2005-03-08

An Analysis of SeaWinds Simultaneous Wind/Rain Retrieval in Severe Weather Events

Jeffrey R. Allen
Brigham Young University - Provo

AN ANALYSIS OF SEAWINDS SIMULTANEOUS WIND/RAIN

RETRIEVAL IN SEVERE WEATHER EVENTS

by

Jeffrey R. Allen

A thesis submitted to the faculty of

Brigham Young University

in partial fulfillment of the requirements for the degree of

Master of Science

Department of Electrical and Computer Engineering

Brigham Young University

August 2005

BRIGHAM YOUNG UNIVERSITY

GRADUATE COMMITTEE APPROVAL

of a thesis submitted by

Jeffrey R. Allen

This thesis has been read by each member of the following graduate committee and by majority vote has been found to be satisfactory.

_____   _____
Date   David G. Long, Chair

_____   _____
Date   Karl F. Warnick

_____   _____
Date   Richard H. Selfridge

BRIGHAM YOUNG UNIVERSITY

As chair of the candidate's graduate committee, I have read the thesis of Jeffrey R. Allen in its final form and have found that (1) its format, citations, and bibliographical style are consistent and acceptable and fulfill university and department style requirements; (2) its illustrative materials including figures, tables, and charts are in place; and (3) the final manuscript is satisfactory to the graduate committee and is ready for submission to the university library.

_____   _____
Date   David G. Long
                                          Chair, Graduate Committee

Accepted for the Department

                                          _____
                                          Michael A. Jensen
                                          Graduate Coordinator

Accepted for the College

                                          _____
                                          Douglas M. Chabries
                                          Dean, Ira A. Fulton College of
                                          Engineering and Technology

ABSTRACT

AN ANALYSIS OF SEAWINDS SIMULTANEOUS WIND/RAIN RETRIEVAL IN

SEVERE WEATHER EVENTS

Jeffrey R. Allen

Department of Electrical and Computer Engineering

Master of Science

Scatterometers, such as SeaWinds, can provide wide coverage of ocean surface winds. They estimate near-surface wind vectors by relating measured radar backscatter to a geophysical model function. However, SeaWinds measurements are also sensitive to rain, and conventional wind retrieval degrades in rainy conditions.

An algorithm that exploits SeaWinds' sensitivity to both wind and rain has be developed. This algorithm, termed simultaneous wind/rain retrieval, retrieves both wind vectors and rain rates for a given ocean area.

Instantaneous results of simultaneous wind/rain retrieval in Hurricane events is analyzed through comparison with the NEXRAD ground-based radar system. This comparison allows validation of retrieved rains. Additionally, conditions that affect the accuracy of SeaWinds wind/rain observations are evaluated. It is shown that, when thresholded, the rains retrieved by SeaWinds give an adequate rain flag.

The comparisons of SeaWinds and NEXRAD rain estimates facilitate construction of a model to simulate variability in the SeaWinds rain estimates. The model is used to show that rain estimates are unbiased, though with significant variability. The variability is likely to be primarily driven by the noise inherent to the SeaWinds system.

ACKNOWLEDGMENTS

I would like to thank my graduate advisor, Dr. David Long for his patience, help, and dedication in the creation of this thesis. I appreciate that he was willing to spend many hours teaching and advising me from early in my studies. His example has helped me become a better student and person.

I would also like to thank my wife Emily, for her support throughout my studies. I appreciate the time that she spent working and caring for our son Paul, to allow me to study and write this thesis. I would also like to thank Paul for not crying very much.

Contents

List of Tables

List of Figures

Chapter 1

Introduction

1.1 Overview

Oceans play an important role in the Earth's heat transfer and global climate. Knowledge of oceanic conditions is important to a variety of disciplines. Before the introduction of remote sensing satellites, observation of the ocean was limited to coastal and ship based observations. These observations are restricted in range and coverage area. Satellite remote sensors allow periodic oceanic observation over wide areas. We focus our attention on the type of space-borne remote sensor called a scatterometer.

Scatterometry is the science of measuring radar scattering from a distributed target such as the Earth. Scatterometry primarily contributes to oceanic information by facilitating estimation of near-surface wind speeds and directions. Scatterometers can cover a large percentage of the Earth's surface daily in all weather conditions as well as at night. Near-surface winds gathered by scatterometers may improve knowledge of the Earth's present and future weather conditions.

The SeaWinds scatterometers aboard QuikSCAT and the Advanced Earth Observing Satellite 2 (ADEOS II), were launched in 1999 and 2003, respectively. Their primary mission is to provide wide coverage of near ocean surface winds. Knowledge of these winds facilitates weather prediction and observation on a global scale. The winds retrieved by the scatterometers have been shown to be highly accurate in areas with moderate wind speeds and no rain [1, 2]. However, the wind estimates have been shown to degrade in rainy conditions [3, 4, 5].

1.2 Rain Observation

Both SeaWinds instruments are Ku-band (14 GHz) radar scatterometers that utilize polarized radar to measure surface backscatter. Near-surface wind vectors are estimated by measuring radar backscatter. Radar reflections off ocean waves are influenced by the height and orientation of the waves. Specifically, in the Ku band, one of the principle components of the backscatter is a function of scattering from surface capillary waves. Near surface wind speed and direction may be determined by relating the backscatter to an empirically derived geophysical model function (GMF).

However, rain changes the wave structure and backscatter signature. This is because rain drops change the received backscatter by attenuating the radar signal through the air and inducing additional waves on impact. The conventional GMF does not account for rain effects and wind vector estimation accuracy is degraded.

To improve rain contaminated wind estimates Draper and Long synergistically combined colocated Tropical Rain Measurement Mission (TRMM) and SeaWinds measurements to develop a new GMF that explicitly accounts for rain [6]. Relation of the new GMF to backscatter allows simultaneous estimation of corrected wind vectors and vertically integrated rain rate [7].

Validation of SeaWinds rain retrieval has been performed through monthly averaging [6], Cramer-Rao bound analysis, and Monte Carlo Simulation [8]. However, instantaneous rain rate estimation of real data has not been throughly studied.

Ground based weather radars are able to accurately detect rain at relatively high resolutions. SeaWinds instantaneous rain estimates may be studied by comparing colocated ground and SeaWinds rain observations. However, ground radar is limited in range and the radar platform must be on land. To perform a valid rain estimation study, SeaWinds rain data may be compared with rain detected by coastal ground weather radar in several rainy events.

In this thesis we explore simultaneous wind/rain retrieval in North Atlantic storm events. This study is performed to estimate the accuracy of the SeaWinds rain retrieval and determine conditions that affect that accuracy. Analysis is performed through comparison of instantaneous colocated SeaWinds and ground based next

generation weather radar (NEXRAD) measured rain rates. Additionally, a simple noise model for the retrieval algorithm is developed and algorithmic trade-offs are discussed.

1.3 Results Summary

In this thesis we verify that simultaneous wind/rain retrieval finds comparable rain fields to those determined by NEXRAD. The algorithm yields an effective rain flag for rain affected areas. Additionally we show that the mean retrieved rain is correct, but the variability of the rain estimates is large. The high variability is also exhibited by rain estimates from other sensors. We then show that the variability of the rain estimates is driven by the communications noise of the SeaWinds sensor.

1.4 Contributions

This thesis makes three contributions to the field of wind based scatterometry. These contributions are discussed the following paragraphs.

First, colocated rain and wind fields are created and compared for several events and sensors. These events are comprised of a large variety of wind vector and rain conditions. In most cases, hurricane events are used. This is because hurricanes exhibit a diverse range of wind speeds, wind directions and rain rates. This diversity allows for investigation of simultaneous wind/rain retrieval over this range. The correlation of NEXRAD and SeaWinds-based rain rates for each event is analyzed. Linear correlation of both rain rates is explored, and the correlation coefficient of both data sets for the events is determined.

The second contribution of this thesis is analysis of conditions that improve or degrade simultaneous wind/rain retrieval. Correlation of rain rates and wind vectors are determined for several such conditions. Relative wind direction and swath location effects on data correlation are also explored. Rain effects on wind vector estimation are demonstrated. A rain-only algorithm is developed. The algorithm's effect on rain detection in rain dominated areas is demonstrated.

The final contribution of this thesis is the development of a simple Sea-Winds/NEXRAD noise model. Rain estimates from both sensors are noisy. A noise model that incorporates combined rain estimation error is examined through Monte Carlo simulation. The combined standard deviation of the real data rain rate standard deviation is estimated and an accuracy bound on SeaWinds rain estimated is determined. Additional simulation employs the accuracy bound and rain-only retrieval to compare the variability in the rain estimates to the variability in the SeaWinds measurements. We demonstrate that the variability is primarily caused by the measurement variability.

Additionally, the appendix contains three reports that contribute to the field of scatterometer-based ice detection.

First the Appendix contains a report on the expected daily dilation and contraction of Antarctic sea-ice. Sea-ice data provided by the passive Special Sensor Microwave/Imager (SSM/I) and QuikSCAT are used to find the distribution of sea-ice advance along with statistics for several areas of Antarctica. This data may be used in future ice detection algorithms to limit detection errors by limiting allowed ice change.

Also included is a study of SeaWinds-on-QuikSCAT and tandem mission (Combined SeaWinds-on-QuikSCAT and SeaWinds-on-ADEOS II) polar ice detection. Areal ice extent and case studies are used to determine detection improvements yielded by the fusion of data from two observers.

Finally, a study comparing sea-ice detection methods developed by Remund and Long is included [9, 10]. Advantages and improvements of each method are noted along with recommendations for algorithm improvement.

1.5   Outline

This thesis is organized into six chapters and three appendices. Each chapter's topic is noted below.

- Chapter 2 gives background into SeaWinds measurements, simultaneous/wind rain retrieval, NEXRAD measurements, and sources of measurement error for all sensors.

- Chapter 3 delves into SeaWinds based rain retrieval accuracy by comparing instantaneous rain rates from SeaWinds and NEXRAD for several events.

- Chapter 4 compares rain correlation and wind retrieval in several measurement and meteorologic conditions. Also, an algorithm for rain-only retrieval is proposed and tested.

- Chapter 5 approximates SeaWinds/NEXRAD rain measurement error by developing, modeling, and simulating a rain noise model. The noise model is then used in conjunction with rain-only retrieval to estimate the rain estimation variability due to SeaWinds' measurement uncertainty.

- Chapter 6 concludes by summarizing results and discussing future research.

- Appendix 1 contains a study on daily Antarctic sea-ice advance and retreat.

- Appendix 2 examines the advantages of the tandem mission and QuikSCAT only sea-ice detection.

- Appendix 3 studies and compares two scatterometer-based sea-ice detection algorithms.

Chapter 2

Background

2.1 Introduction

Ku-band scatterometers such as SeaWinds, estimate near-surface wind speed and direction through relating measured radar backscatter to a model of the ocean surface [11]. Rain changes the ocean scatterers by inducing additional waves and signal attenuation. The presence of rain degrades conventional wind estimates [3, 4, 5]. Rain affects 4-10% of SeaWinds measurements [6].

SeaWinds wind estimation [8] is performed by measuring the normalized radar cross section (σ°) of an ocean target and relating the measurement to near-surface wind speed and direction. The relationship between σ° and surface wind vectors is termed the geophysical model function (GMF) [12, 13, 14]. Wind vector estimates are produced by inverting the GMF using several σ° measurements for a given point [15].

In order to ameliorate wind estimate errors in rain contaminated σ° measurements Draper and Long developed a simultaneous wind/rain retrieval method for SeaWinds [8] that, in this thesis, is termed the Draper method. This method allows Seawinds to simultaneously measure wind and integrated columnar rain rate. The Draper method was developed and validated through simulation and comparison with measurements from the Tropical Rain Measurement Mission (TRMM) [6, 7, 8].

To analyze simultaneous wind/rain retrieval colocated rain information from NEXRAD and QuikSCAT are compared. Sections 2.2 and 2.3 describe SeaWinds and NEXRAD based rain rate detection. Section 2.3.1 discusses the possible causes of detection error.

2.2 SeaWinds Simultaneous Wind/Rain Estimates

SeaWinds backscatter measurements are provided by two identical instruments, QuikSCAT-on-SeaWinds and SeaWinds-on-ADEOS-II. To measure $\sigma°$, the instruments employ a rotating pencil beam antenna. The antenna is fed by two offset feeds, the first is a H-polarized beam with a surface incidence angle of approximately $46°$, and the other is a V-polarized beam with a $54°$ incidence angle. The beams are rotated to trace two helical surface patterns. The inner beam extends approximately 700 km from nadir while the outer beam extends 900 km from nadir. For points inside the inner beam region this arrangement allows the instrument to retrieve four $\sigma°$ measurements from four distinct azimuth angles [16].

SeaWinds $\sigma°$ measurements are spatially gridded into 25 km $\times$ 25 km wind vector cells (WVCs). The outer 9 WVCs on each side of the swath are in the outer-beam-only region and the center 18 WVCs are in the nadir region. In these WVCs wind estimation skill is low due to the lack of measurement azimuth diversity. The remaining cells in the off-nadir inner-beam regions are in the region known as the "sweet spot". Measurements made in the sweet spot have greater azimuth diversity and corresponding high estimation skill [16, 17].

Near-surface wind vectors of each WVC are determined by inverting the GMF given co-located $\sigma°$ measurements in each WVC through maximum likelihood estimation. By assuming Guassian white noise and independent samples, the probability of the $\sigma°$ measurements given near-surface wind velocity and direction $\vec{u}$ is

$$p(\vec{z}|\vec{u}) = \prod_k \frac{1}{\sqrt{2\pi}\zeta} \exp\left(-\frac{1}{2}\frac{(z_k - M(\vec{u}, \phi_k, ...))^2}{\zeta^2}\right), \tag{2.1}$$

where $\vec{z}$ is a vector of $\sigma°$ measurements, M is the GMF, and ζ^2 is the measurement variance [8]. The GMF is a function of wind vector $\vec{u}$, the instrument azimuth angle

8

ϕ_k, and other parameters such as rain rate. However, standard processing algorithms ignore rain in wind retrieval. SeaWinds estimates the wind by taking the negative logarithm of Eq. (2.1), dropping constant terms and applying an iterative search routine to find a minima [18]. In the case of ambiguities, ambiguity selection is performed using thresholded nudging [19] and an iterative median filter [20].

The conventional model function, QMOD3, does not explicitly account for rain effects. Rain effects change the backscatter characteristic and can be large or even dominating [8, 21]. Such rain effects may be especially prevalent in a hurricane environment. Figure 2.1 displays conventional winds retrieved during Hurricane Frances' landfall (9/5/2004 10:30 UTC). Rain effects are seen in the area between Florida and the Bahama islands. Along one line it may be seen that winds in adjacent WVCs are perpendicular to each-other. Such winds are physically unrealistic and are at least partly due to rain contamination.
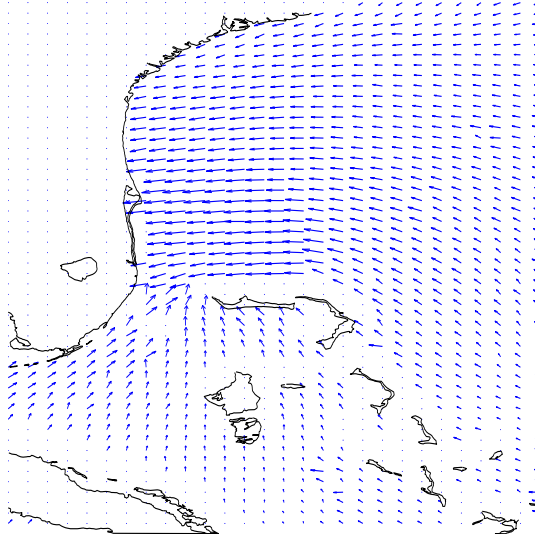
Figure 2.1: Conventional SeaWinds observed winds during Hurricane Frances' landfall (9/5/2004). Many WVCs between the Florida coast and the Bahama islands are rain contaminated and have perpendicular wind vectors.

To account for rain effects Draper and Long developed a new GMF that explicitly accounts for rain effects [8]. The new GMF models rain effects on σ° as

$$\sigma_m = \sigma_w \alpha_r + \sigma_e, \tag{2.2}$$

where σ_m is the received backscatter, σ_w is the backscatter due to the near-surface wind stress, α_r is the two way signal attenuation due to the attenuation due to hydrometeors, and σ_e is the backscatter due to rain surface impact [8, 21, 22]. The new GMF (M_r) is expressed in [7] as

$$M_r(\vec{u}, \phi_k, R, ...) = M(\vec{u}, \phi_k, ...)\alpha_r(R) + \sigma_e(R). \tag{2.3}$$

In [6], colocated rain measurements from the TRMM, wind vector estimates from the National Centers for Environmental Prediction (NCEP), and σ° SeaWinds measurements are combined to estimate the parameters $\alpha(R)$ and $\sigma_e(R)$ as quadratic functions of R.

Inversion of the new GMF allows simultaneous wind vector and vertically integrated rain rate retrieval. Simultaneous wind/rain retrieval reports rain in units of km mm/hr, which may be interpreted as the rain rate at each infinitesimal altitude integrated from the ground to the maximum height of the storm. In order to limit errors, the maximum rain rate retrieved by simultaneous wind/rain retrieval is limited to 100 km mm/hr.

Simultaneous wind/rain retrieval requires multiple measurements and high instrument skill and may only be performed in inner-beam region of the swath. This limits the simultaneous wind/rain retrieval swath width to 1400 km and allows daily rain observations of at least 80% of the Earth's ocean surface.

The Draper method divides SeaWinds observed wind/rain data into three regimes [23]. In regime 1, σ° is dominated by rain. In regime 2, wind and rain contributions to σ° are on the same order. Regime 3 contains areas where σ° is wind-dominated. The regions are defined through thresholding the estimated rain induced backscatter (σ_e°) and the measured backscatter (σ_m°). Regime 1 contains areas in which $\sigma_e^\circ/\sigma_m^\circ \geq 0.75$ and regime 3 contains areas in which $\sigma_e^\circ/\sigma_m^\circ \leq 0.25$ [23]. The

regimes help in understanding the conditions in which wind or rain information can be extracted. Wind data from regime 1 and rain data in regime 3 may be unobtainable. Simultaneous wind and rain estimates can be obtained for data in regime 2.

2.3 NEXRAD Rain Estimation

NEXRAD measures reflectivity and Doppler shift by employing a rotating 8.5 m paraboloid antenna [24]. The 750 kW radar operates in the S band (2.7 - 3.0 GHz) and successively scans 360° in 1° increments in the azimuth angle and from 0.5° to 16.5° in 1° increments in elevation angle. The radar also performs an additional circular scan at 19.5°. NEXRAD generally rotates at 3.4 rpm and completes a volume scan approximately every 5 minutes.

Given reflected power measurements, P_r, NEXRAD estimates reflectivity, Z, using

$$Z = \frac{2^{10}(\ln 2)}{\pi^3 c} \frac{\lambda^2}{P_t \tau G^2 \theta_{3dB}^2} \frac{r^2 P_r}{|K|^2},\tag{2.4}$$

where Z is the reflectivity, c is the speed of light in a vacuum, λ is the transmitted wavelength, P_t is the transmitted power, τ is the pulse duration in seconds, G is the antenna gain, θ is the 3dB antenna beam-width, r is the range to target, and K is the complex index of refraction for water [24]. Z is estimated at 1 km over the range of 1 to 460 km from the radar.

In general, the reflectivity to rain rate (Z-R) relationship is modeled as

$$Z = aR^b,\tag{2.5}$$

where R is the rain rate in mm/hr and a and b are constants [25]. Through numerous aircraft observations Jorgensen and Willis determined the Z-R relationship of mature hurricanes to be $Z = 300R^{1.35}$ [26]. The rain rate for a given volume scan can be determined by inverting the Z-R relationship using Z data in NEXRAD Level II data provided by the NOAA Radar Operations Center (ROC).

2.3.1 Error Discussion

NEXRAD and SeaWinds measurements differ in sensitivity to near-surface rain. NEXRAD's volume scan does not measure near-surface scatterers while such scatterers are principle contributors to SeaWinds measurements. Large near-surface precipitation may result in significant rain estimation discrepancies.

This study compares NEXRAD and SeaWinds observations that are colocated by the spatial extent of the SeaWinds WVC at the surface. Due to their observation geometries, the observations are not necessarily colocated at higher altitudes (see the discussion in [6]). This vertical misregistration also increases the variability in the rain rate comparisons.

Scattering due to hydrometeors is dependent on operating frequency [27]. SeaWinds is a Ku-band instrument while NEXRAD is a S-band instrument. Both sensors have distinct sensitivities to hydrometeor size distributions and differences in rain rate estimation may result.

High rain events attenuate NEXRAD's signal through scattering from near range hydrometeors and attenuation from liquid water on the radome [24]. This causes P_r attenuation and rain rate underestimation. The attenuation increases with distance to target. Fading limits the maximum useful range of the radar and adds error to the rain rate estimate. In this study, NEXRAD's maximum range extends to the maximum range in which fading does not dominate rain rate estimates. Fading effects are determined subjectively through human analysis and comparison with QuikSCAT rain estimates. For each event NEXRAD's maximum useful range varies between 200 and 350 km.

Each rain cell in each storm has a unknown precipitation profile and Z-R relationship. This Z-R relationship may differ from that determined by [26]. For example, [28] determined the Z-R relationship for drizzle and thunderstorms to be

$$Z = 140R^{1.5} \tag{2.6}$$

and

$$Z = 500R^{1.5}, \tag{2.7}$$

respectively [28]. Additionally, if non-liquid water precipitation such as wet hail is present, Douglas [29] found the Z-R relationship to be

$$Z = 84000R^{1.29}. \tag{2.8}$$

Figure 2.3.1 displays rain rate as a function of Z (dB) for the above relationships. Precipitation variability due to Z-R relationship error increases with rain rate. If hail is present, bright banding occurs and the variability can become large relative to the rain estimate. Nevertheless, in this report we use $Z = 300R^{1.35}$ for our Z-R relationship.
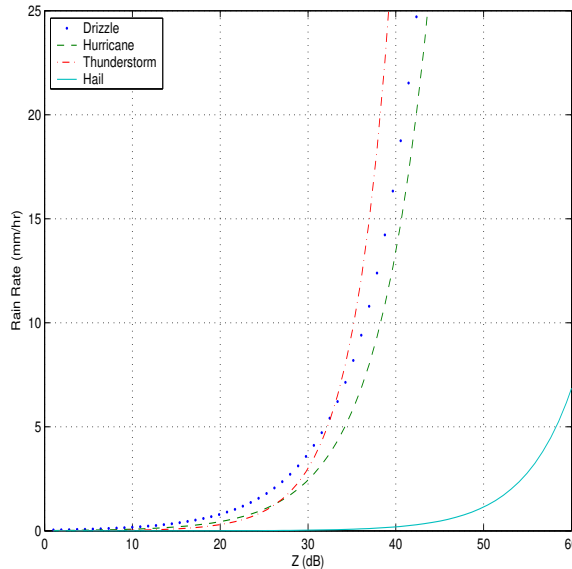
Figure 2.2: Rain rate vs. reflectivity plot for various Z-RR relationships. Liquid rain rate variability due to Z-R relationship changes is generally less than 2 mm/hr. If hail is present, "bright banding" of the rain rate occurs, resulting in overestimation of the rain rate.

SeaWinds does not uniformly sample each WVC. The beam has a non-uniform antenna beam pattern that integrates backscatter over its footprint. Rain has high

spatial variability and is rarely uniform over a given WVC, which results in non-uniform samples of a non-uniform rain event. It is possible that one SeaWinds measurement within a WVC may detect no rain while another may detect high rain rates. This is known as the beamfilling effect [8] and contributes to estimation errors.

Chapter 3

Results

In this chapter we develop and test a rain estimate comparison approach for SeaWinds and NEXRAD rain data. The goal of the comparison is to determine how well rain information from each sensor correlates. We expect colocated rain rates from each sensor to be linearly correlated. For this reason the primary metric used in evaluating the similarities of the rain estimates is the correlation coefficient. Additional comparison is made by evaluating various rain and wind maps from both sensors and external sources.

3.1 Approach

To validate SeaWinds rain estimates, we compare the SeaWinds and NEXRAD rain observations. The comparison is made by evaluating virtually instantaneous co-located rain intensity data from each sensor. In order to create comparable data, the NEXRAD rain rate is estimated and averaged over each SeaWinds WVC. To ensure temporal rain cell co-location, only NEXRAD data observed within 5 min. of the SeaWinds observation is considered.

3.1.1 Resolution Adjustments

In order to compare SeaWinds and NEXRAD rains we need to account for the scales on which the sensors report rain. Simultaneous wind/rain retrieval reports the columnar vertically integrated rain rate for each 25×25 km WVC. NEXRAD rain is reported in 1 km range bins along each incidence and azimuth angle in the volume scan. Thus, in order to create comparable resolution data, the NEXRAD rain rate is

spatially and vertically averaged over each SeaWinds WVC. To determine the average NEXRAD rain rate for a given WVC, we average all the NEXRAD measurements that are located vertically above the WVC, subject to a maximum observation height of 10 km. We found that using the 10 km ceiling eliminates scattering from non-rain sources in the upper atmosphere, while preserving rain information and correlation with SeaWinds-based rains. Averaging in this manner provides a measurement of the vertically integrated rain on the same scale reported by SeaWinds.

To convert the SeaWinds rains from km mm/hr to mm/hr for comparison to NEXRAD observations, we must estimate the storm height. Hurricanes have a storm height that can vary between 6 and 12 km [24]. This height varies for each area of each storm. However, in this study, storm height information is unavailable. Hence, for simplicity, we desire to estimate a fixed storm height for all events. We consider two storm height estimation approaches: least squares approximation and cumulative distribution function (CDF) fitting.

In least squares approximation, the Draper rain rate is scaled such that the slope of the least squares fit of the two rain rates has a slope of one. This approach ensures that, on the average, the Draper to NEXRAD rain rate has a 1 to 1 relationship. Using least squares approximation, we estimate a fixed storm height of about 6 km. However, the least squares approach assumes that our observations are collected from one noisy and one noiseless sensor. In our study, both observers are influenced by noise. Additionally, we note that when the 6 km height is employed, the CDFs of the rain rates from each sensor exhibit large differences.

Thus, in this study, we adopt an approach that fits the CDFs of the two rain rates. We assume the storm height for all events to be the constant that, subjectively, best matches the CDFs of the Draper and NEXRAD rain rates. This approach allows us to ensure that the probability that both sensors detect a given rain rate is approximately equal. Through experimentation with the cases described below, we observe that an assumed storm height of approximately 8 km best matches the CDFs of each sensor's rain rate. Hence, to facilitate our comparison with NEXRAD, we

16

scale all simultaneous wind/rain observations by 1/8. We note that the correlation coefficient metric is independent of scale factor.

To illustrate our approach, Fig. 3.1 displays the NEXRAD rain that has been averaged into 1 km × 1 km vertical bins and the SeaWinds WVCs for Hurricane Isabel's landfall (9/18/2003). An image of the vertically, temporally, and spatially integrated NEXRAD rain rate for Hurricane Isabel's landfall is displayed in Fig. 3.2.

3.2 Case Study Results

In this section SeaWinds and NEXRAD rain estimates from several storm events during 2003 and 2004 are evaluated. SeaWinds-on-QuikSCAT observed all events except Hurricane Isabel, which was observed by SeaWinds-on-ADEOS-II. For validation purposes a low wind/rain event and several hurricane events are examined. Spatial and numerical analysis is performed and correlation is determined for all WVCs whose centers lie within NEXRAD's estimated maximum useful range.

3.2.1 Low Wind/Rain Observation

For validation purposes, NEXRAD and SeaWinds rain information from an arbitrary low wind/rain event are compared. NEXRAD radar data from Jacksonville, FL on August 27, 2004 at 10:55 UTC is compared with co-located SeaWinds rain estimates. The NEXRAD rain rate is projected onto the SeaWinds WVC grid and compared to the rain map generated by the Draper method from SeaWinds data. The corresponding rain maps are displayed in Fig. 3.3. NEXRAD's approximate maximum useful range (300 km) is delineated by the circular line while the vertical line delineates the approximate boundary between SeaWinds' nadir region and sweet spot.

Figure 3.3 shows that SeaWinds and NEXRAD estimated rain rates have high spatial correlation within the useful range. Both sensors detect the storm extending east from central Florida with similar rain rates. A scatter-plot of the rain observed by both sensors is shown in Fig. 3.4. While the number of comparison points is small, in general, the rain rates from both sensors agree within 4 km mm/hr. The
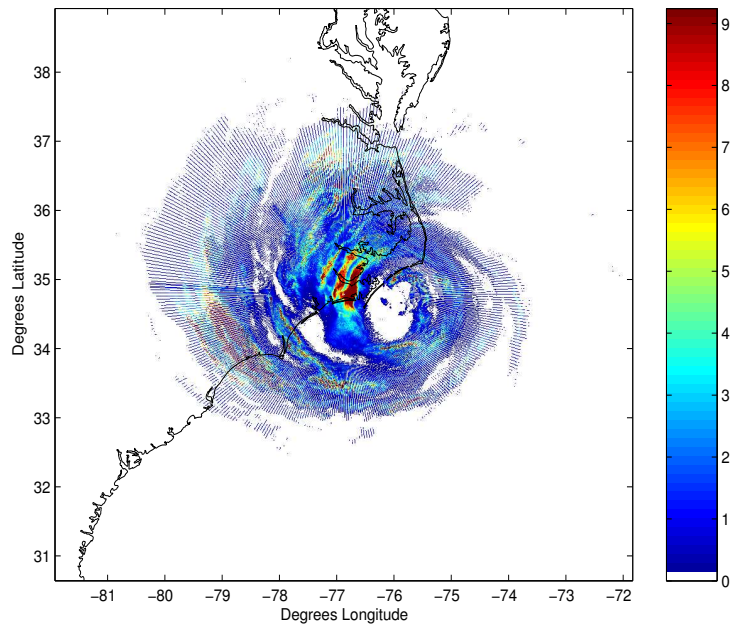
Figure 3.1: NEXRAD measured vertically integrated rain rate of Hurricane Isabel's landfall from Morehead City, NC (9/18/2003, 16:00 UTC). The artifacts on the outer edges of the swath are due to a decrease in azimuth resolution as ranges to target increases.
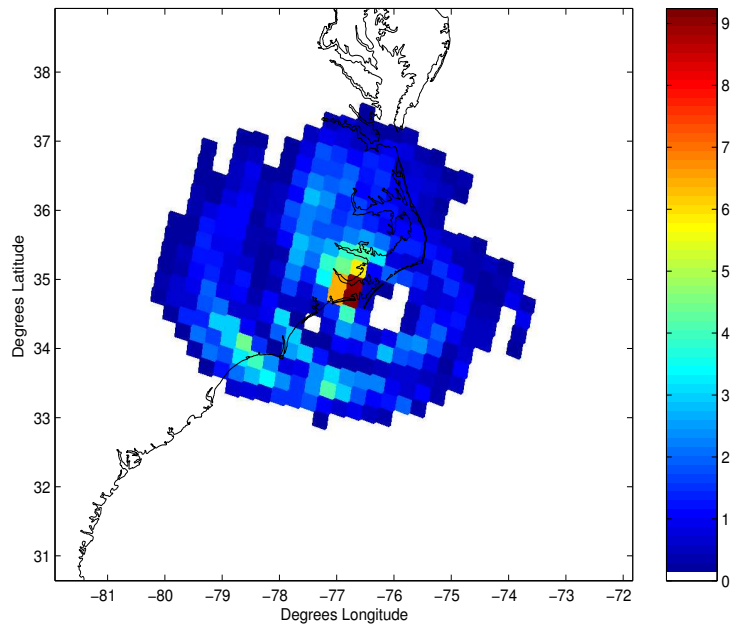
Figure 3.2: NEXRAD rain rate (mm/hr) averaged into SeaWinds WVCs during Hurricane Isabel's landfall (9/18/2003, 16:00 UTC).

correlation coefficient of the rain rates is 0.9241, which demonstrates the high linear dependence of the rain rates. In this case, both sensors' rain estimates are similar, validating the comparison approach.
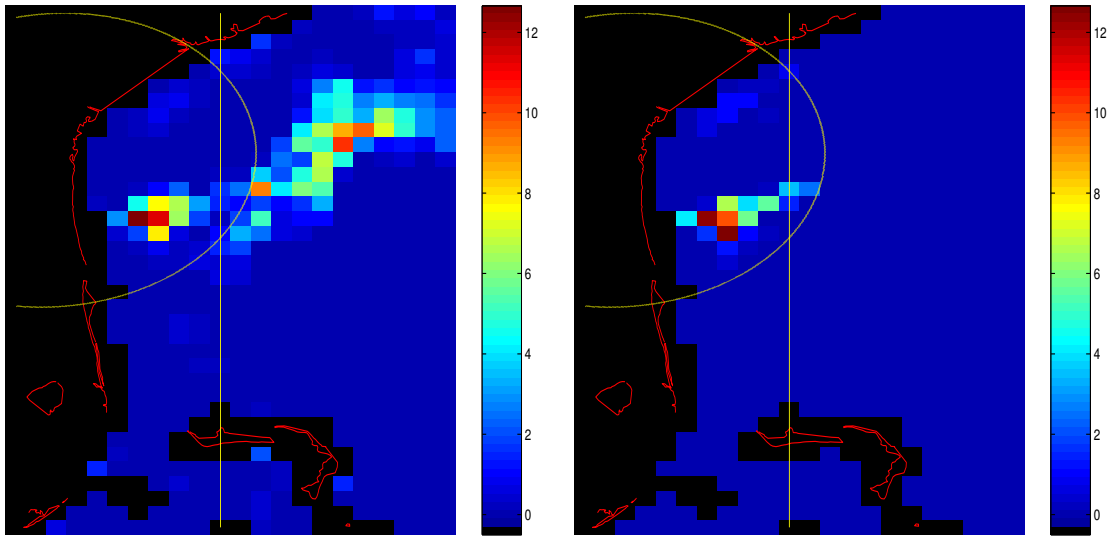
(a) SeaWinds estimated rain rate (mm/hr).   (b) NEXRAD estimated rain rate (mm/hr).

Figure 3.3: SeaWinds and NEXRAD rain rates for the low wind/rain observation (8/27/2004) projected onto a 25×25 km WVC grid aligned with the along/cross track of SeaWinds' swath. All data to the left of the vertical line are in the nadir region of Seawinds' swath while data to the right of the line are in the sweet spot. The circular line delineates NEXRAD's maximum useful range

3.2.2 Hurricane Isabel

On September 18, 2003 Hurricane Isabel made landfall on the North Carolina coast. SeaWinds on ADEOS II observed the landfall at approximately 16:00 UTC while NEXRAD continuously observed the event from Morehead City, NC. In this case NEXRAD's estimated maximum useful range is 250 km.
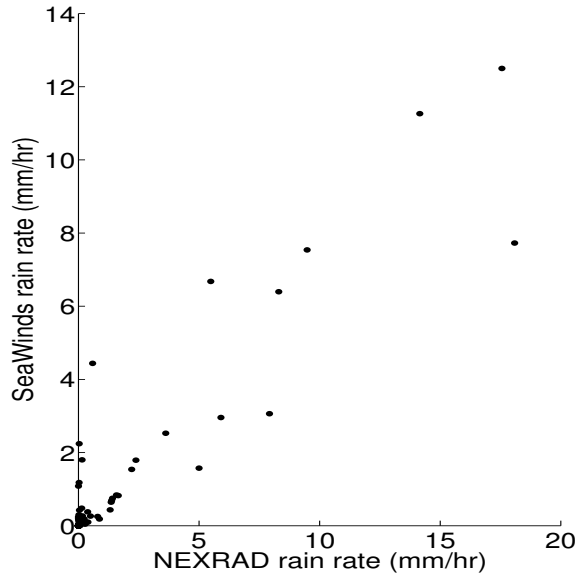
Figure 3.4: Scatter-plot of SeaWinds and NEXRAD integrated rain rates corresponding to Fig. 3.3. The data has a correlation coefficient of 0.9241 and includes all 85 ocean points that fall within the circle in Fig. 3.3.

To facilitate a comparison of various rain estimate and flagging algorithms Fig. 3.5 displays the NEXRAD rain rate, the multidimensional histogram (MUDH) rain flag [30], normalized objective function (NOF) rain flag [31], and the Draper rain rate. The vertical line in the figures delineates the approximate boundary between the nadir region and sweet spot of the SeaWinds swath. The majority of the co-located information is in the nadir region of the SeaWinds swath.

To illustrate the wind vectors of the event, Fig. 3.6 displays wind vector maps of the event. The winds are provided by the National Centers for Environmental Prediction (NCEP), the SeaWinds conventional wind retrieval, SeaWinds conventional wind retrieval with directional interval retrieval and threshold nudging (DIRTH) smoothing [32], and Draper wind/rain retrieval.

Figure 3.5 shows that the estimated rain rates have some spatial correlation. The eye, eye-wall, and some rain bands are in co-located, although the eye is larger in the NEXRAD map. In order to verify vertically integrated rain rates, a scatter-plot
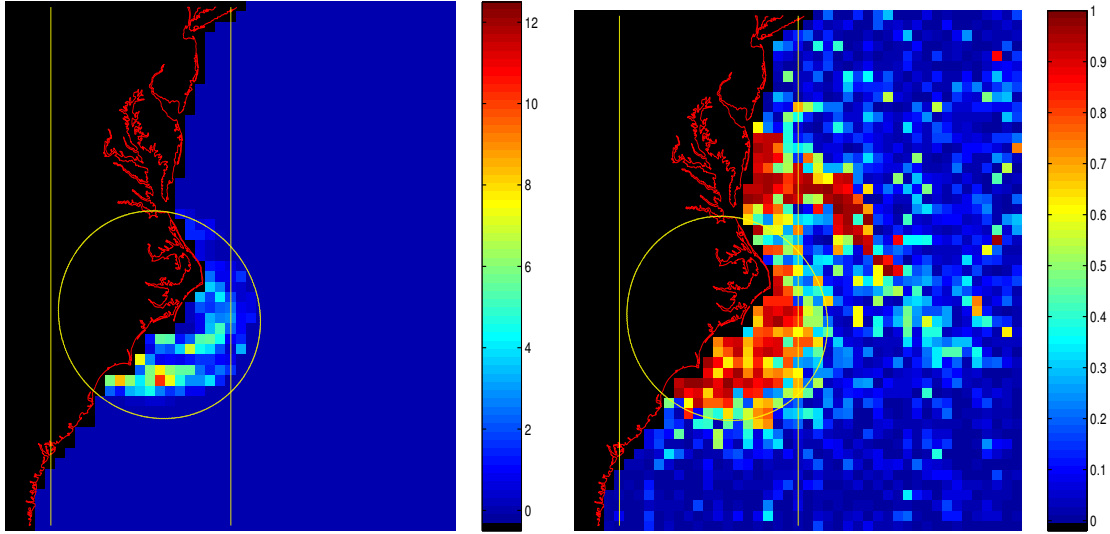
(a) NEXRAD rain rate.

(b) MUDH rain probability
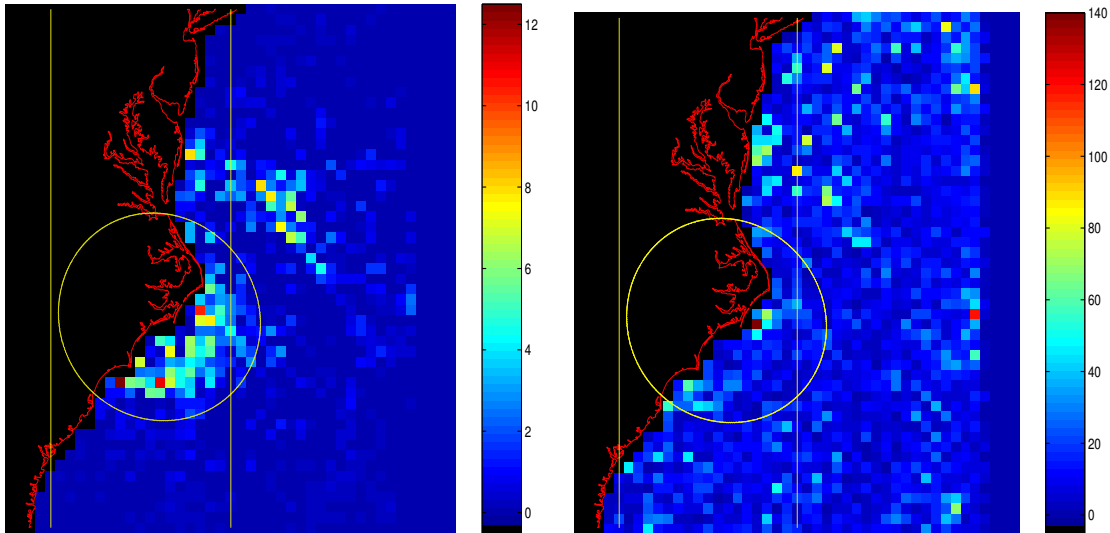
(c) Draper rain rate.

(d) NOF rain flag.

Figure 3.5: Rain rates and flags from SeaWinds observation of Hurricane Isabel (9/18/2003 16:00 UTC). Circles represent NEXRAD's estimated maximum useful range, and vertical lines delineate SeaWinds swath's nadir region, see Fig. 3.8.
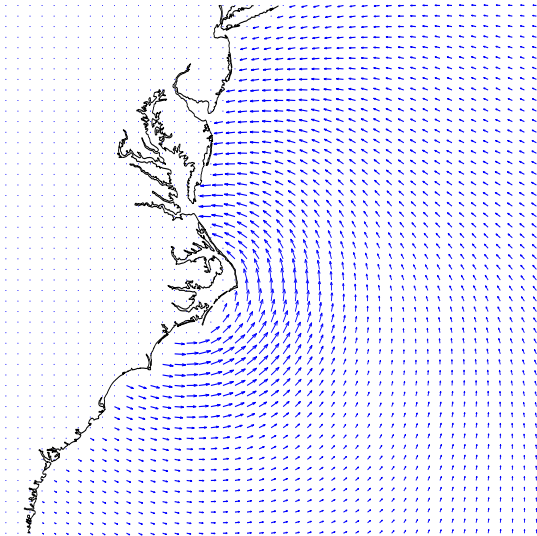
(a) NCEP wind vectors.
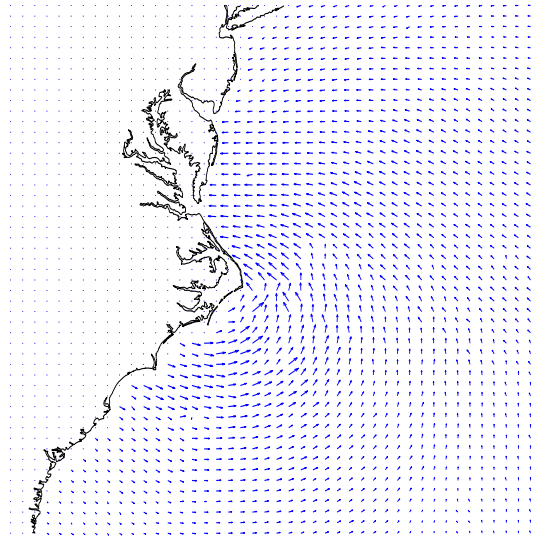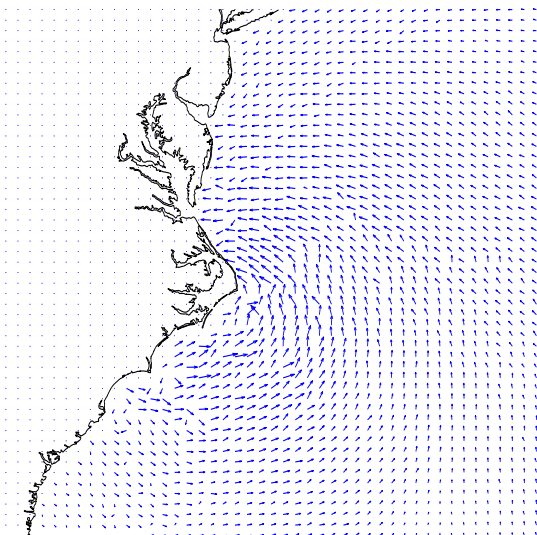
(b) L2B wind vectors.

(c) Draper wind vectors.

(d) L2B wind vectors with DIRTH smoothing.

Figure 3.6: Wind vectors from SeaWinds' observation of Hurricane Isabel (9/18/2003 16:00 UTC).

of both rain rates is displayed in Fig. 3.7. The correlation coefficient of the data is 0.6759, which is lower than the low wind/rain case.
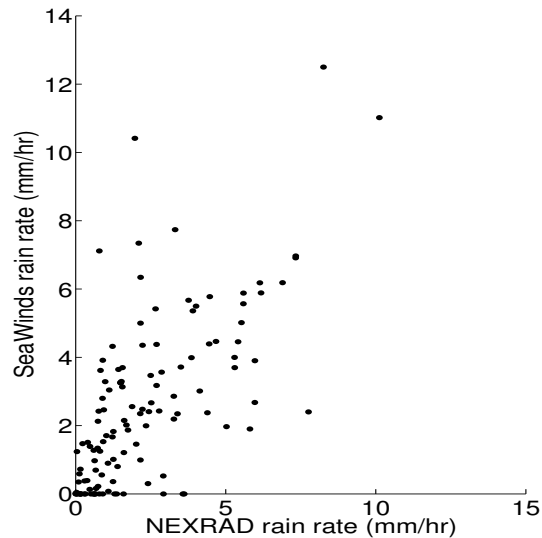
Figure 3.7: Scatter-plot of SeaWinds and NEXRAD integrated rain rates from Hurricane Isabel's landfall (9/28/2003 16:00 UTC). The correlation coefficient of the data is 0.6759. The data consists of 124 points.

The ADEOS-II platform also carries the advanced microwave scanning radiometer (AMSR) which also provides rain rate estimates. Co-location of AMSR and SeaWinds-on-ADEOS-II is nearly instantaneous. For comparison purposes, Figs. 3.8(a), 3.8(b), and 3.8(c) show QuikSCAT's, NEXRAD's, and AMSR's rain observations of Isabel's landfall. All three rain fields have general similarities. They show the hurricane eye and outer rain bands in the same locations with similar intensities.

Figure 3.9 displays scatter-plots comparing AMSR's rain field to those obtained through NEXRAD and SeaWinds. The correlation coefficient of the comparison are 0.7172 and 0.7283, respectively. These coefficients are is similar each sensor's separate correlation with NEXRAD data, although AMSR appears to overestimate the rain rate.
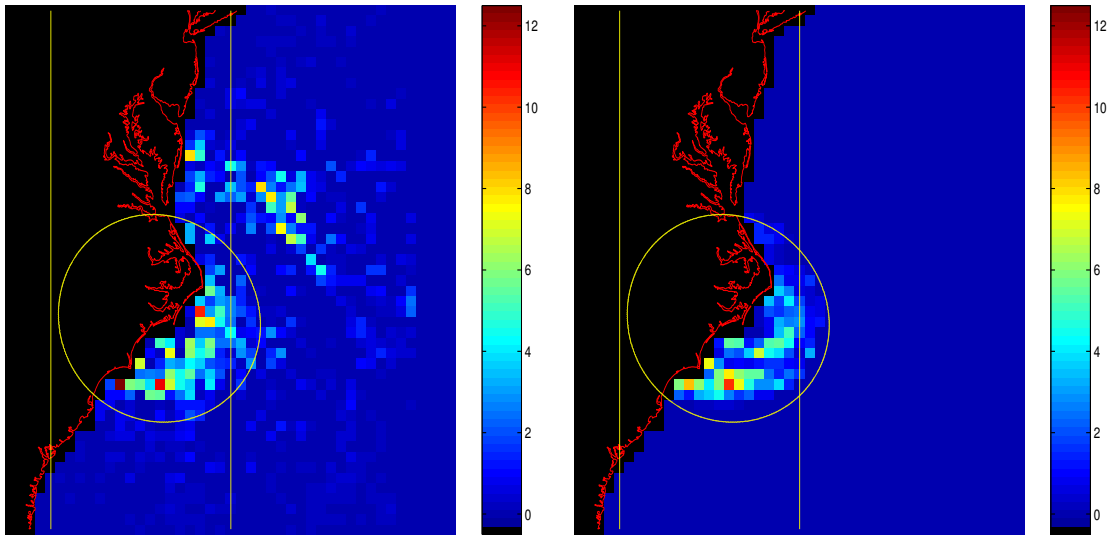
(a) SeaWinds estimated rain rate of Hurricane Isabel landfall (mm/hr).

(b) NEXRAD estimated rain rate of Hurricane Isabel landfall (mm/hr).
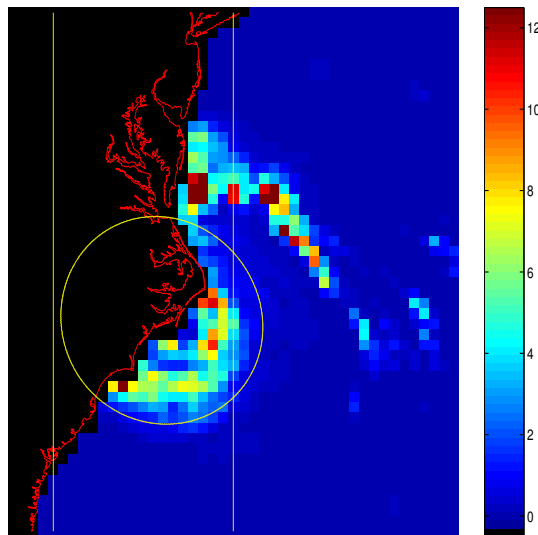
(c) AMSR estimated rain rate of Hurricane Isabel landfall (mm/hr).

Figure 3.8: SeaWinds and NEXRAD rain rates for Hurricane Isabel's landfall (9/18/2003, 16:00 UTC). The circular line delineates NEXRAD's maximum useful range. All data to the left of the vertical line are in the nadir region of Seawinds' swath while data to the right of the line are in the sweet spot. The majority of measurements are located in the nadir region of the swath.
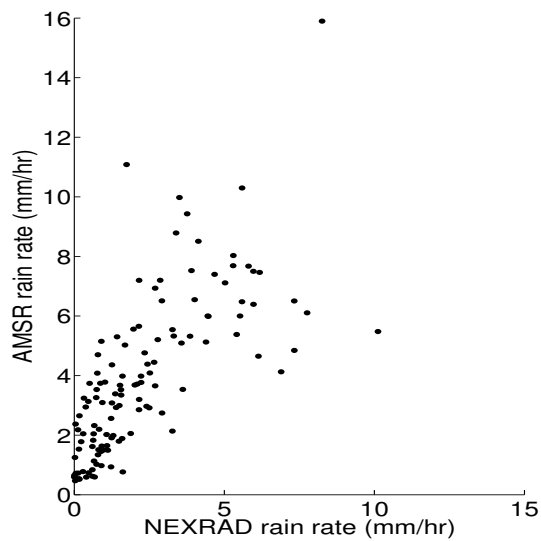
(a) Scatter-plot of AMSR vs. NEXRAD estimated rain rate (mm/hr). The correlation coefficient of the data is 0.7172 and consists of 124 points.
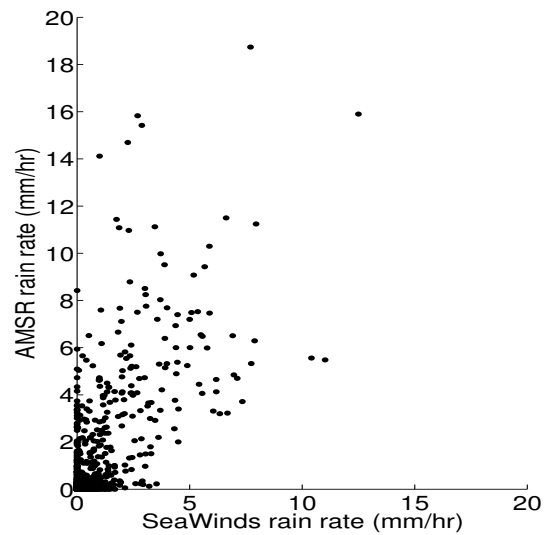
(b) Scatter-plot of SeaWinds and AMSR integrated rain rates in Hurricane Isabel's landfall on 9/28/2003 16:00 UTC. The correlation coefficient of the data sets is 0.7283 and consists of 1542 points.

Figure 3.9: AMSR, SeaWinds, and NEXRAD rain rate scatter-plots.

In summary, cross comparison of NEXRAD, SeaWinds, AMSR rain rates yield similar results. Rain rate differences due to noise, calibration error, and other error sources cause wide rain rate discrepancies. However, correlation coefficients from each comparison are similar. It is reasonable to conclude that the error sources for each instrument are independent, but on the same order of magnitude.

3.2.3 Hurricane Alex

On August 1, 2004 at 10:30 UTC, Hurricane Alex was observed by SeaWinds and NEXRAD radar in Jacksonville, FL. During observation Alex was still maturing and had not developed the high winds exhibited by more mature hurricanes. Each sensor's rain and wind estimate from the storm observation are is displayed in Figs. 3.10 and 3.11. All data to the left of the vertical line is in the sweet spot while data to the right of the line is in the nadir region. NEXRAD's maximum useful range is estimated to be 350 km.

A scatter-plot of both sensor's rain rate estimates is displayed in Fig. 3.12. NEXRAD estimates that the pixel at the center of the storm has a rain rate of nearly 30 mm/hr which may be due to hail induced bright banding. The correlation coefficient of the two plots is 0.8244, significantly larger than that of Isabel. This may be due to several factors. Seawinds' observation of Isabel was primarily from the nadir region of its swath, while Alex was observed in the sweet spot. Also, Alex exhibits smaller winds and higher rains than Isabel. Low winds and high rains increase the rain/wind $\sigma°$ ratio and may improve rain rate retrieval [8].

As in the case with previous comparisons, both sensors detect the storm in the same location. Also, neither rain plot exhibits a well defined hurricane eye or rain bands. This is consistent with Alex's stage of development.
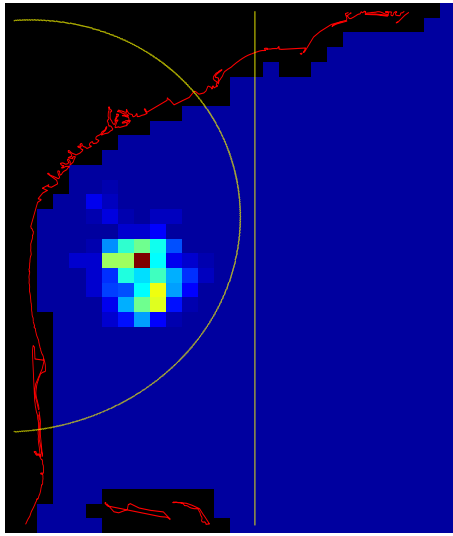
(a) NEXRAD rain rate.
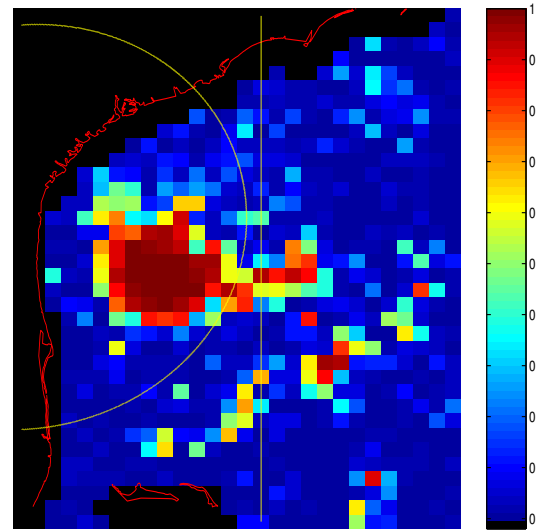
(b) MUDH rain probability
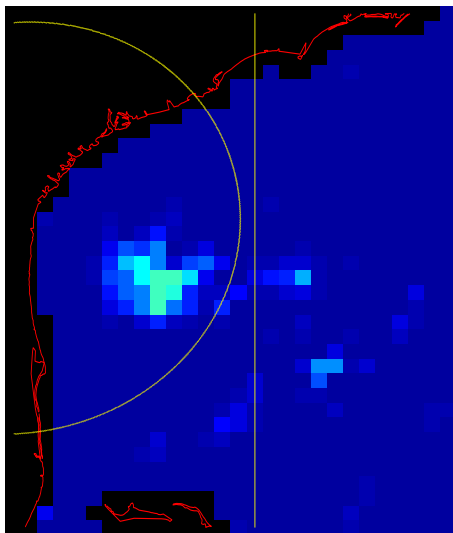
(c) Draper rain rate.

(d) NOF rain flag.

Figure 3.10: Rain rates and flags from SeaWinds observation of Hurricane Alex (8/1/2004 10:30 UTC). Circles represent NEXRAD's estimated maximum useful range. Data left of the vertical line is in the sweet spot of SeaWinds' swath.
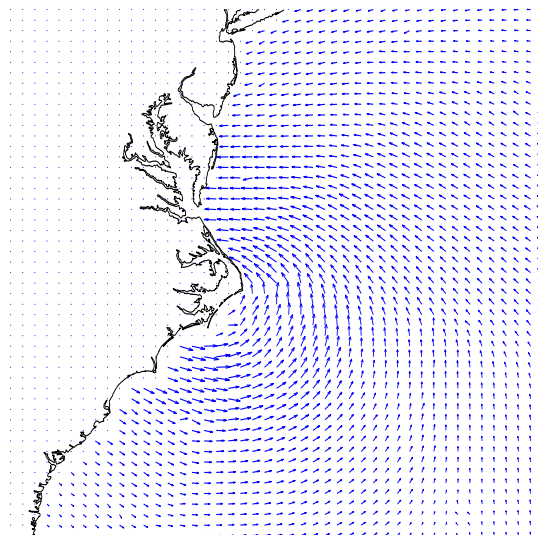
(a) NCEP wind vectors.
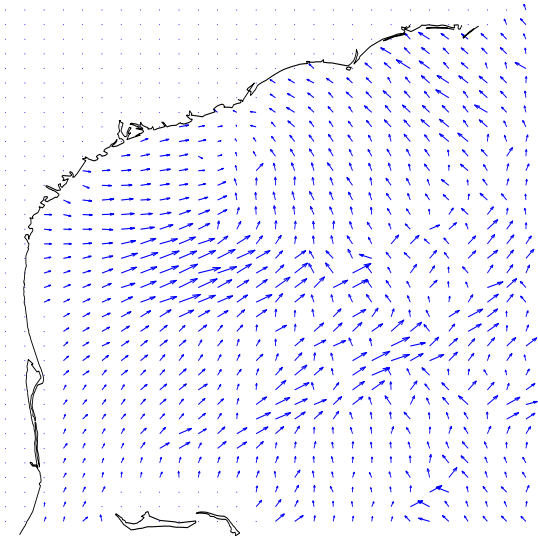
(b) L2B wind vectors.

(c) Draper wind vectors.
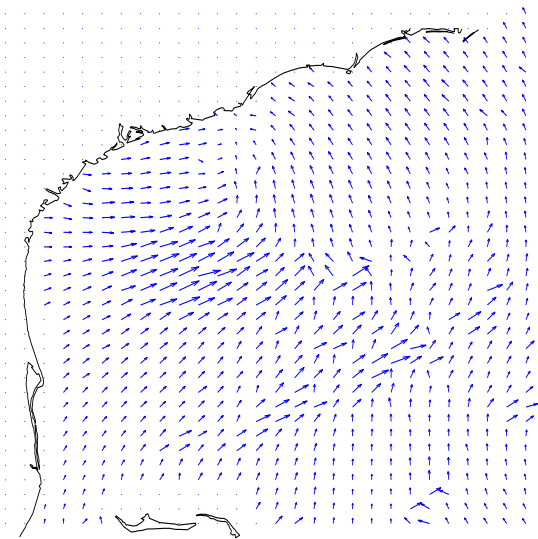
(d) L2B wind vectors with DIRTH smoothing.

Figure 3.11: Wind vectors from SeaWinds' observation of Hurricane Alex 8/1/2004 10:30 UTC).
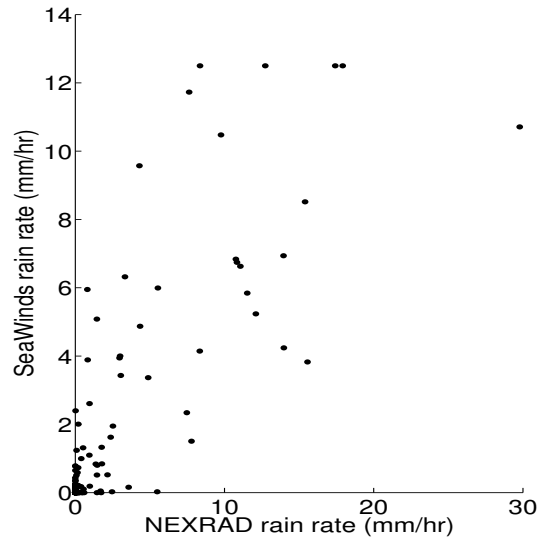
Figure 3.12: Scatter-plot of SeaWinds and NEXRAD rain rates for Hurricane Alex. With a coefficient of 0.8244 correlation of the this observation is higher than that of Isabel, but lower than the low wind/rain case. The data consists of 178 points.

3.2.4 Hurricane Frances

Hurricane Frances made landfall in central Florida on September 4-5, 2004. Frances was a very large, slow moving, storm. Its slow movement allowed SeaWinds make three observations of the landfall event at 10-12 hour intervals. To illustrate the hurricane location of each observation, corresponding NEXRAD rain rate observations from Melbourne, FL are shown in Fig 3.13.

The first observation of Frances (Fig. 3.13(a)) occurred while the hurricane eye was over the Bahama Islands, and outer rain bands reached central Florida. Rain rate estimates from SeaWinds and NEXRAD are displayed in Fig. 3.14. NEXRAD's estimated maximum useful range is 300 km. The two vertical lines in the figures display SeaWinds' nadir region boundaries. In this case all usable co-located data is within the nadir region of the swath.

Wind fields from the event are shown in Fig. 3.15. L2B and DIRTH wind vectors around the eye tend to point in either the along or cross track directions of the swath, and in some areas (such as east of the Bahama islands), the adjacent WVCs
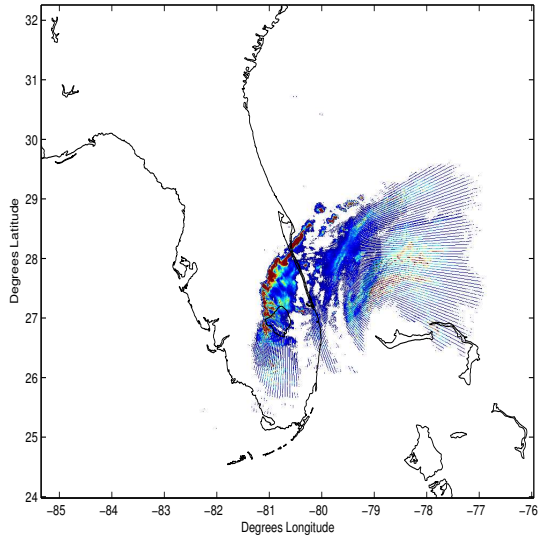
(a) 9/4/2004, 10:55 UTC
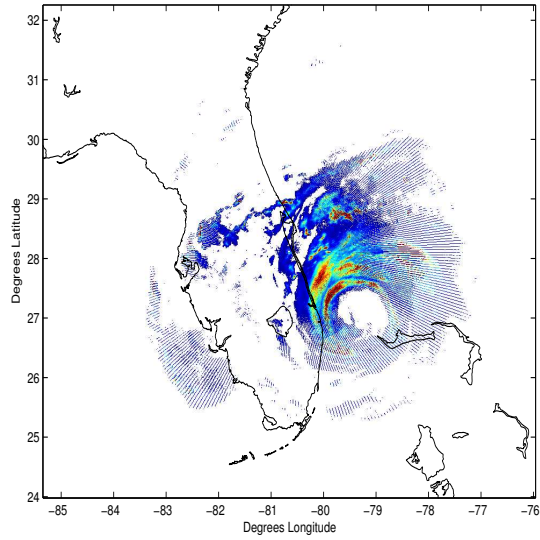
(b) 9/4/2004, 23:15 UTC
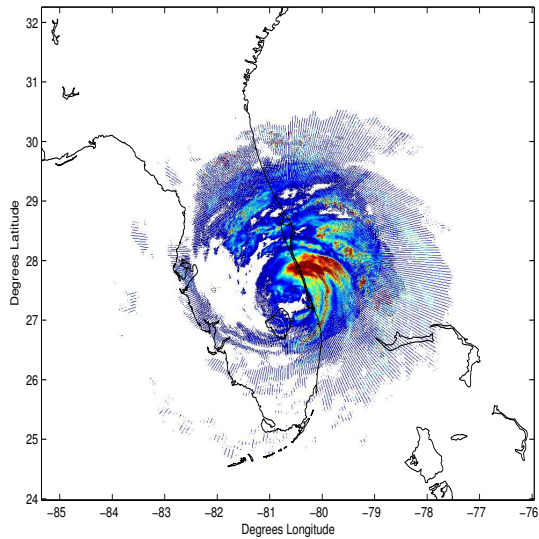
(c) 9/5/2004, 10:30 UTC

Figure 3.13: NEXRAD estimated rain rates corresponding to SeaWinds' observation of Hurricane Frances' landfall.

show nearly perpendicular vectors. This effect, termed "squaring off", is caused by rain contaminatation, and is discussed in greater detail in Chapter 4.

Rain rate maps for the observation are shown in Figs. 3.14(a) and 3.14(c). The correlation coefficient of the data sets is 0.7700. Both sensors show no rain in the upper portion of the map. The rain rate scatter-plot of the first Frances observation is shown in Fig. 3.16. SeaWinds detects rates of over 12 mm/hr where the NEXRAD rate detects rates of less than 2 mm/hr but, correlation remains relatively large because the majority of low rain rate cells agree. In this case SeaWinds accurately detects which cells have rain and which do not. However, estimated rain rates differ.
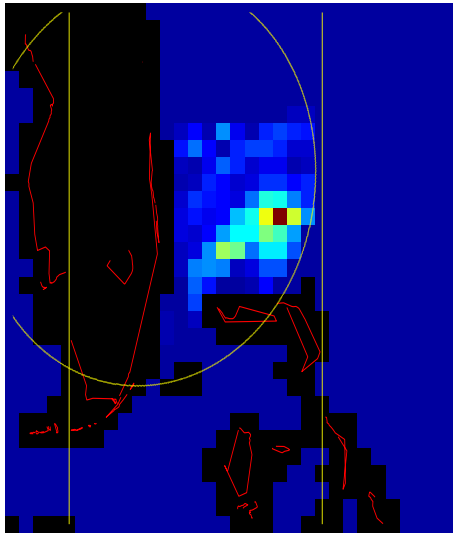
(a) NEXRAD rain rate.
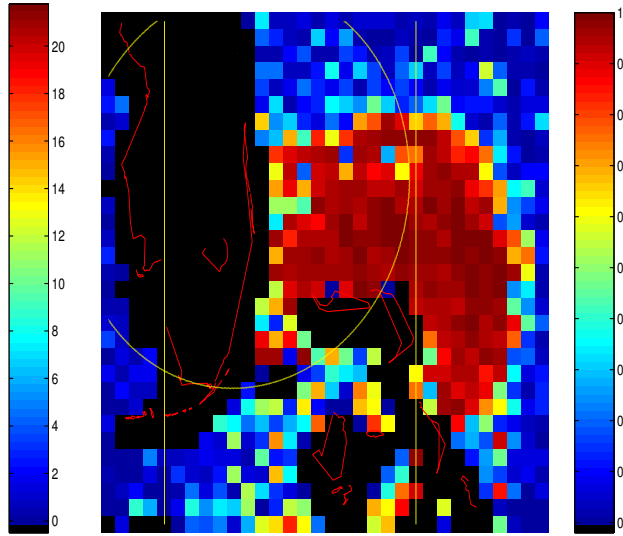
(b) MUDH rain probability
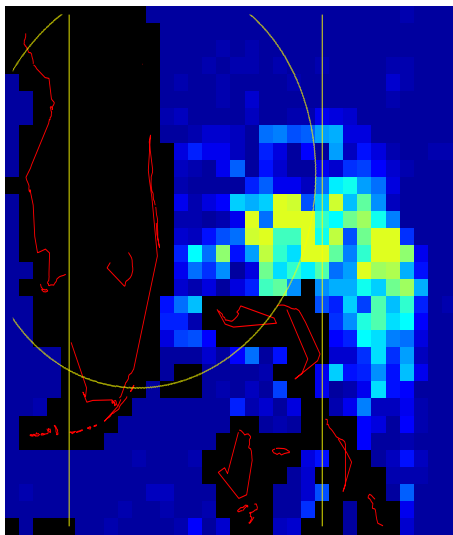
(c) Draper rain rate.
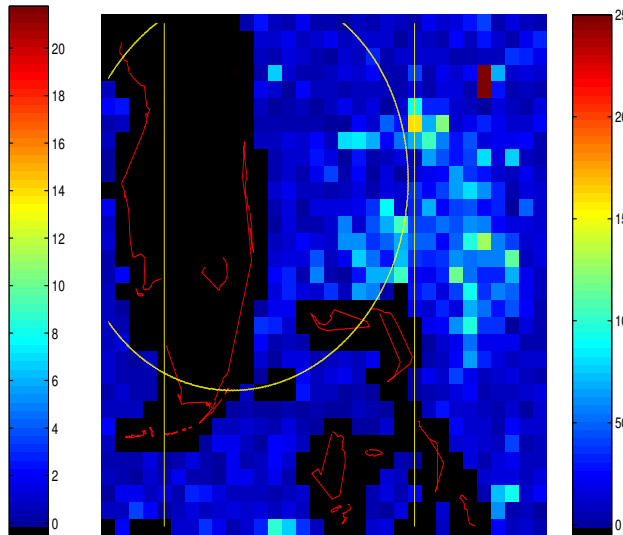
(d) NOF rain flag.

Figure 3.14: Rain rates and flags from SeaWinds first observation of Hurricane Frances (9/4/2004 10:55 UTC). Circles represent NEXRAD's estimated maximum useful range, and vertical lines delineate SeaWinds swath's nadir region.
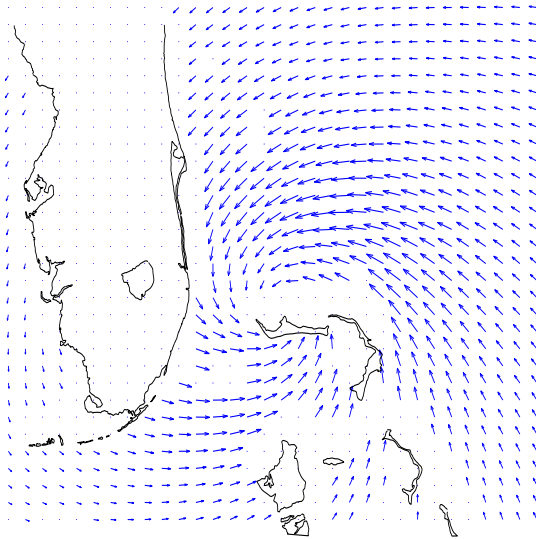
(a) NCEP wind vectors.
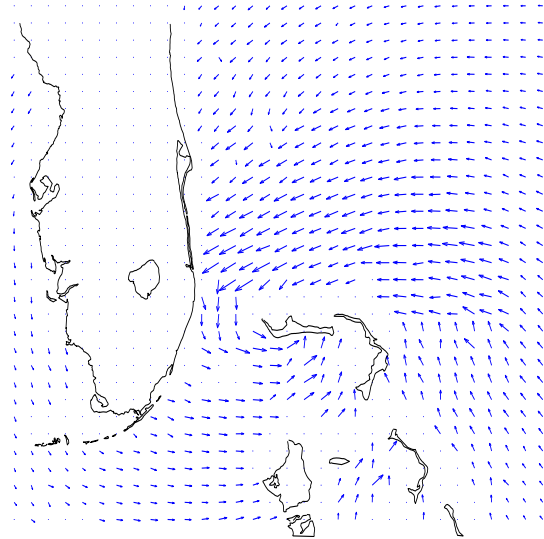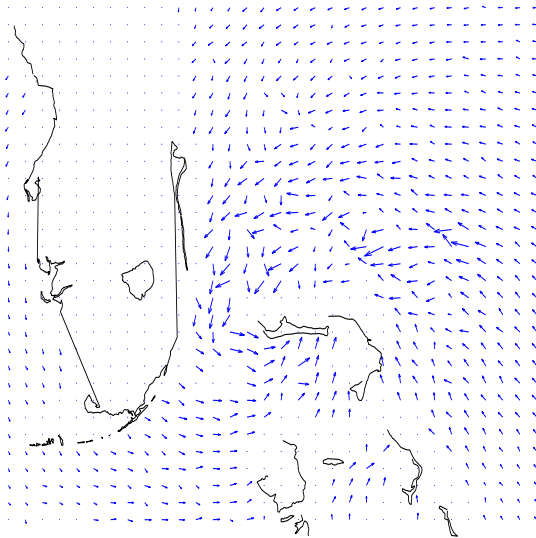
(b) L2B wind vectors.

(c) Draper wind vectors.
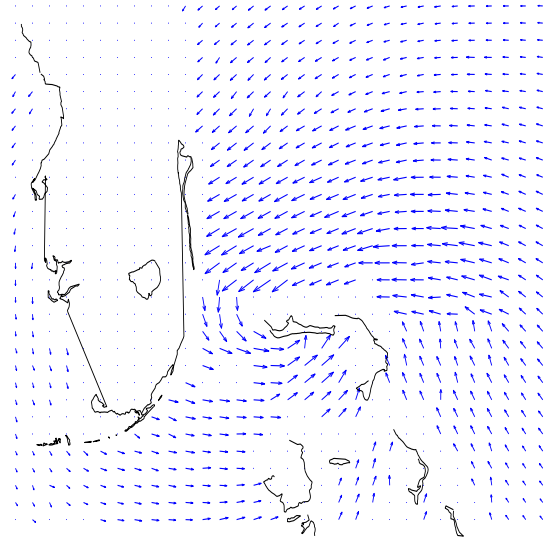
(d) L2B wind vectors with DIRTH smoothing.

Figure 3.15: Wind vectors from SeaWinds' first observation of Hurricane Frances (9/4/2004 10:55 UTC). The L2B and DIRTH wind vectors exhibit squaring off effects.
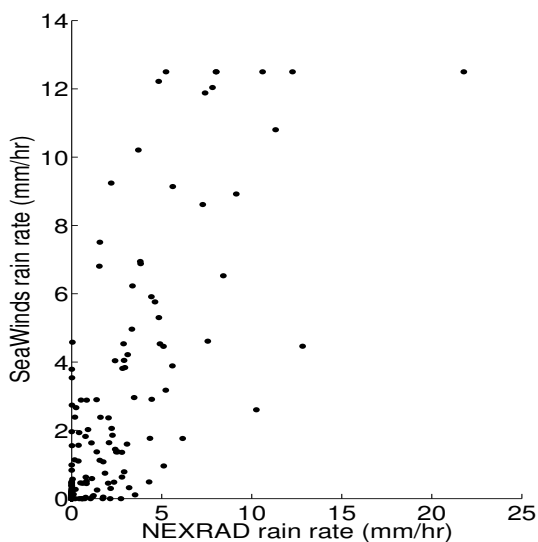
Figure 3.16: Scatter-plot of SeaWinds and NEXRAD rain rates for SeaWinds' first observation of Hurricane Frances. The correlation coefficient is 0.7700. The data consists of 178 points.

The second observation of Hurricane Frances by SeaWinds occurred approximately 12 hours after the first at 23:15 UTC on September 4, 2004. During observation the leading edge of the eye-wall was over the Florida coast (Fig. 3.13(b)). High near field rain rates limit NEXRAD's maximum useful range to approximately 200 km. Rain rates and wind vectors for NEXARAD and several SeaWinds algorithms are displayed in Figs. 3.17 and 3.18. The majority of useful colocated data is in SeaWinds' sweet spot, and the DIRTH and L2B wind fields also exhibit squaring off effects.

Figures 3.17(a) and 3.17(c) display instantaneous rain rate estimates from NEXRAD and SeaWinds. The plots exhibit spatial correlation. Both plots show the storm eye and eye-wall in the same areas. However, outer rain band rain rates are dissimilar.

A scatter-plot of both rain rates is displayed in Fig. 3.19. The correlation of the data has a correlation coefficient of 0.7006, significantly lower than all other hurricane observations.

34
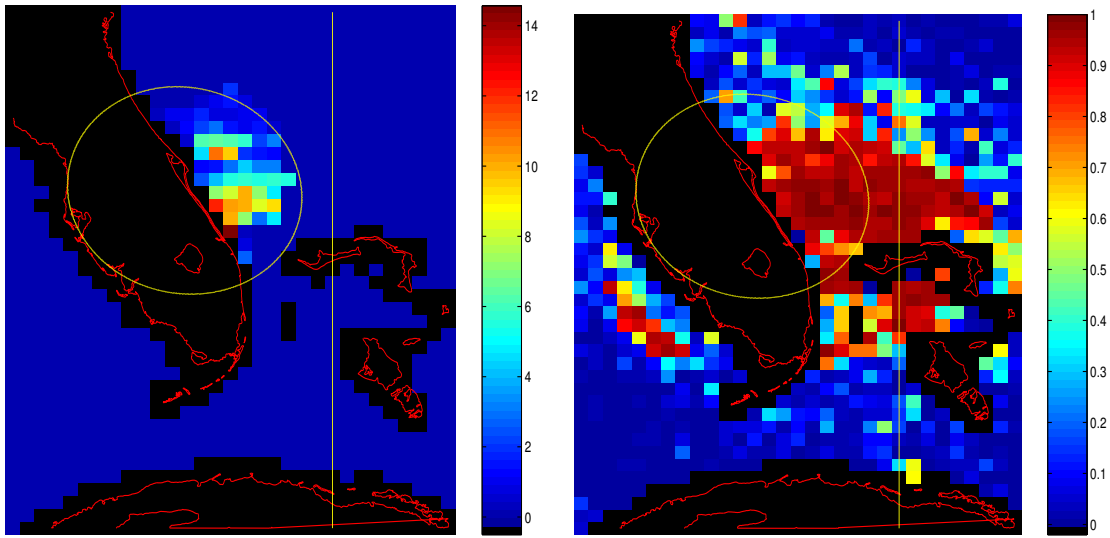
(a) NEXRAD rain rate.

(b) MUDH rain probability
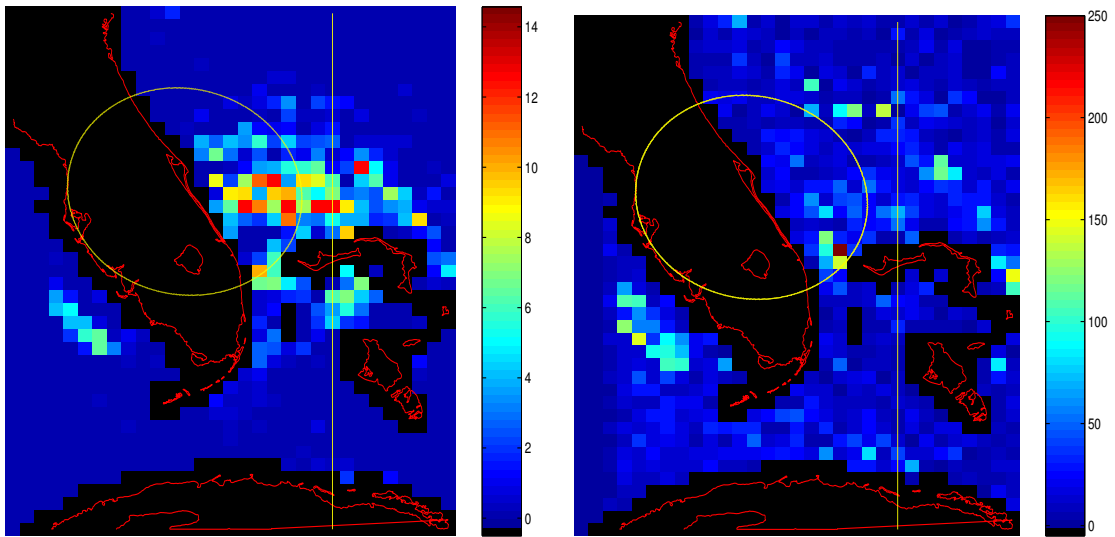
(c) Draper rain rate.

(d) NOF rain flag.

Figure 3.17: Rain rates and flags from SeaWinds second observation of Hurricane Frances (9/4/2004 23:15 UTC). Circles represent NEXRAD's estimated maximum useful range. Data right of the vertical line is in the nadir region of SeaWinds' swath.
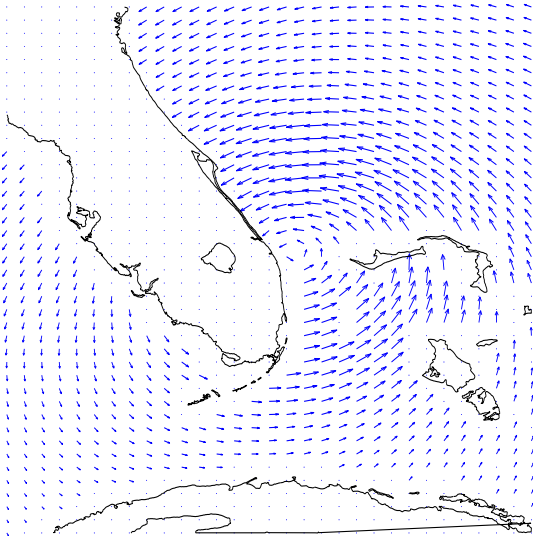
(a) NCEP wind vectors.
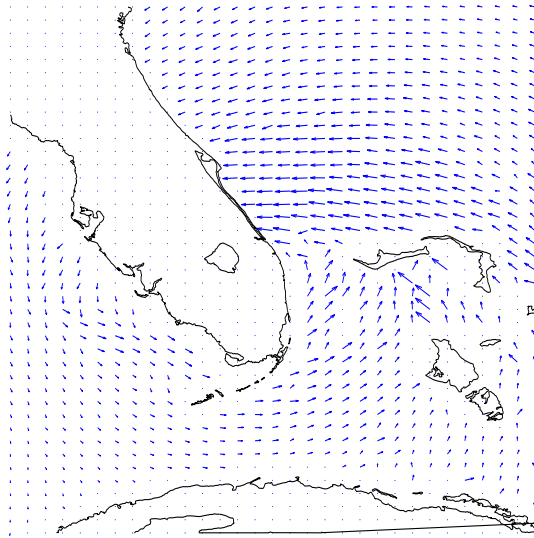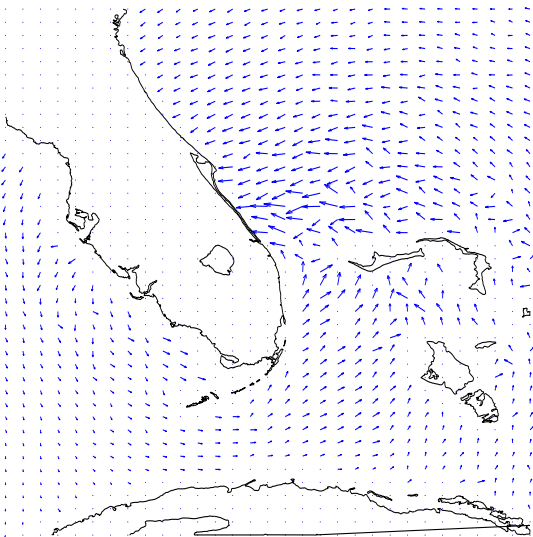
(b) L2B wind vectors.

(c) Draper wind vectors.
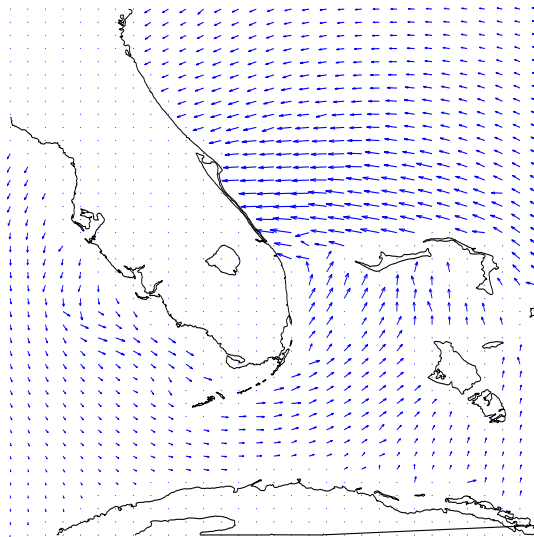
(d) L2B wind vectors with DIRTH smoothing.

Figure 3.18: Wind vectors from SeaWinds' second observation of Frances (9/4/2004 23:15 UTC). The L2B and DIRTH wind vectors exhibit squaring off effects.
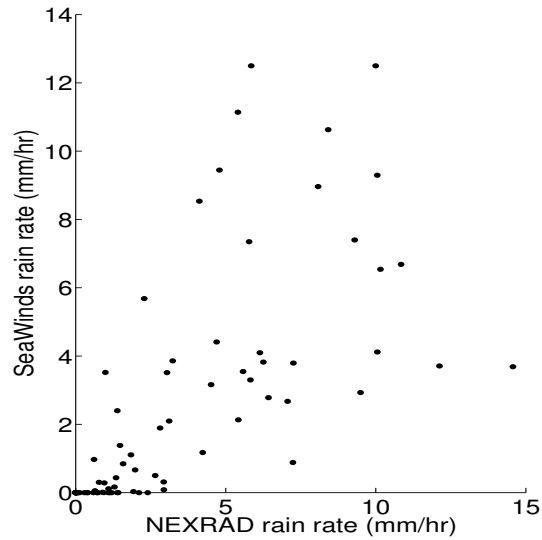
Figure 3.19: Scatter-plot of SeaWinds and NEXRAD rain rates for SeaWinds' second observation of Hurricane Frances. The correlation coefficient is 0.7006. The data consists of 81 points.

Approximately 12 hours after SeaWinds' second observation of Frances' landfall, a final observation was made. In this observation the eye and eye-wall had completed landfall and only outer rain-bands remained over the ocean (Fig 3.13(c)).

Figures 3.20 and 3.21 display the NEXRAD and SeaWinds rain rates and wind vectors for the final observation of Hurricane Frances. All data is in the sweet spot of the SeaWinds swath. NEXRAD's approximate maximum useful range is 275 km. The spatial correlation near the Florida coast is high for both storm location and rain rate.

A scatter-plot of the two rain rates is shown in Fig. 3.22. The correlation coefficient for the data is 0.7413, which is significantly higher than the correlation coefficient of the previous observation. The data converges as the NEXRAD rain rate increases. Figure 3.13(c) shows that, during observation, large near field rains were present. Consequently, Fig. 3.20(a) exhibits fading and all distant WVCs have low rain rates.
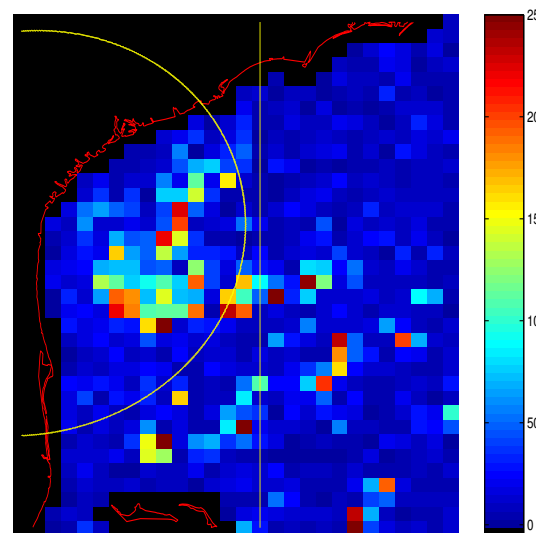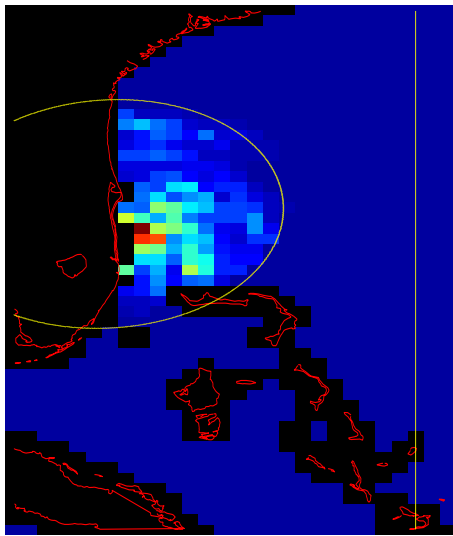
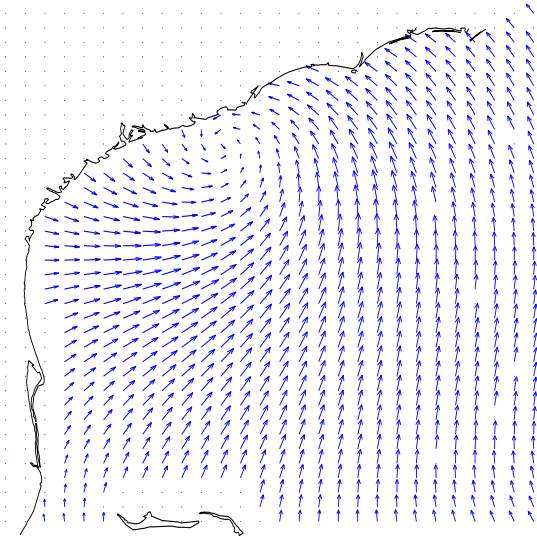(a) NEXRAD rain rate.
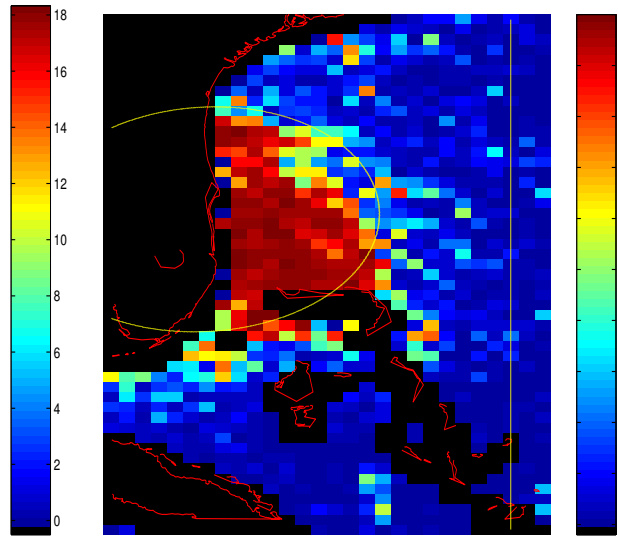
(b) MUDH rain probability
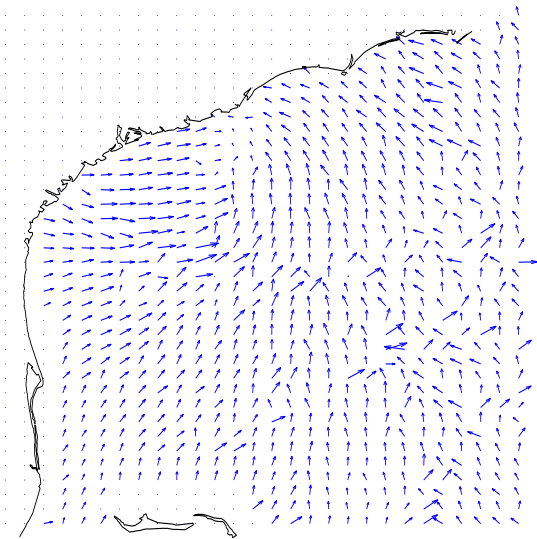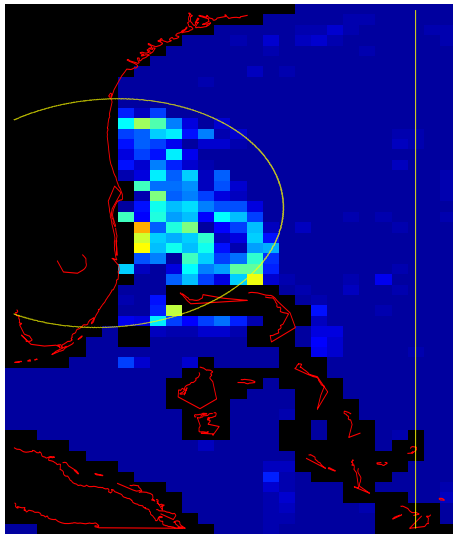
(c) Draper rain rate.
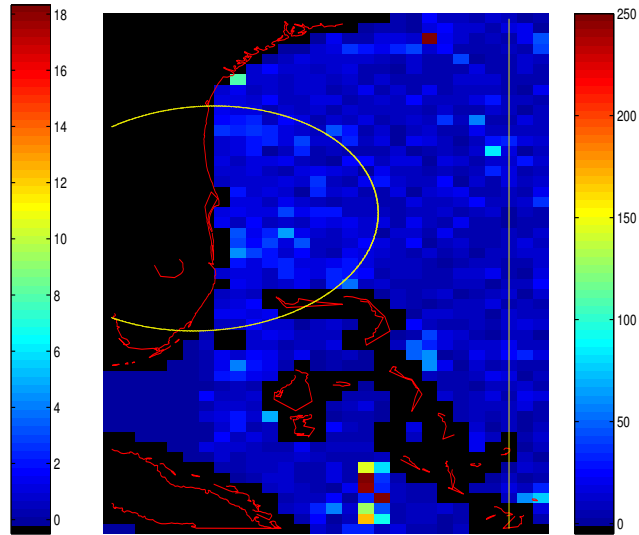
(d) NOF rain flag.

Figure 3.20: Rain rates and flags from SeaWinds third observation of Hurricane Frances (9/5/2004 10:30 UTC). Circles represent NEXRAD's estimated maximum useful range. Data right of the vertical line are in the nadir region of SeaWinds' swath.
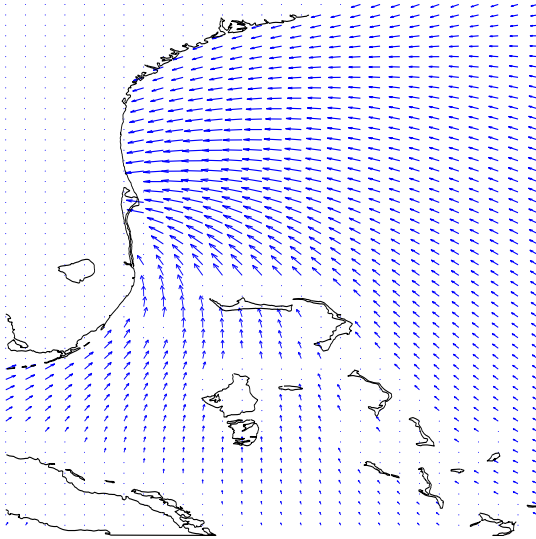
(a) NCEP wind vectors.
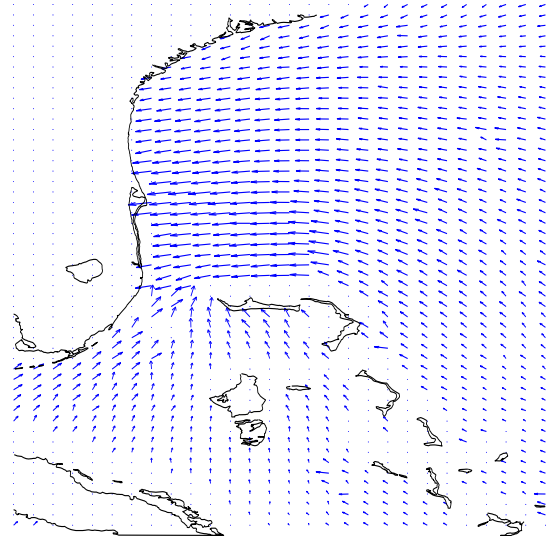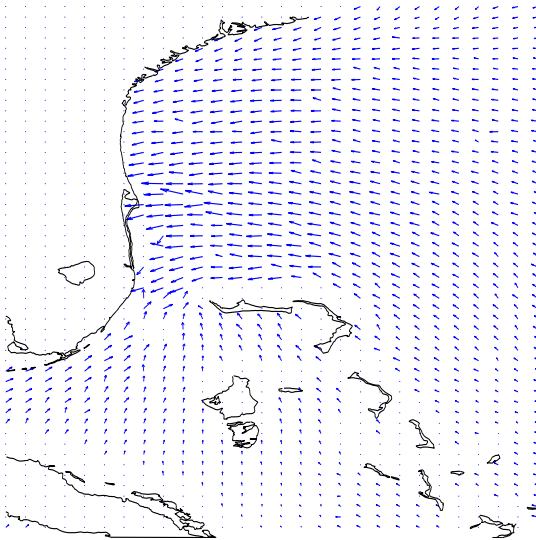
(b) L2B wind vectors.

(c) Draper wind vectors.
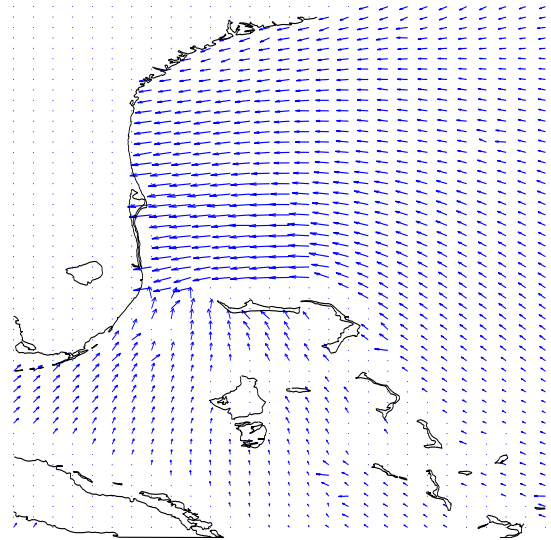
(d) L2B wind vectors with DIRTH smoothing.

Figure 3.21: Wind vectors from SeaWinds' third observation of Frances (9/5/2004 10:30 UTC). The L2B and DIRTH wind vectors exhibit rain induced squaring off between Florida and the Bahama islands.
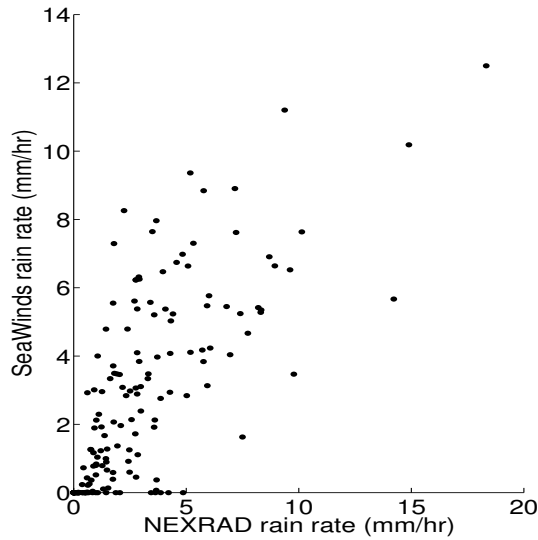
Figure 3.22: Scatter-plot of SeaWinds and NEXRAD rain rates for SeaWinds' final observation of Hurricane Frances. The correlation coefficient is 0.7413. The data consists of 171 points.

3.3 Summary

We observe that, on average, the Hurricane eyes and rain bands observed by both sensors are in the same location. We also note that the individual colocated rain estimates are noisy. This noise is especially prevalent in high wind/rain storms such as Hurricane Isabel and Frances. Table 3.1 displays the correlation coefficient of the rain observations from each case study as well as the correlation coefficient of all the rain information combined. Table 3.1 also presents the linear least square coefficients of each study in which the fit line is defined as

$$y = \mathrm{a}(1)x + \mathrm{a}(2), \tag{3.1}$$

where y is the Draper rain rate, x is the NEXRAD rain rate, and a(1) and a(2) are the coefficients shown in the table. We note that the linear least square coefficients are dependent on the scale factor discussed in Section 3.1.1.

Table 3.1: Correlation and linear least square fit coefficients for each case study.

Case Study Event	Correlation Coefficient	a(1)	a(2)
Low wind/rain	0.92	0.62	0.17
Isabel	0.68	0.80	0.74
Alex	0.82	0.55	0.33
Frances (1st observation)	0.77	0.83	0.48
Frances (2nd observation)	0.70	0.66	0.19
Frances (3rd observation)	0.74	0.69	0.64
Combined	0.75	0.66	0.54

Chapter 4

Analysis

In this chapter SeaWinds wind/rain estimation performance is analyzed, and conditions that change SeaWinds/NEXRAD rain rate correlation are explored. To facilitate analysis, a scatter-plot of SeaWinds and NEXRAD rain rates from all hurricane observations is displayed in Fig. 4.1(a). The 12.5 mm/hr limit on the Draper rain rate and general correlation can be seen. The combined correlation coefficient is 0.7456, which is approximately the correlation coefficients of monthly averages of QuikSCAT and TRMM Microwave Imager (TMI) data compared in [8].

The CDFs of the NEXRAD and SeaWinds rain rates for all hurricane events is displayed in Fig. 4.1(b). As previously discussed, the storm height estimate is calibrated so that the CDFs are matched on average.

The largest difference in the CDFs is when the rain rate is 12.5 mm/hr. The difference is caused by the rain rate ceiling imposed by the Draper method. The plot suggests that correlation may be improved by extending the ceiling to a higher rain rate. Nevertheless, we conclude that Draper rain rate estimates are reasonably accurate compared to NEXRAD. Further analysis follows.

4.1   Rain Flag Performance

Conventionally, rain contamination in WVCs is flagged by the multidimensional histogram (MUDH) algorithm [30]. This algorithm estimates the probability that a WVC is rain enhanced. The probabilities provided by the algorithm may then be used to flag rain enhanced WVCs.
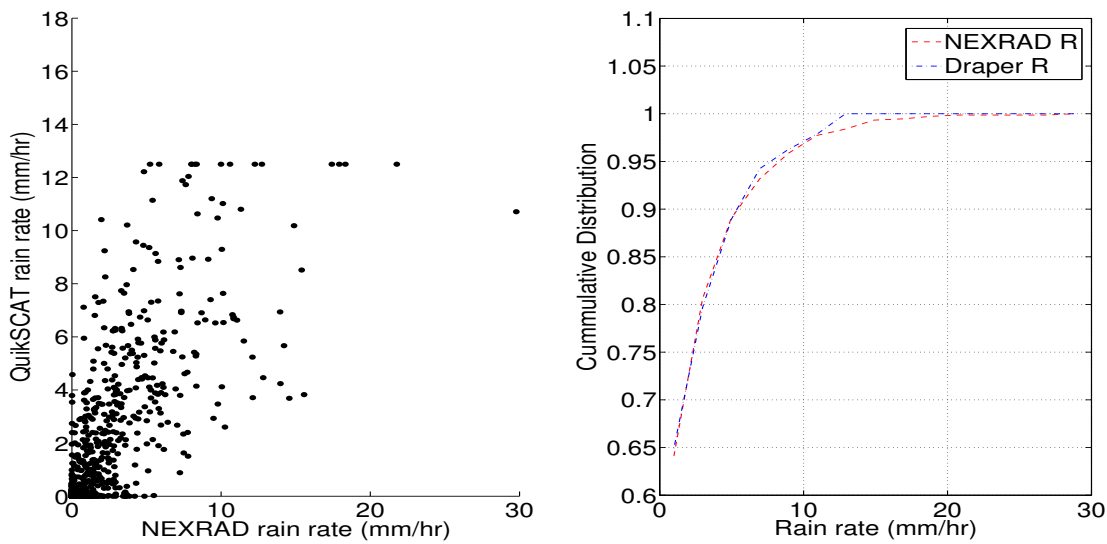
(a) Scatter-plot of SeaWinds and NEXRAD rain rates for all SeaWinds hurricane observations. The combined correlation coefficient is 0.7456.

(b) CDF of NEXRAD and Draper rain rates within NEXRAD's maximum useful range.

Figure 4.1: Integrated scatter-plot and histogram comparing SeaWinds and NEXRAD rain rates.

The Draper method can be converted to a rain flag algorithm by thresholding the rain rate. In this study the threshold is set at 2 mm/hr. Two performed metrics are then considered. The first is the "false alarm percentage", which is the percentage of WVCs where NEXRAD detects no rain and SeaWinds detects a rain rate greater than the threshold. The second metric is the "missed rain percentage", which is the percentage of WVCs in which the NEXRAD rain rate is greater than the threshold and SeaWind's rain rate is less than the threshold. The false alarm percentage for the Draper method is 0.13% and the missed rain percentage is 8.17%.

Draper rain flag performance may be compared to the MUDH rain flag through thresholding. The MUDH threshold is set by determining which probability threshold flags the same percentage of WVCs as the 2 mm/hr NEXRAD threshold. For the hurricane cases, the MUDH threshold is 90%, the MUDH false alarm percentage is

0.40% and the missed rain percentage is 8.97%. The comparison metrics are somewhat larger than corresponding Draper rain flag percentages, and we conclude that the Draper algorithm provides an improved rain flag.

4.2 Wind Vector Analysis

In this section we examine wind vectors estimated by the Draper method. For this analysis the data window is expanded to include all WVCs shown in the wind/rain observation plots in Section 3.2. For evaluation purposes, the Draper wind vectors are compared with NCEP and L2B wind vectors. Draper, L2B, and NCEP wind speed direction maps for each of the hurricane events are displayed in the wind vector plots in Figs. 3.6, 3.11, 3.15, 3.18, and 3.21. Wind directions are in degrees clockwise from North, and speeds are in m/s.

NCEP wind vectors are trilinearly interpolated (in space and time) wind vectors from a $2.5° \times 2.5°$ latitude-longitude grid with a temporal resolution of 6 hours [7]. L2B wind vectors are vectors retrieved through the conventional SeaWinds wind retrieval. DIRTH winds are similar to conventional L2B winds, but have been estimated by the DIRTH algorithm.

Case study wind vector figures show that the NCEP winds are over-smoothed. This is expected due to the lower resolution of the NCEP wind vector estimates. The DIRTH winds are similar to the NCEP winds. The L2B winds are not as smooth as the NCEP or DIRTH winds. However, L2B wind vectors exhibit squaring off in some rainy areas. For example, Fig. 3.17(d) exhibits squaring off just north of the hurricane eye.

Squaring off is caused by increased $\sigma°$ in rain enhanced WVCs. The rain model in Eq. (2.2) shows that rain simultaneously increases and decreases σ_w by inducing additional surface capillary waves while attenuating the airborne signal. In most rain events the increased signal from additional capillary waves dominates airborne attenuation [6] and rain affected σ_w is greater than the zero rain σ_w.

As a function of azimuth angle, the conventional GMF is a double cosine function with peaks at $0°$ and $180°$ relative azimuth angle. Rain effects suppress σ_w,

and cause the azimuth dependency of σ° to decrease. This causes σ° to be constant for all measurements. This increases the probability that the estimated wind direction is either the direction of the vector from the spacecraft to the measured area or the vector from the measured area to the spacecraft. Figure 4.2 illustrates observation geometry for equally spaced SeaWinds observations of a WVC in the sweet spot. Rain dominated σ° measurements result in wind vector estimates than are parallel or antiparallel to the measurement vector. In cyclonic storms this yields squared off wind vectors.
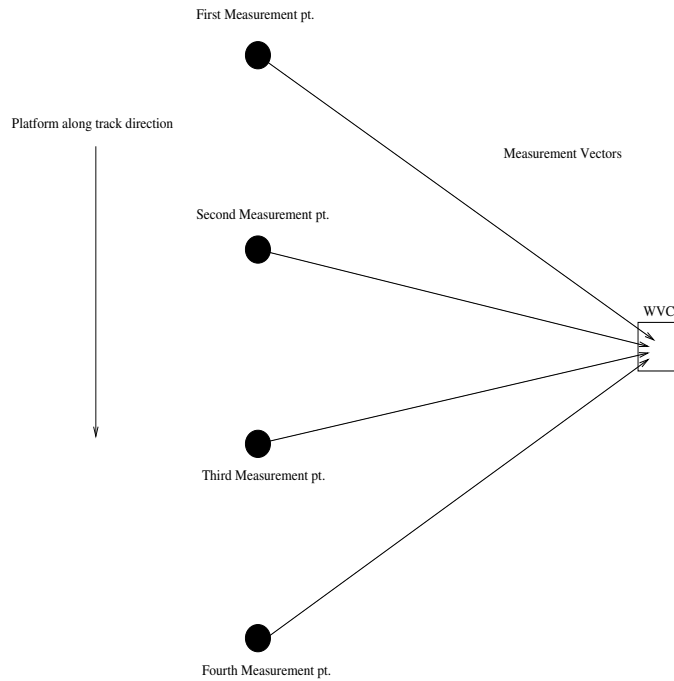
Figure 4.2: SeaWinds measurement geometry from a WVC in the sweet spot. If σ° is sufficiently increased due to rain, wind vector estimates from each measurements tend to be either parallel or antiparallel to the measurement vector.

Figure 4.3 displays histograms of the L2B and Draper relative wind direction estimates from WVCs in which the Draper algorithm finds the rain rate is less than 1 mm/hr. Wind directions are relative to the along track direction of the platform. The nonraining histogram distributions are similar and appear approximately uniform.

Figure 4.4 displays relative wind direction histograms in areas in which the Draper rain rate is greater than 1 mm/hr. The directional distribution in Fig. 4.4(a) exhibits the effects of squaring off. The histogram has large peaks near 0° and 180° and smaller peaks near 90° and 270°. Few direct estimates for L2B winds have off track directions such as 60°. On the other hand, the Draper wind directions in Fig. 4.4(b) have a distribution closer to uniform, which is the expected result.
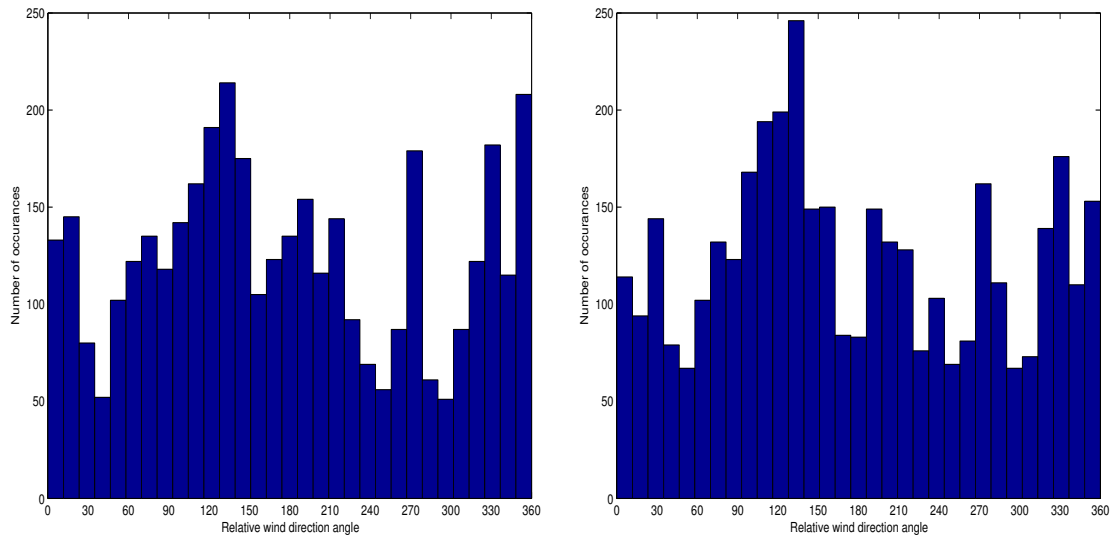
(a) L2B relative wind direction histogram.

(b) Draper relative wind direction histogram.

Figure 4.3: Relative wind direction estimates for L2B and Draper winds in non-raining (rain rate < 1.0 mm/hr) areas. In both cases the relative wind directions are approximately uniformly distributed throughout all wind directions.
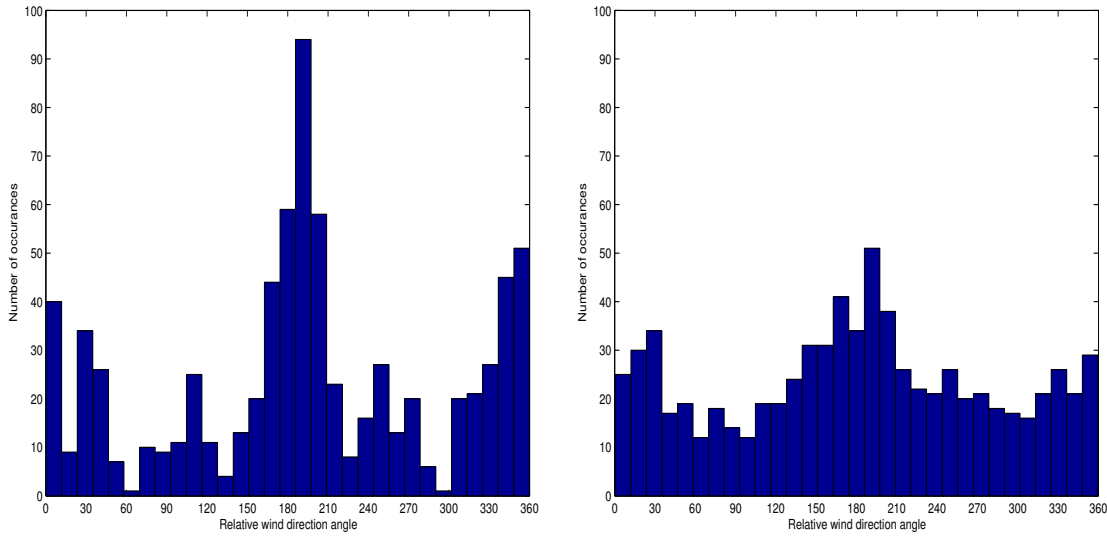
(a) L2B relative wind direction histogram.

(b) Draper relative wind direction histogram.

Figure 4.4: Relative wind direction estimates for L2B and Draper winds in rainy areas (rain rate > 1.0 mm/hr). The L2B histogram exhibits squaring off. The histogram has large peaks near 0° and 180° and smaller peaks near 90° and 270°. The Draper wind vectors are nearly uniformly distributed, and exhibit less squaring off effects.

Unfortunately, Draper wind vectors are the noisiest of the displayed winds, in both raining and nonraining cases. This noise is exhibited in all Draper wind vector plots and is most prevalent in Fig. 3.18(d). Although they have less over-smoothing and squaring off.

Scatter-plots comparing Draper, NCEP and L2B wind speeds and directions for all events, are displayed in Figs. 4.5 and 4.6. The scatter-points are color coded by the Draper rain rate. To ease comparison, wind directions are compared by adding the minimum angle between the two wind estimates to the Draper wind direction estimate.

NCEP wind vector estimation is independent of SeaWinds measurements. Wind field figures displayed in Section 3.2 support the conclusion that NCEP winds

are also independent of local rain. Scatterplots of Draper and L2B wind speeds and directions for all data within the regional analysis are displayed in Figs. 4.5 and 4.6. Wind vector differences are largest in near cross-swath directions, and wind speed discrepancies are largest in heavier rains.

Wind direction discrepancies between the Draper and L2B vectors increase near 90° and 270°. This is due to estimation degradation in cross track winds [7] – the effects of "squaring off" in the L2B data. It can also be seen that in the near cross swath directions nearly all WVCs are estimated to have no rain. In those directions the Draper method may be unable to retrieve rain rate estimates.

As rain rate increases, the Draper method generally estimates a lower wind speed than the current L2B method [6]. This effect is not seen in Draper/NCEP wind comparisons. In the mean sense, Draper wind estimates exhibit fewer squaring off effects and are a closer match to NCEP estimates. However, Draper wind estimates also have greater variability than the variability observed in L2B winds.

4.3 Swath Location Effects

An important factor in SeaWinds wind/rain estimation accuracy is swath location. As previously noted, instrument skill degrades in nadir regions which may cause wind/rain retrieval accuracy degradation. Figure 4.7 compares scatter-plots from estimated rain rates within the sweet spot and the nadir region of the swath for all case studies. Neither plot exhibits exceptionally higher correlation than the other. However, the correlation coefficient of the data from the sweet spot is 0.7665 while the correlation coefficient of data collected in the nadir region is 0.7092.

4.4 Regime Thresholding

In this section we examine wind and rain estimation for each of the regimes described in Section 2.2. It is expected that rain rates may be readily estimated for WVCs in regime 1, but not in regime 3 [23]. Also, we expect that wind estimates can only be made for regimes 2 and 3. Figure 4.8 displays the regime estimates for SeaWinds' second observation of Hurricane Frances. We note that areas distant to the
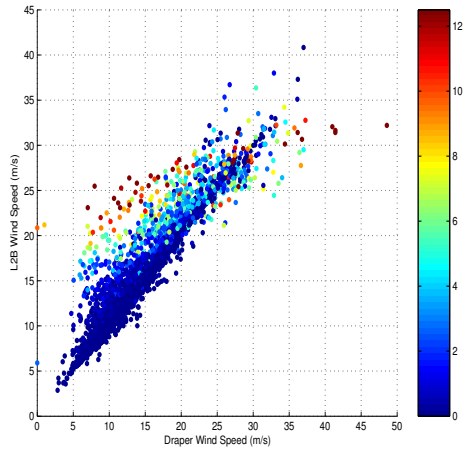
(a) Draper wind speed vs. L2B wind speed (m/s).
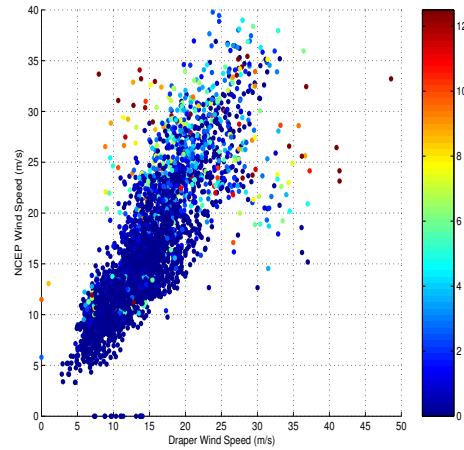
(b) Draper wind speed vs. NCEP wind speed (m/s)
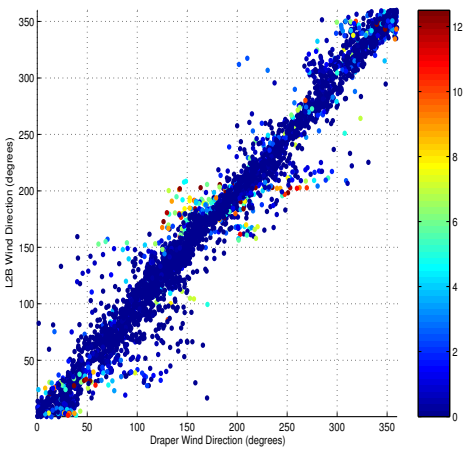
(c) Draper wind direction vs. L2B wind direction (degrees).
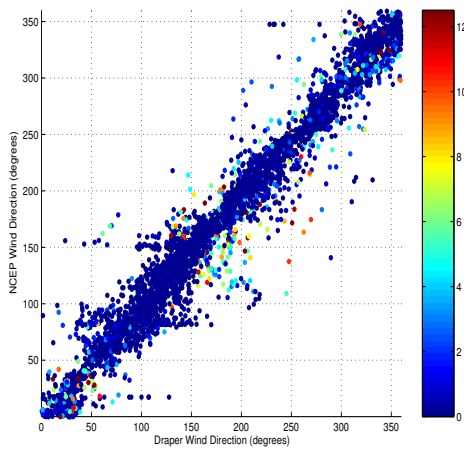
(d) Draper wind direction vs. NCEP wind direction (degrees).

Figure 4.5: Comparisons of NCEP and L2B wind vectors vs. wind vectors found from the Draper model for all hurricane events. Points are color coded by Draper rain rate (mm/hr). In general, the Draper model estimates lower wind speeds. Also, wind direction estimation degradation in near cross swath winds is observed. The variability of wind speed and direction estimates increases with rain intensity.
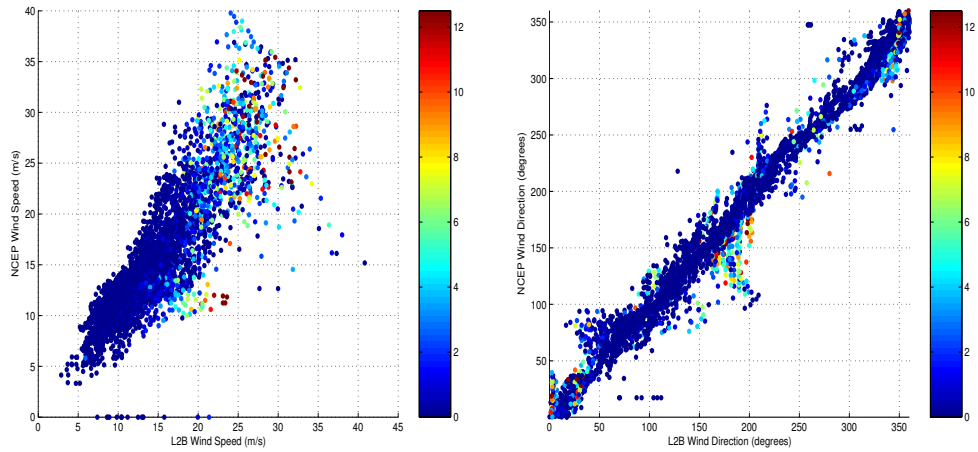
(a) NCEP wind speed vs. L2B wind speed (m/s).

(b) NCEP wind direction vs. L2B wind direction (degrees).

Figure 4.6: Comparisons of NCEP and L2B wind speeds and directions. Points are color coded by the Draper rain rate (mm/hr) of the WVC. The wind vector distribution is similar to the NCEP verses Draper wind vectors in Fig. 4.5.
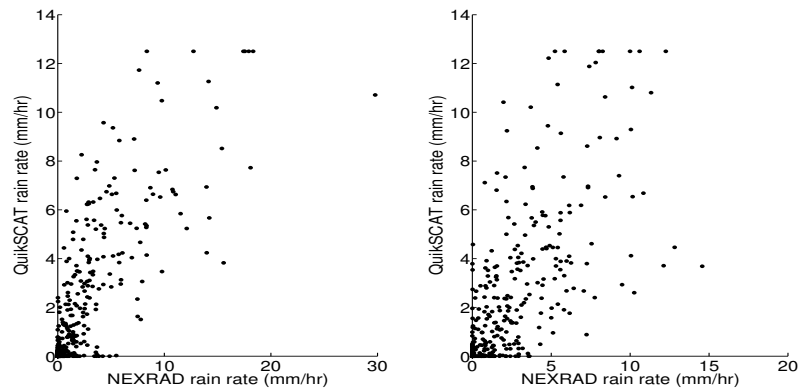
(a) Scatter-plot of combined data within the sweet spot of SeaWinds' swath. The data consists of 450 points.

(b) Scatter-plot of combined data within the nadir region of SeaWinds' swath. The data consists of 382 points.

Figure 4.7: Scatter-plots of combined hurricane rain rate data from the sweet spot and nadir regions of SeaWinds' swath. The data from the sweet spot has a correlation coefficient of 0.7665 and data from the nadir region has a correlation coefficient of 0.7092.

hurricane or inside the hurricane eye are classified in regime 3, where wind dominates the backscatter. Regime 2 covers most of the eye-wall and outer rain bands, where rain and wind effects are of the same order. Points classified in regime 1 are in the center of the outer rain bands and a few eye-wall points, where σ° is dominated by rain.

Regime scatter-plots of NEXRAD and SeaWinds rain rates from the case studies are displayed in Fig. 4.9. Most WVCs with high SeaWinds and NEXRAD rain rates are in regime 1. WVCs with low SeaWinds and NEXRAD rain rates are in regime 3. Regime 2 contains a mix of relatively high and low rain rates.

The correlation coefficients for the first, second, and third regimes are 0.5884, 0.6066, and 0.3946 respectively. Low correlation in regime 3 is expected because σ° in the regime is wind-dominated and rain rate estimation is poor. However, rain in regimes 1 and 2 exhibit improved correlation as rain increasingly dominates the measured backscatter.

We note that the correlation coefficient of each regime is less than the correlation coefficient of the combined data set (0.7200). This is due to the separation of the data in regime 3 from the other regimes. Regime 3 rain rates are smaller than rates from the other regimes. This data reduces the variance of the individual rain sets and increases the correlation coefficient of the combined set.

Rain data in regime 1 does not exhibit improved correlation over regime 2 rain. This may be due to interference from σ° induced by wind, although the fixed storm height calibration factor discussed in Section 3.1.1 may be playing a role. The Draper method attempts to estimate rain and wind for all regimes. Regime 1 σ° is rain dominated and wind information is suppressed. By attempting to retrieve wind in regime 1 the algorithm may add variability to the rain estimates. Regime 1 rain estimates may be improved by performing rain-only retrieval.
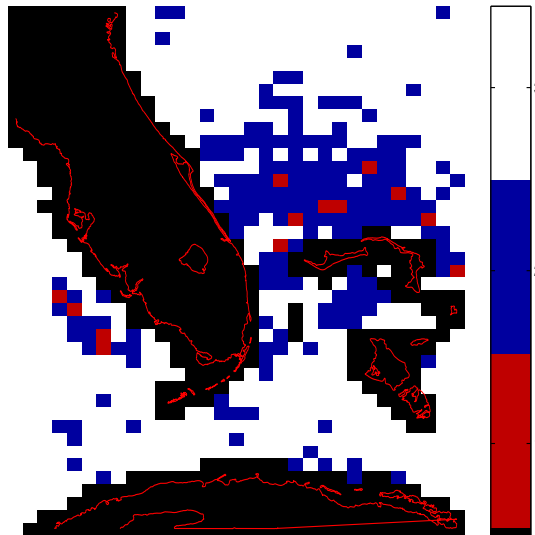
Figure 4.8: Regimes of each WVC for SeaWinds' second observation of Hurricane Frances. Most WVCs in the outer rain bands and near the eye of the hurricane are classified in regime 2. The eye and points distant from the hurricane are classified in regime 3. Few WVCs are classified in the rain dominated regime 1.
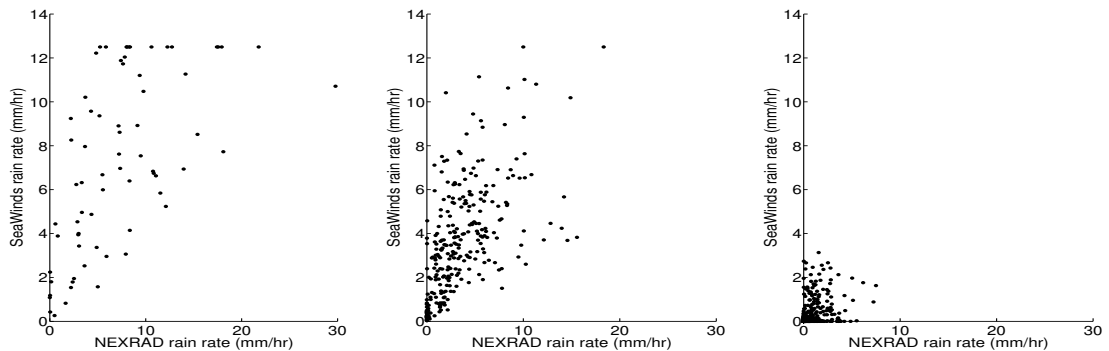
(a) Regime 1, rain dominated $\sigma°$. The data correlation coefficient is 0.5884 and consists of 70 points.

(b) Regime 2, wind and rain effects on $\sigma°$ are the same order of magnitude. The data correlation coefficient is 0.6066 and consists of 283 points.

(c) Regime 3, wind-dominated $\sigma\circ$, rain is not observable. The data correlation coefficient is 0.3946 and consists of 479 points.

Figure 4.9: Scatter-plot of NEXRAD vs. SeaWinds rain rates for each regime.

4.5 Rain-only Retrieval

A rain-only retrieval algorithm is developed by forming a rain-only GMF (M_{rain}). That is,

$$M_{rain} = \sigma_e(R), \tag{4.1}$$

where $\sigma_e(R)$ is a quadratic function of R as described in [6]. The rain rate is determined by finding the least squared error $[e(R_{dB})]$ of each measurement and the model function for each measurement,

$$e(R_{dB}) = \sum_{i=1}^{n} (\hat{\sigma}_i - \sigma_{ei}(R_{dB}))^2, \tag{4.2}$$

where R_{dB} is the rain rate in dB normalized to 1 mm/hr, $e(R_{dB})$ is the error function, $\hat{\sigma}_i$ is the SeaWinds i^{th} $\sigma°$ measurement for the WVC of interest, and $\sigma_{ei}(R_{dB})$ is the GMF for the ith measurement and n is the number of $\sigma°$ measurements in the WVC. $e(R_{dB})$ is minimized by taking the derivative of Eq. (4.2), setting it to zero, and dropping constant terms. Since σ_{ei} is a quadratic function, the derivative of Eq. (4.2) is the cubic function

$$\sum_{i=0}^{3} \gamma_i R_{dB}^n = 0, \tag{4.3}$$

where the constant terms γ_i are determined by the constants in each $\sigma_{ei}(R_{dB})$ and the SeaWinds measurements. Eq. (4.3) is solved by the cubic equation and R_{db} is set to the real root that minimizes $e(R_{dB})$.

In order for rain-only retrieval to be accurate, wind contributions to $\sigma°$ must be negligible. Areas where wind-only retrieval are performed are restricted to the rain-dominated regime 1, as identified by the simultaneous wind/rain retrieval algorithm. Figure 4.10 displays SeaWinds and NEXRAD rain rate estimates for simultaneous wind/rain and rain-only retrieval for the low wind/rain case. In regime 1, the correlation coefficient of the Draper rains with NEXRAD colocated rains is slightly improved from 0.8785 to 0.8896. It also appears that the variance of the rain estimates decreases. Additionally, the instance where simultaneous wind/rain retrieval

produces a rain rate estimate of 4.2 mm/hr and NEXRAD estimates nearly no rain at all is reduced to 2.1 mm/hr.

Correlation of regime 1 data from Hurricane Alex is also increased through the use of rain-only retrieval. However, in the other Hurricane events which have larger winds, correlation with NEXRAD rains decreases when rain-only retrieval is performed. An example of this is displayed in Fig. 4.11 where rain-only retrieval is performed for regime 1 data in the first observation of Hurricane Frances. In this case correlation is decreased to 0.3917, and several more points show a saturated rain rate. We speculate that this is most likely due to misclassification of the data regime and higher wind speeds. In most of the points, wind is a large contributor to $\sigma°$ and the rain rate is overestimated. Similar results are seen in the second observation of Hurricane Frances and in Hurricane Isabel, both of which are high wind/rain events.

4.6   Regime Wind Detection

To explore regime-based wind estimation, Figs. 4.12, 4.13 and 4.14 display wind speed and direction scatter-plots of Draper, L2B, and NCEP winds for each regime. We note that in regime 1, rain dominates the backscatter and the wind estimates are expected to be poor, and that the rain-only algorithm should be used. As expected regime 1 winds are noisier than other winds, and the wind speeds exhibit more inconsistencies. Also, no WVCs with NCEP or L2B wind directions near 270° are classified in regime 1. This may be due to poor measurement geometry for such wind directions.

Regime 3 winds are more consistent and exhibit less noise than the other regions. L2B and Draper wind estimates in this region are similar. This is due to low rain influence on $\sigma°$. Also, rain rate information in regime 3 is generally unobtainable due to low rain effects relative to the wind.
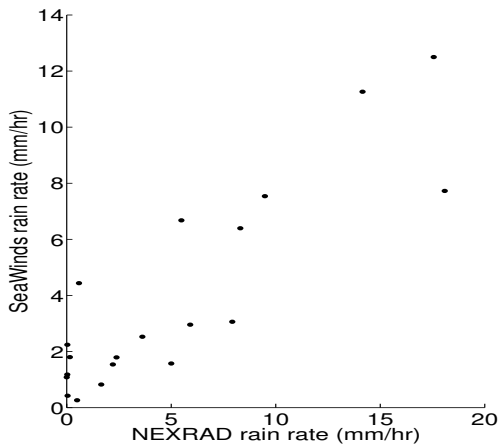
(a) Simultaneous wind/rain retrieval results. The data correlation coefficient is 0.8785 and consists of 20 points.
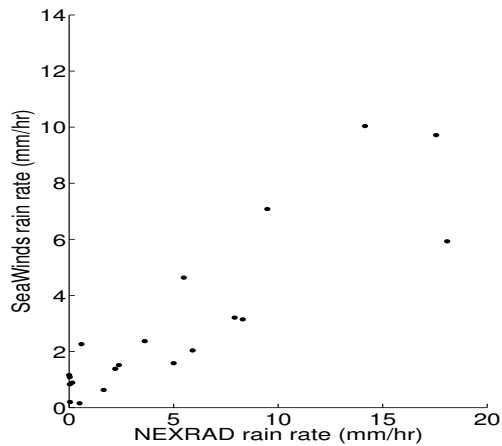
(b) Rain-only retrieval results. The data correlation coefficient is 0.8896 and consists of 20 points.

Figure 4.10: Scatter-plot of NEXRAD vs. SeaWinds rains for simultaneous wind/rain and rain-only retrieval in regime 1 WVCs from the low wind/rain case (8/27/2004).
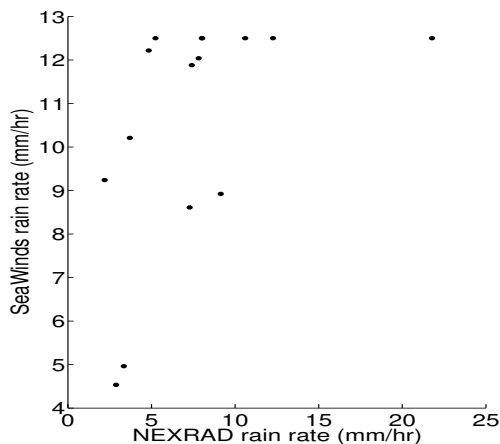
(a) Simultaneous wind/rain retrieval. The data correlation coefficient is 0.5014 and consists of 15 points.
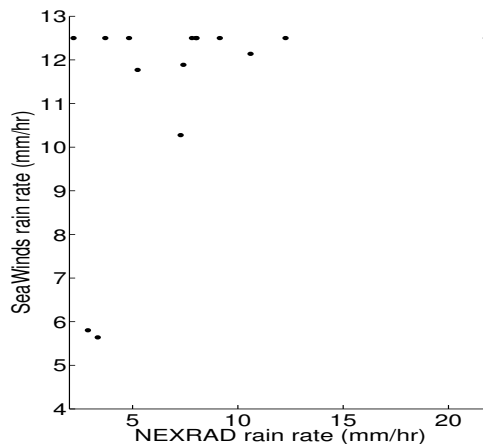
(b) Rain-only retrieval results. The data correlation coefficient is 0.3917 and consists of 15 points.

Figure 4.11: Scatter-plot of NEXRAD vs. SeaWinds rains for simultaneous wind/rain and rain-only retrieval in regime 1 WVCs from the first observation of Hurricane Frances (9/4/2004 10:55 UTC).
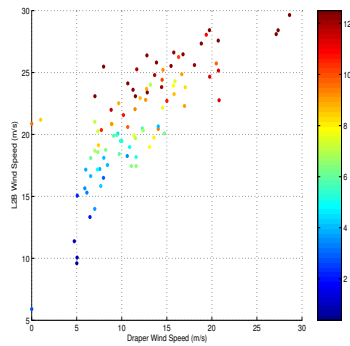
(a) Regime 1, L2B vs. Draper wind speed.
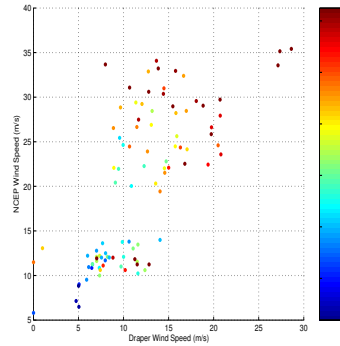
(b) Regime 1, NCEP vs. Draper wind speed.
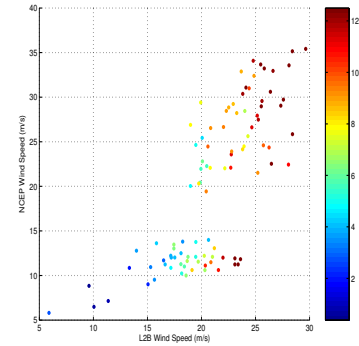
(c) Regime 1, NCEP vs. L2B wind speed.
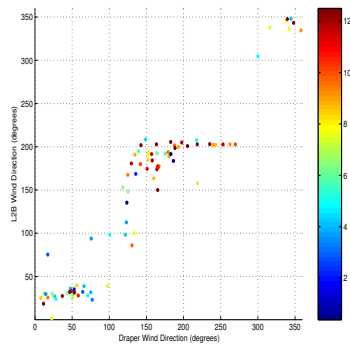
(d) Regime 1, L2B vs. Draper wind direction.
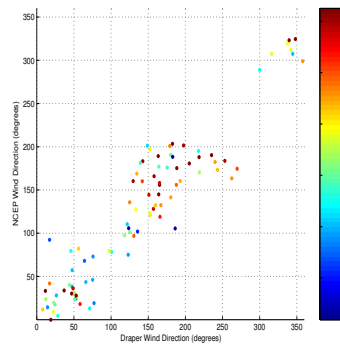
(e) Regime 1, NCEP vs. Draper wind direction.
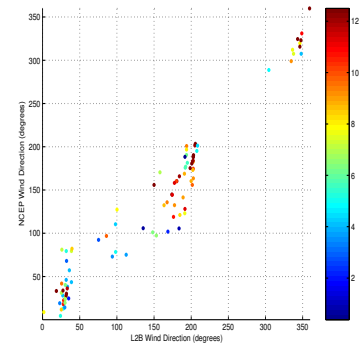
(f) Regime 1, NCEP vs. L2B wind direction.

Figure 4.12: Rain dominated regime 1 wind scatter-plots for all events. Scatter-points are color-coded by Draper rain rate.
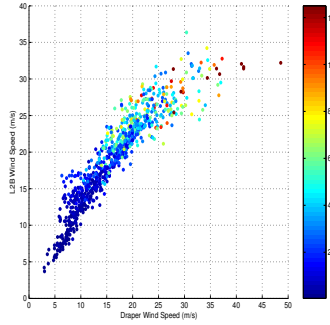
(a) Regime 2, L2B vs. Draper wind speed.
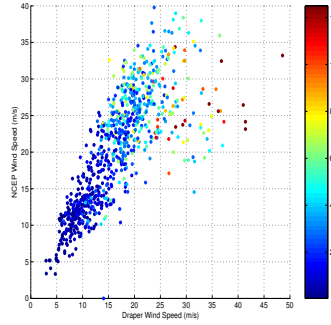
(b) Regime 2, NCEP vs. Draper wind speed.
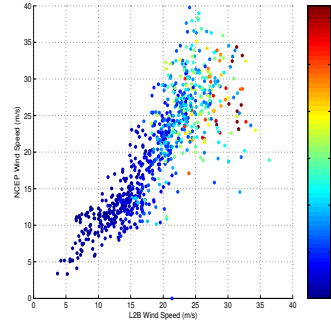
(c) Regime 2, NCEP vs. L2B wind speed.
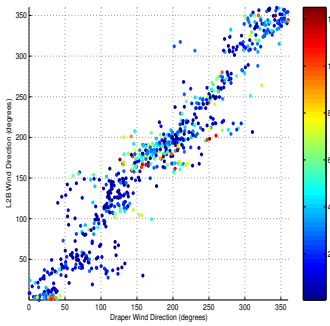
(d) Regime 2, L2B vs. Draper wind direction.
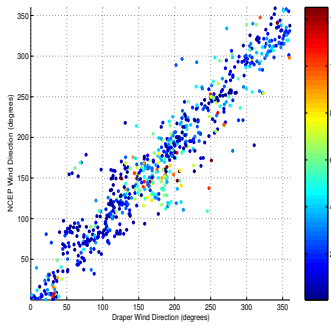
(e) Regime 2, NCEP vs. Draper wind direction.
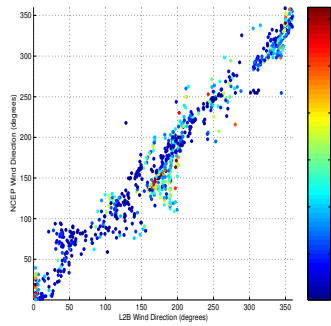
(f) Regime 2, NCEP vs. L2B wind direction.

Figure 4.13: Regime 2, where wind and rain contributions to σ° are of the same magnitude, wind scatter-plots for all events. Scatter-points are color-coded by Draper rain rate.
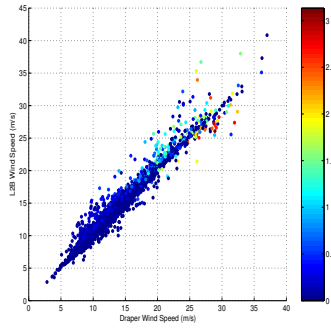
(a) Regime 3, L2B vs. Draper wind speed.
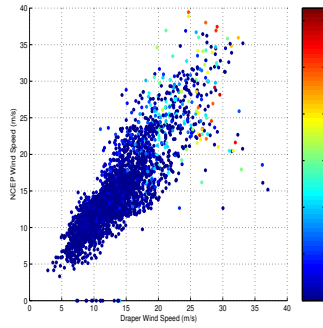
(b) Regime 3, NCEP vs. Draper wind speed.
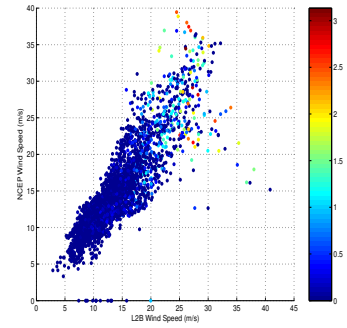
(c) Regime 3, NCEP vs. L2B wind speed.
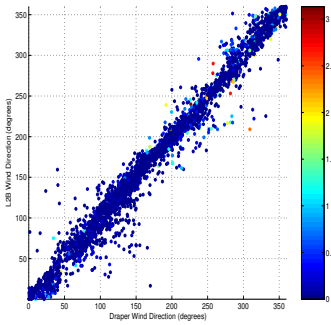
(d) Regime 3 L2B vs. Draper wind direction.
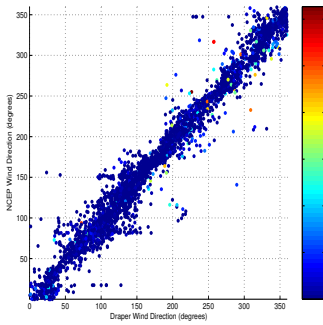
(e) Regime 3, NCEP vs. Draper wind direction.
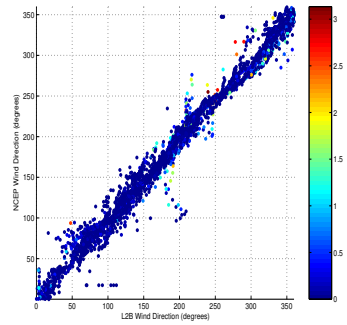
(f) Regime 3, NCEP vs. L2B wind direction.

Figure 4.14: Regime 3, where σ° is wind dominated, wind scatter-plots for all events. Scatter-points are color-coded by Draper rain rate.

Chapter 5

SeaWinds Rain Variability Estimation

In this chapter we analyze the variability of SeaWinds rain estimates. This is done by identifying noise sources and estimating their contributions to the total rain estimate variability. In order to facilitate this analysis, a simple noise model is introduced. From the model we use Monte-Carlo simulation to find the rain estimate variability. After finding the rain estimate variability, we employ rain-only retrieval to estimate the noise on $\sigma°$ that causes the simulated rain rate variability. Known SeaWinds noise parameters (the so-called communications K_p [16]) are compared to the estimated $\sigma°$ noise to infer the relative magnitude of rain estimation noise due to GMF error, beamfilling, and imperfect colocation.

In order to examine SeaWinds/NEXRAD rain rate estimation variability we create a simple noise model. The model is used to express the variability of sensor rain rate estimates. In order to generate the noise model, sources of NEXRAD and SeaWinds estimation error are analyzed. While a realistic rain rate variability model must allow for systematic, deterministic "calibration", and random errors, we focus primarily of random errors.

A source of error in NEXRAD rain estimates is error in Z detection. NEXRAD return power (P_r) is estimated from the returned signal envelope through a combination of time and range averaging. Averaging is performed to reduce the standard deviation (σ) of the Z estimate to 1 dB [24]. Figure 5.1 displays hurricane rain rate verses Z $\pm\sigma$. The difference between the σ envelope edges increases with rain rate. Figure 5.2 displays the σ difference between the zero noise rain rate and the rain rate when the Z estimate differs from the true Z by $\pm\sigma$. NEXRAD's rain rate estimation

σ in hurricane events for rain rates greater than 2 mm/hr is approximately $0.2R$. In absence of other factors, the NEXRAD rain rate (R_{NEXRAD}) observation model is related to the true rain rate (R_{true}) by

$$R_{\text{NEXRAD}} = |R_{\text{true}}(1 + \alpha_1 \nu_1)|, \tag{5.1}$$

where $\alpha_1 = 0.2$ and ν_1 is a zero mean, random variable with unit variance. The absolute value operator is used because reported rain must be non-negative to be physically realistic. Due the large number of independent scatterers and Z estimation error sources, ν_1 is assumed to be Gaussian by the central limit theorem.
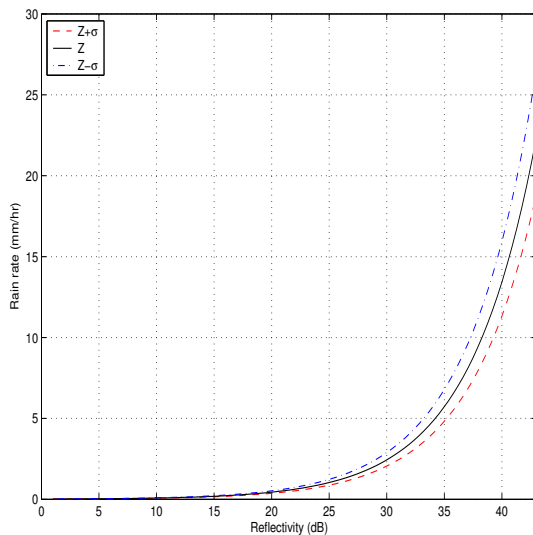
Figure 5.1: NEXRAD rain rate verses reflectivity. Rain rate is plotted as a function of Z with $\pm\sigma$ envelopes. The solid line is the nominal Z-R relationship, and the dotted lines show the relationship when Z = Z $\pm\sigma$ where $\sigma = 1$ dB.
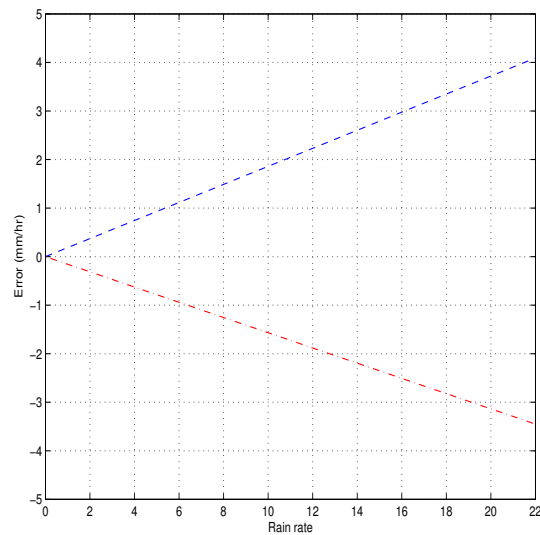
Figure 5.2: Differences between calculated and true rain rate for Z $\pm\sigma$ The standard deviation of the rain rate estimation is approximately 0.2R, where R is the true rain rate.

Random noise in SeaWinds based rain estimates comes from several sources. Thermal emissions, amplifier noise, errors in path attenuation estimates [8], and other sources contribute to random error. The behavior of the rain rate scatter plots in this thesis suggests that Draper rain estimation error can be modeled as additive noise.

Thus, we model SeaWinds rain (R_{SeaWinds}) estimates as

$$R_{\text{SeaWinds}} = |R_{\text{true}} + \alpha_2 \nu_2|, \tag{5.2}$$

where α_2 is constant and ν_2 is a unit variance zero mean Gaussian random variable. Combining Eqs. (5.1) and (5.2) yields

$$R_{\text{SeaWinds}} = |R_{\text{NEXRAD}}(1 + \alpha_1 \nu_1) + \alpha_2 \nu_2|, \tag{5.3}$$

where ν_1 and ν_2 are uncorrelated Gaussian random variables with zero mean and unit variance, α_1 and α_2 are the standard deviations of the additive SeaWinds and NEXRAD estimation errors.

Additionally, AMSR rain (R_{AMSR}) measurements are modeled in a fashion similar to SeaWinds rain. Assuming additive Gaussian noise ν_3, with $\sigma = \alpha_3$

$$R_{\text{AMSR}} = |R_{\text{true}} + \alpha_3 \nu_3|. \tag{5.4}$$

Combining Eqs. (5.2) and (5.4) gives

$$R_{\text{AMSR}} = |R_{\text{SeaWinds}} + \alpha_2 \nu_2 + \alpha_3 \nu_3|. \tag{5.5}$$

Since the scatter-plots comparing SeaWinds to NEXRAD and AMSR to NEXRAD [Figs. 3.7 and 3.9(a)] have similar correlation, it is reasonable to assume that α_2 and α_3 are on the same order.

5.1 Simulation

In order to perform Monte-Carlo simulation, the distribution of instantaneous columnar rain rate is needed. Figure 5.3 displays the CDFs of the NEXRAD and Draper rain rates for all cases previously studied with a scaled exponential CDF with the same mean and variance as the NEXRAD rain rate. The exponential and NEXRAD CDFs exhibit differences in low rain rates. However, in this first order simulation, the CDFs exhibit enough similarity that it is reasonable to model the distribution of Hurricane rain as exponential with the mean and variance of the NEXRAD rain rate.
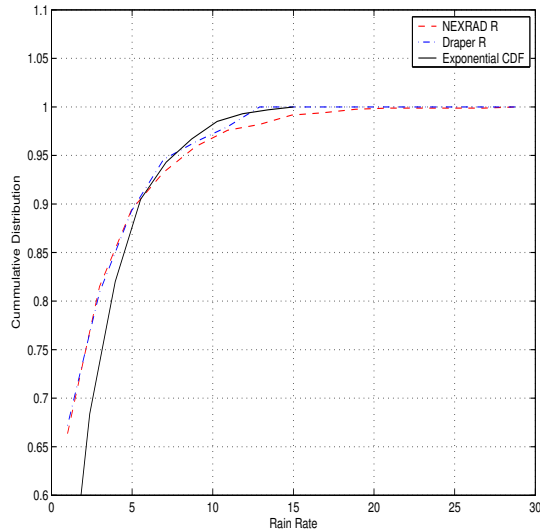
Figure 5.3: Cumulative distribution functions of the NEXRAD and Draper rain rates for all hurricane events and an exponential distribution with the same mean and variance as the NEXRAD rain rates.

We perform Monte-Carlo simulation by first creating 1000 exponentially distributed realizations of R_{NEXRAD} for each of several values of α_2. Then, Eq. (5.3) is used to find R_{SeaWinds} for each realization. Finally, the correlation coefficient of the R_{NEXRAD} and R_{SeaWinds} realizations is determined for each value of α_2.

The results of the Monte-Carlo simulation are displayed in Figure 5.4(a) as plot of α_2 verses the correlation coefficient. The correlation coefficient nears 0.75 (the approximate correlation of real R_{SeaWinds} and R_{NEXRAD} rain estimates) when $\alpha_2 \approx 2.5$. For illustration, the scatter-plot of the first 100 simulated NEXRAD and SeaWinds rain estimates for the simulation with $\alpha_2 = 2.5$ is displayed in Fig. 5.4(b). The scatter-plot is similar to the scatter-plots found for the hurricane events.
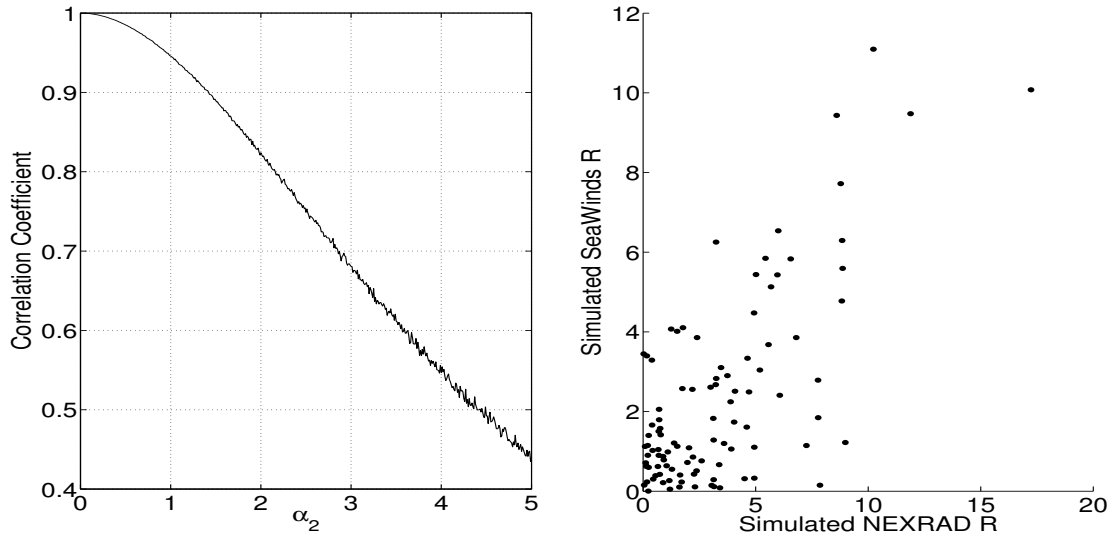
(a) α_2 verses correlation coefficient for the additive noise Monte-Carlo simulation. Correlation nears 0.75 when α_2 is 2.5.

(b) Scatter plot of the additive noise Monte-Carlo simulation at $\alpha_2 = 2.5$

Figure 5.4: Monte-Carlo simulation results for the simple SeaWinds/NEXRAD noise model.

Our simulation suggests that we may treat total additive noise on SeaWinds rain estimations as a zero mean Gaussian random variable with a standard deviation of 2.5. Draper and Long estimated that SeaWinds rain retrieval is generally within 3 dB of the true rain [7]. Monte-Carlo simulation for Hurricane rains shows that the standard deviation of the SeaWinds rain estimate is within 3 dB of the true rain for all rates greater than 6 km mm/hr, which confirms the error estimate of [7].

5.1.1 Multiplicative Noise

For completeness we evaluate a simple noise model in which the SeaWinds rain retrieval noise is multiplicative. In multiplicative form the noise model becomes

$$R_{\text{SeaWinds}} = \left| R_{\text{NEXRAD}} \frac{(1 + 0.2\nu_2 R)}{(1 + \alpha_1 \nu_1)} \right|. \tag{5.6}$$

The Monte-Carlo simulation is repeated with the multiplicative noise model. Figure 5.5(a) displays correlation coefficient verses α for the simulation. At $\alpha \approx 0.26$ the correlation coefficient nears 0.75. Figure 5.5(b) shows the R_{SeaWinds} verses R_{NEXRAD} scatter plot for the simulation when α is 0.26. This scatter-plot pattern differs from real data scatter-plots. Figure 5.5(b) exhibits less noise at low rain rates, and greater noise at low rain rates than the actual data. We conclude that the contribution of multiplicative noise is small compared to the additive noise contribution.
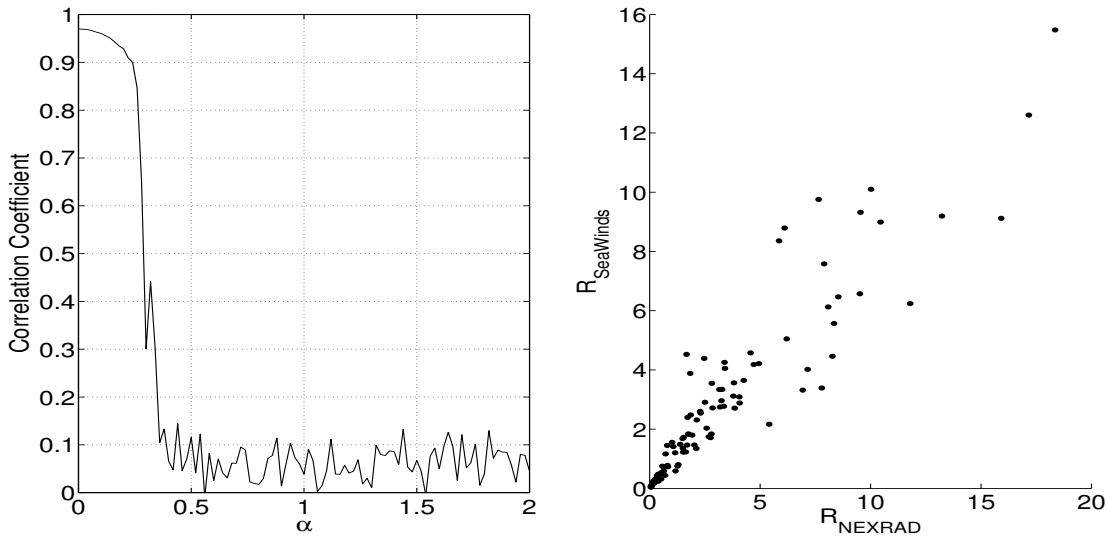
(a) α_1 verses correlation coefficient for multiplicative noise Monte-Carlo simulation. Correlation nears 0.75 when α_1 is 0.26.

(b) Scatter plot of the multiplicative noise Monte-Carlo simulation at $\alpha_1 = 0.4$

Figure 5.5: Multiplicative noise Monte-Carlo simulation results.

5.2 Noise Sources

As noted in section 2.3.1, rain estimation error is caused by three main sources, communication error, beamfilling, and imperfect colocation. By simulating SeaWinds rain retrieval we may compare the error caused by the communication noise to the

error caused by beamfilling and imperfect colocation. In order to simplify the simulations, we simulate regime 1 retrieval. Since σ° in regime 1 is rain dominated, we may use rain-only retrieval to calculate the effect of noise on rain estimates.

Rain-only retrieval relates $\sigma^\circ_{\mathrm{dB}}$ to R_{dB} through a quadratic equation. Analytic computation of σ° noise effects on R estimation is complex. To simplify the problem, Monte-Carlo simulation is employed.

We perform the simulation by creating several thousand samples of R, with the exponential random variable described in Section 5.1. The samples are scaled to cancel the calibration constant described in Section 3.2.1. σ° corresponding to each sample is then calculated through the rain-only model function. The SeaWinds instrument generally makes between 4 and 8 measurements of each WVC in the inner beam region. To simulate these measurements, zero mean Gaussian noise with standard deviation α is added to six copies of each σ° realization to create six noisy samples of σ° for each sample of R. Rain-only retrieval is performed using the noisy σ° samples to determine the estimated rain rate R_{est}. R_{error} is calculated by subtracting R_{est} from the scaled R. The amount of noise in R is calculated as the standard deviation in R_{error}. This simulates SeaWinds σ° measurements in rain dominated regions.

We have found that the rain retrieval noise is dominated by additive noise. However, in order to facilitate a comparison of rain estimation and communication noise, we determine K_{pr}, the normalized standard deviation of the additive noise in the σ° realizations. We define K_{pr} as

$$K_{pr} = \frac{\alpha}{\sigma^\circ_{\mathrm{ave}}}, \tag{5.7}$$

where $\sigma^\circ_{\mathrm{ave}}$ is the average realization of σ° and α is the additive noise standard deviation. Figure 5.6 displays the standard deviation of R_{error} verses K_{pr}. The standard deviation of the R estimates is 2.5 when K_{pr} is approximately 0.18.
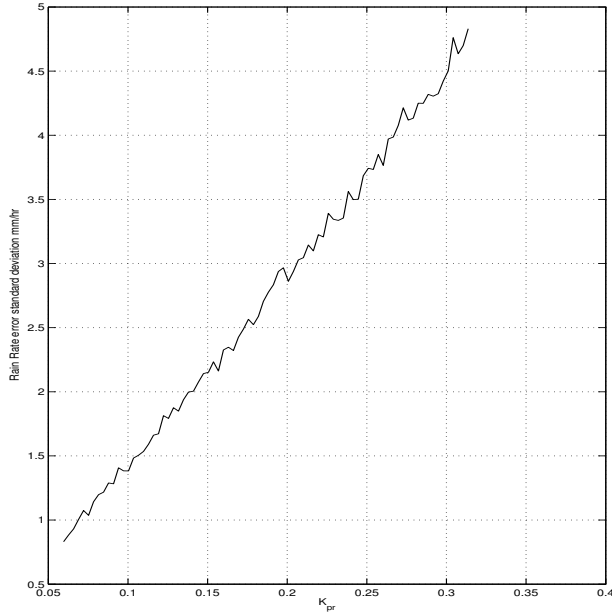
Figure 5.6: Simulation of the standard deviation of R_{error} vs K$_{pr}$. The standard deviation of the R estimates is 2.5 when K$_{\text{pr}}$ is approximately 0.18.

The SeaWinds communication K$_p$ for the noisy σ° measurements is given by

$$K_p = \sqrt{(\alpha_c - 1) + \frac{\beta_c}{\sigma^\circ} + \frac{\gamma_c}{\sigma^{\circ 2}}}, \tag{5.8}$$

where α_c, β_c, and γ_c are the parameters kp_alpha, kp_beta, and kp_gamma that are computed and stored in the SeaWinds L2A data product. The average K$_p$ for regime 1 data from all case studies is 0.15. Figure 5.6 suggests that if all non-communication noise were removed, the standard deviation of the SeaWinds rain estimate would be approximately 2.0 mm/hr, only 20% less than the current standard deviation.

From this simple comparison it is reasonable to conclude that, on the average, SeaWinds rain estimates are limited by the signal to noise ratio of the instrument. The noise from communications K$_p$ dominates, and the noise from exterior sources such as beamfilling, model error, and imperfect colocation, are only secondary.

Chapter 6

Conclusion

Large scale observation of ocean winds and rain is a critical tool for global climatology, weather prediction, and storm tracking. Microwave remote sensors, such as scatterometers, provide world-wide daily observations of ocean winds. However, the benefits of a scatterometer's observations are constrained by the accuracy of its measurements.

Although originally designed to measure near-surface wind vectors, spaceborne SeaWinds scatterometers are sensitive to rain. Simultaneous wind/rain retrieval enables SeaWinds to estimate wind vectors and vertically integrated rain rates for observed ocean areas. SeaWinds' rain rate estimates are useful because its broad coverage gives daily estimates for much of the Earth's ocean surface.

This thesis addresses the question of accuracy of instantaneous SeaWinds simultaneous wind/rain estimation in real events. Validation of the estimates is performed using ground-based NEXRAD weather radar. Comparison of the rain fields generated by the two sensors reveals that, on the average, simultaneous wind/rain retrieval estimates the correct rain field. Additionally, if thresholding is used, the algorithm yields an improved rain flag over previous algorithms.

In both wind and rain estimates we observe the same trend. Simultaneous wind/rain retrieval removes biases that are present in the conventional retrieval algorithms. On the average, the wind and rain estimated by the algorithm is correct. However, the variability of the estimates is quite large. SeaWinds rain estimates are accurate to within 2.5 mm/hr. Much of the noise that creates the high variability is intrinsic to the SeaWinds system and the rain model sensitivity.

6.1 Summary of Contributions

This thesis presents a look into SeaWinds-based simultaneous wind/rain retrieval in severe storm events. The contributions of the thesis may be summarized as follows.

- Rain information from simultaneous wind/rain retrieval and NEXRAD weather radar was collected and colocated into useful rain fields for several storm events.

- We determined that, in general, rain observations from both instruments are related in a linear fashion. The correlation coefficient of the storm events decreases with storm intensity and varies between 0.6 and 0.9. Additionally, we showed that the statistical distribution of rain rates from both instruments are nearly identical.

- We identified squaring off in the conventional L2B wind fields and showed that simultaneous wind/rain retrieval exhibits fewer squaring off effects.

- We analyzed wind/rain information from each regime as classified by simultaneous wind/rain retrieval. We determined that data from each regime behaved as predicted by Draper. Wind information from regime 1 and rain information in regime 3 are, in general, not observable.

- We developed a least squared error rain-only detection algorithm. This algorithm is applied to rain dominated (regime 1) WVCs. We showed that in low wind events, correlation is improved when rain-only retrieval is used in such areas.

- We identified and developed a simple model to estimate SeaWinds rain rate variability. We determined, using the model, that the standard deviation of rain estimates is 2.5 mm/hr.

- Through rain-only retrieval analysis we found the K_p necessary to cause the rain estimates to have a standard deviation of 2.5 mm/hr. We found this K_p to be close to the predicted communications K_p of $\sigma°$ of the SeaWinds instrument.

We thus found it reasonable to conclude that rain rate estimation error sources such as beamfilling and model error, are relatively small, and improvements in the error would most likely yield marginal improvements.

6.2   Future Research

The noise model presented in this thesis for simultaneous wind/rain retrieval may be overly simplified. It assumes only additive uncorrelated noise. In reality, several of the noise sources, such as beamfilling, may be correlated. Also, the noise in the retrieval algorithm may consist of an additive and multiplicative component. A more complex model may yield a more accurate study of noise effects on simultaneous wind/rain retrieval.

Another source of error that may be important in rain field comparison is colocation. Similar to the study by Draper in [6], this study compares observations that are colocated by ground footprint. The observations are not necessarily coincident at higher altitudes. This may result in error because each NEXRAD/SeaWinds observation may be observing separate rain cells at different altitudes. Improved comparison may be made by comparing the 3-D rain fields determined by each instrument.

SeaWinds WVCs are at a very low resolution for rain cell observation. Low resolution observations increase beamfilling error. A high resolution wind vector observation algorithm has been developed in [33]. A high resolution simltaneous wind/rain retrieval algorithm may be developed. High resolution NEXRAD rains may then compared with high resolution SeaWinds rains, reducing the beamfilling error and improving rain field comparison.

Appendix

Appendix A

Daily Antarctic Sea-Ice Edge Expansion and Contraction Detection with Binary Processing Applications

A.1 Introduction

The sea-ice edge extent of Antarctica is constantly changing. Freezing, melting, ocean currents, wind, and other factors all contribute to its variability. A knowledge of how the ice edge extent changes can help in understanding the impact Antarctic sea-ice has on global climatology and improve sea-ice mapping techniques.

Antarctic has an inter-annual ice range of about 16×10^6 km^2 [34]. The large variability, combined with the inhospitable conditions of the area and long periods of darkness, make "in situ" Antarctic ice edge detection difficult. For this reason, it is desirable to use remote sensing to provide such information.

Since its mission began Julian Day (JD) 200, 1999, the QuikSCAT scatterometer aboard the SeaWinds satellite has been a useful sea-ice detection sensor. Seawinds detects sea ice by transmitting a ku-band radar at the Earth's surface and measuring the radar cross section (RCS) of the reflected energy. The electromagnetic energy QuikSCAT transmits is unaffected by darkness or clouds and QuikSCAT scans the entire polar ice caps daily. The daily coverage makes QuikSCAT a good data source to determine polar sea-ice edge changes.

In order to determine the sea-ice edges from the RCSs gathered by QuikSCAT, the daily average RCS must be determined. This is done using the scatterometer image reconstruction (SIR) algorithm [35, 36]. From this algorithm a map of the average RCS measurements is created. This is called a "SIR" image. Figure A.1 displays a SIR image from JD 237, 2003.

In SIR images sea-ice can be distinguished from open ocean. This is due to the difference in the textures and values of the RCSs of sea-ice and open ocean. An ice-mask can be created by determining which parts of the image are land, sea-ice, and open ocean and creating an image reflecting the classifications. An example ice-mask is displayed in Fig. A.2. The black areas are classified ocean, the gray are sea-ice and the white areas are land.
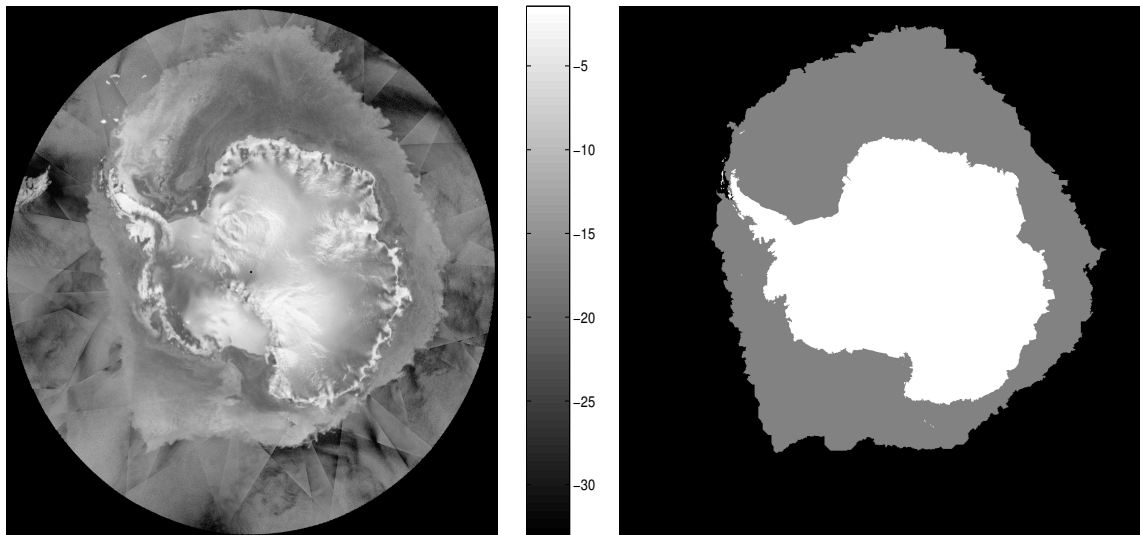
Figure A.1: SIR image from vertically polarized slice QuikSCAT data from JD 237, 2003. The backscatter shown is represented in dB.

Figure A.2: QuikSCAT ice-mask from the JD 237, 2003. Gray areas designate classified sea-ice, white areas designate land, and black designate classified open ocean.

To automatically create ice-masks Long [10] developed an adaption of the Remund-Long algorithm [37, 38] that uses an iterative maximum likelihood method on SIR image data. After sea-ice/ocean classifications are completed binary processing using region growing techniques is applied to remove spurious ice classifications and to restrict ice edge expansion and contraction [39]. Currently, daily ice edge expansion and contraction is limited to 200 km. It is desirable to determine if relaxing or tightening this restriction can yield more accurate ice-masks.

76

In this study only Antarctic sea-ice is examined. This is because the bulk Antarctic sea-ice edge movement occurs in northern and southern directions [40]. Arctic sea-ice edge movement is more complicated due to the geography of the land masses surrounding the Arctic Ocean. Such movement requires an approach that is more robust than that used in this study.

To determine the optimum constraint, daily contraction and dilation over several longitudes is examined and filtered in Section A.2. Section A.3 determines statistical from the gathered data. Section A.4 verifies the results of the daily ice-mask changes using data gathered by the Special Sensor Microwave/Imager (SSM/I). Section A.5 makes recommendations on how the results of this study may be applied to the Long algorithm.

A.2   Antarctic Ice Edge Movement along Longitudinal Lines

The Antarctic sea-ice edge changes are complex. It can dilate, contract, move zonally, or move to the north or south. This complexity means it can be difficult to determine what ice-edge movement is. To simplify the problem, in this appendix, ice edge movement is measured by changes in the maximum latitudinal sea-ice edge extent along selected longitudinal lines. This approximation is made because most ice movement occurs along longitudinal lines. In other words, although some zonal movement occurs, the advance and retreat of the sea-ice edge generally occurs in northern and southern directions.

The longitudinal lines that are studied in this appendix are in 20 degree increments from -175° to 165°. Fig. A.3 shows the longitudinal study lines as solid lines pointing radially outward over a polar map of the Antarctic continent.

To determine the latitudinal sea-ice edge extent movement, daily calculations of the sea-ice edge from JD 200, 1999 to JD 365, 2003 are made. This is done by first, converting all land in the trinary ice-mask to ice as shown in Fig. A.4. The result is a binary image where ice pixels are 1's value and open ocean pixels are 0's. The

77
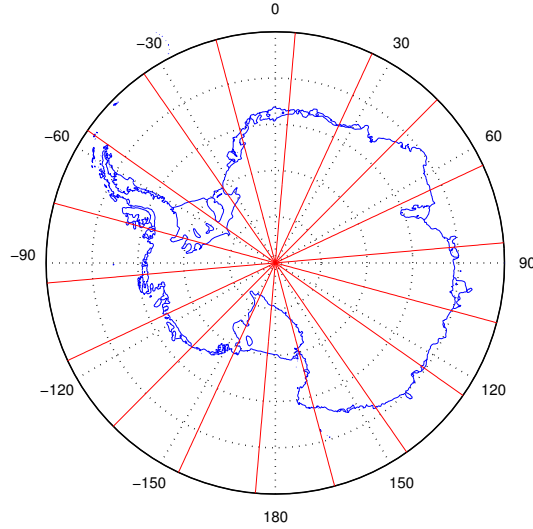
Figure A.3: Polar map of Antarctica. The solid lines pointing radially outward are the longitudinal lines used in this appendix.

lower ice edge is found by subtracting the image from a shifted version of itself using

$$a_{i,j} = \begin{cases} a_{i,j} - a_{i-1,j} & i > 1 \\ a_{i,j} & i = 1, \end{cases} \tag{A.1}$$

where the image consists of an $n \times m$ matrix, and $a_{i,j}$ is the value of the pixel on the jth column of the ith row. The shifted difference image is then converted to a binary image by setting all non-positive a values to 0. The result is an image where pixels on the lower boundary of the ice are 1's and the rest are 0. An example of the binary shifted image is displayed in Fig. A.4(c). This process is repeated using images that are shifted right, left, and up. An ice edge image is then created from the union of all four shifted difference images. The result is an image whose pixels are one on the ice edge are zero everywhere else as shown in Fig. A.4(d). The latitude and longitude of the center of each edge pixel is then determined. The latitudinal extent of the ice edge along a study longitude is then chosen to be the edge pixel with the greatest latitude whose longitude is less than 0.25° from the longitude of interest. The data from the latitudinal ice-extent is then used to make time graphs of the ice edge. Figure A.5 displays an ice edge extent plot for -135° longitude.

| (a) | (b) | (c) | (d) |
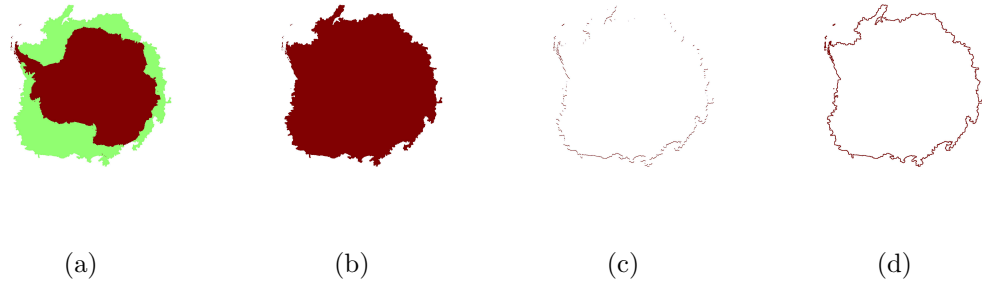
Figure A.4: Ice edge detection algorithm steps. The RL trinary mask image in (a) is converted to the binary image in (b) by setting all land pixels to ice pixels. (c) displays the detected ice-edge after the first shifting operation. (d) displays the detected ice-edge after all 4 shifting operations

The most noticeable aspect exhibited in Fig. A.5 is the large spikes that go to -74° latitude. A normalized histogram of the daily ice-edge change is displayed in Fig. A.6. This histogram exhibits a number of daily changes that exceed 2° latitude. Such spikes are errors that result from algorithm errors or periods of missed coverage. Such spikes corrupt the data. In order to filter out spikes and preserve the actual data a robust 3σ filter is employed. The filtered time graph and normalized histogram are displayed in Figs. A.7(a) and A.7(b).

It is desirable to estimate the probability distribution function (pdf) of the daily sea-ice edge changes. The normalized histogram from the unfiltered data displayed in Fig. A.6 has a probability distribution function (pdf) that is neither Gaussian nor double exponential. However, the post-filtering histogram shown in Fig. A.7(b) has a pdf that is very similar to a double exponential pdf. This pdf is a good approximation for the distributions of nearly all the study longitudes.

After the latitudinal ice changes are filtered and the statistical distribution of the ice changes is found, changes are converted to km by finding the arc length of the each daily change. The mean sea-ice edge extent is determined and the sea-ice edge is plotted as a distance from the mean sea-ice edge extent. For example Fig. A.8 displays the sea-ice edge distance from its mean in km for -135° longitude. These
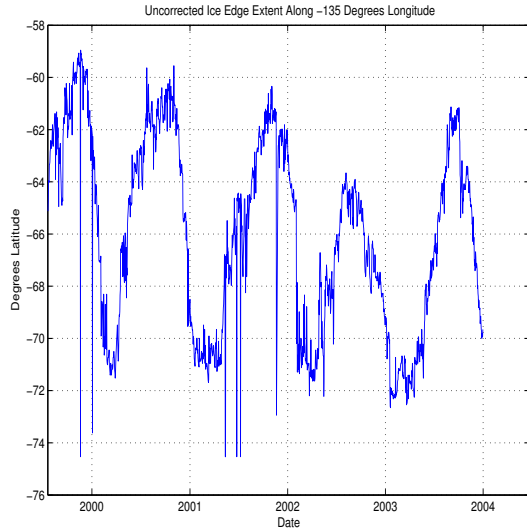
Figure A.5: Latitudinal sea-ice edge extent along -135° longitude prior to robust filtering.
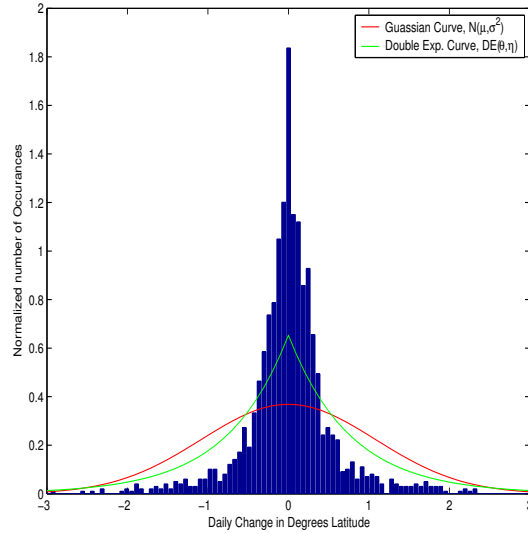
Figure A.6: Normalized 500 bin histogram of the daily latitudinal ice edge change along -135° longitude. Also shown are pdfs of Gaussian and double exponential distributions with the same variance and mean as the histogram.

histograms and plots provide data for analysis of the daily and yearly sea-ice edge extent changes.

A.3   Results

All of the produced plots and histograms provide information in determining the variability of the Antarctic sea-ice edge. From this information several statistical values for each of the longitudinal lines can be determined. The values noted are the mean daily change, daily change standard deviation, mean absolute daily change, mean contraction and dilation season daily changes, maximum absolute daily change, and average annual variability. All the previous statistical values for each of the longitudinal lines of interest are displayed in Table A.1. The standard deviation, and absolute mean of the daily ice movement are calculated from the entire data range in order to find the amount the ice can be expected to change each day.
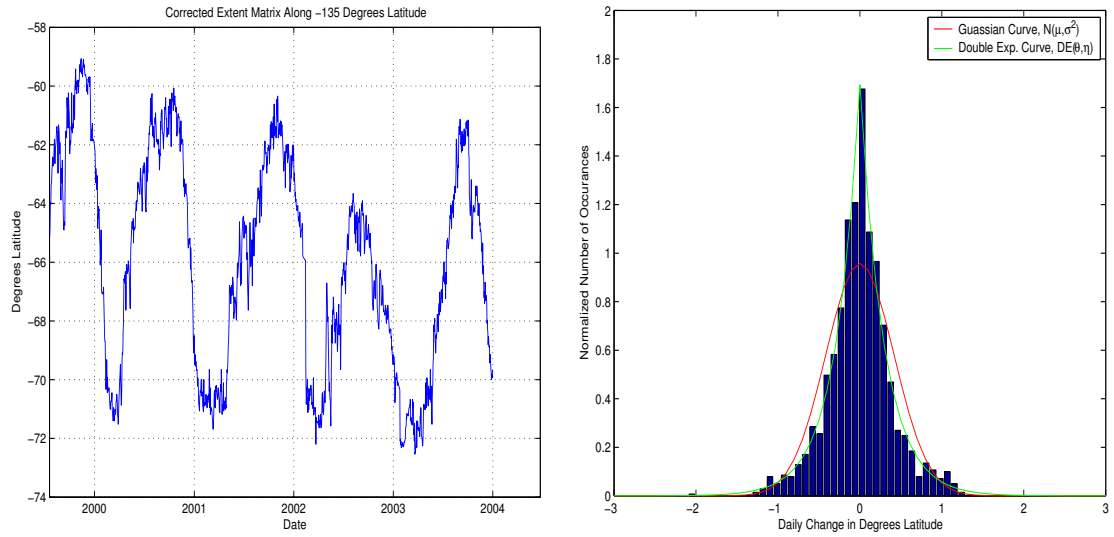
(a) Latitudinal sea-ice edge extent along -135° longitude after robust filtering.

(b) Normalized histogram of and Gaussian pdf of the corrected daily latitudinal ice edge change along -135° longitude with Gaussian and double exponential pdfs.

Figure A.7: Extent plot and histogram of ice edge extent along 135° longitude.

To study if the sea-ice contracts faster than it expands during the freeze and melt season, contraction and dilation seasons are defined. The seasons are determined by examining the corrected latitudinal sea-ice extent plots and estimating the seasons. From these observations, and the observations in [34] the dilation seasons are chosen to be JD 300 of a given year to JD 50 of the following year and JD 100 - JD 200 of any given year respectively. The mean dilation and contraction season sea-ice edge changes are then determined.

In order to improve sea-ice-edge movement algorithms, it is desirable to determine the maximum the sea-ice edge can dilate or contract in a single day. The maximum absolute daily change can be affected by zonal ice movement instead of ice-edge dilation or contraction. For this reason the maximum change is limited by the iterative σ filter, and human analysis. The human judgment is done by making an animation of the ice-edge about the day of maximum change and observing if
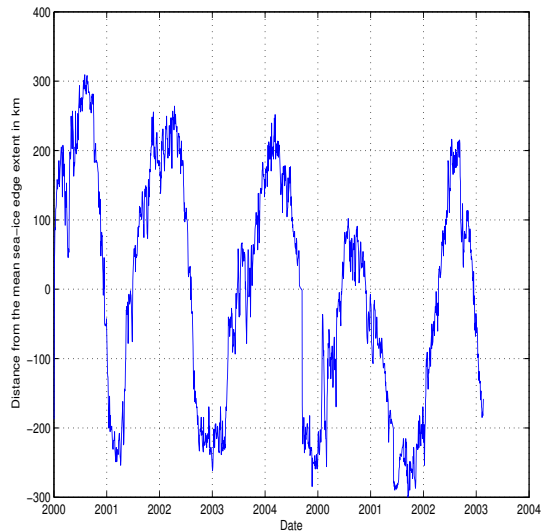
Figure A.8: Sea-ice edge extent distance from the mean sea-ice edge extent along -135° longitude.

the change is caused by contraction, dilation, or lateral ice-movement. The changes caused by lateral ice-movement are discarded and the maximum change cause by contraction or dilation is chosen as the maximum absolute daily change.

Also, sea-ice edge time-series data can also be used to find the average annual variability. The average annual variability is defined as the average minimum sea-ice edge extent subtracted from the maximum sea-ice edge extent in a given year over the years of interest. The average annual variability is also displayed in Table A.1.

A.4   SSM/I Verification

In order to explore the accuracy of the results of Table A.1 the experiments performed using QuikSCAT data are repeated using data from SSM/I instrument F-13. F-13 is a radiometer that also provides daily coverage of Antarctica. It measures microwave emissions from the Earth's surface and calculates the surface brightness temperature (T_b) over 7 microwave channels. The brightness temperature of three of the channels is then used by the NASA Team algorithm [41] to detect sea-ice and create ice-masks similar to those created by the Remund algorithm. The daily ice-edges

Table A.1: Table of measured sea-ice extent values for each of the study longitudes.
All units are in km.

Table of Measurements for each Selected Longitudinal Line (km)						
Long-itudinal Line	Daily Change Std.	Mean Absolute Daily Change	Mean Con-traction Season Daily Change	Mean Dila-tion Season Daily Change	Max. Ab-solute Daily Change ($\leq 5\sigma$)	Average Annual Variability
-175°	63.7	33.3	-9.46	4.90	170	1436
-155°	44.6	31.1	-8.16	8.19	126	1271
-135°	44.3	31.4	-8.11	6.65	140	1234
-115°	42.7	29.5	-4.95	3.55	108	914
-95°	35.9	25.8	-3.60	2.37	87	726
-75°	34.9	24.7	-3.40	3.90	94	782
-55°	8.3	1.99	0.00	0.54	25	138
-35°	64.9	40.7	-9.57	7.31	159	1476
-15°	66.0	37.0	-11.50	9.99	237	1698
5°	67.2	38.4	-13.2	11.60	235	1813
25°	57.4	35.1	-11.7	8.55	205	1719
45°	39.9	26.4	-7.40	5.21	131	1086
65°	41.4	27.0	-7.61	4.56	143	1006
85°	54.5	36.7	-4.91	6.30	179	971
105°	36.4	24.4	-3.65	3.26	117	716
125°	30.0	19.3	-2.89	1.05	94	540
145°	35.5	22.1	-2.07	1.71	108	587
165°	32.9	21.1	-4.36	4.40	94	708

are determined for each of the study longitudes and daily changes are determined. The results of both experiments are compared, and the correlation of the two sets is noted.

Before a comparison of results is performed, the differences between QuikSCAT and SSM/I data sets are considered. One major difference between the Remund and the NASA team algorithms is that the NASA team algorithm estimates sea-ice concentration while the Long algorithm uses an iterative ML method to classify points as either sea ice or open ocean. In order to make the NASA team algorithm comparable with the Long algorithm, a threshold of 30% is set for the NASA team

results. This has been shown to be the most accurate threshold to map the Long ice-edge to the NASA team ice-edge [38]. Points with ice-concentration greater than 30% are classified as sea-ice, while points with less than 30% concentration are classified as open ocean. This estimation is roughly equivalent to the Long algorithm estimation [10], but it is not exact.
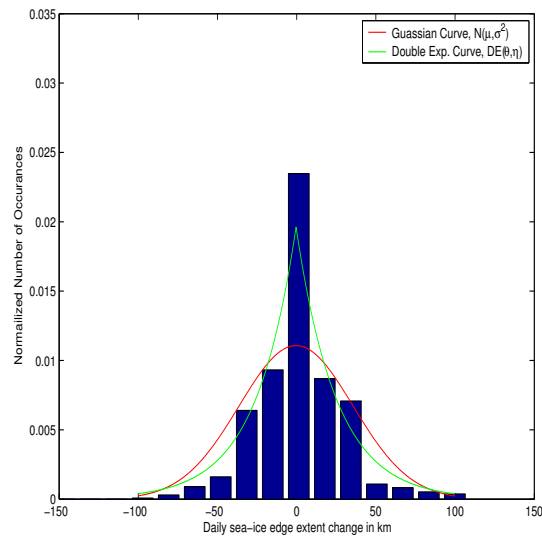
Figure A.9: Corrected normalized histogram of daily sea-ice extent changes using SSM/I data. The lower resolution of the data reduces the number of possible detected sea-ice changes. The pdf of the data is somewhat similar to a double exponential.

Another difference in the data is that the resolution of the two instruments is different. SSM/I images have a pixel size of 25 km with an effective resolution that varies from 70 to 15 km, while Seawind's pixel size is 4.225 km [36] with effective resolution between 5 and 10 km [42, 43]. Seawind's higher resolution should allow it to be a more accurate detector of small scale ice edge movements.

Figure A.10 displays the corrected ice-extent distance from the mean in km for both SSM/I and QuikSCAT data for -135° longitude. It also displays the difference in latitude between the two plots. The two plots are similar. The shapes and distances

from the mean are generally equivalent. The main difference in the plots can be seen in comparing their textures. Figure A.10(b) is rougher and has more small-scale variations while Fig. A.10(a) is comparatively smooth. The texture difference is likely caused by the resolution differences of the instruments. QuikSCAT superior resolution allows it to detect small scale movements and produce finer scale plots.

On average, for all latitudes, QuikSCAT projects ice-edge to be 5-20 km further north than SSM/I. This bias is most likely due to errors in the threshold approximation. The difference plot on Fig. A.10 shows that the largest differences occur during periods of rapid growth or contraction. It appears that SSM/I detects both ice contraction and dilation earlier than QuikSCAT.

Table A.2 displays statistics for each study longitude using SSM/I data, the percent difference of the SSM/I statistics from the QuikSCAT statistics on table A.1, and the correlation coefficient of the QuikSCAT and SSM/I latitudinal extents. Most of the mean daily changes and average annual variabilities for QuikSCAT and SSM/I differ by less than 10%. The similarities of the mean daily change and average annual variability suggest that the smallest and largest longitudinal extents for each year and the extents at the start and end of the study period are equivalent for both data sets. All of the correlation coefficients are greater than 8.9, and most are greater than 9.4. This suggests that for each longitudinal study line, each day's SSM/I latitudinal extent differs from the QuikSCAT latitudinal extent by a nearly constant coefficient. Since the start and end points and the maximum and minimum points for each year are nearly equal it can be deduced that the difference between the detected extents by both sensors for each day is small in most cases. This means that, on a large scale, the ice edges detected by QuikSCAT and SSM/I are similar.

For each longitudinal line of interest the SSM/I daily change standard deviation, mean absolute daily change, and maximum daily change are 19% to 55% smaller than their QuikSCAT counterparts. One major reason for this is the lower resolution of SSM/I. This lower resolution causes many of the smaller daily changes to be undetected. Figure A.9 shows that, for -135°, SSM/I data detected no ice edge change for nearly 1/3 of all study days. On the other hand, the QuikSCAT histogram in

Fig. A.6 found no ice edge change on only 1/16 of the study days. This may be due to the pixel sized quantization, which is the result of the sensor's resolutions. The larger amount of days with no estimated change lowers the SSM/I standard deviation and mean absolute daily change. The lower standard deviation causes the iterative σ filter to allow fewer large changes, which may cause the maximum daily changes to also be smaller.

SSM/I ice edges detected using the NASA bootstrap algorithm with a 30% ice content are, on the large scale, consistent with those detected by QuikSCAT. Both detected ice edges are highly correlated with similar mean yearly and daily movements. However, the resolution differences of the SSM/I and QuikSCAT lead to significant differences in the detection of small scale changes. The average sea-ice edge change detected by both sensors is smaller than the resolution of SSM/I. The lower resolution causes SSM/I to miss many small scale changes, which leads to lower statistical values than those detected by the QuikSCAT sensor.

A.5 Binary Processing Applications

The binary processing algorithm in Long and Remund-Long ice-masking processing is described in detail in [9, 39, 44]. To summarize, binary processing is used to remove ice mis-classification errors. These errors are removed by a sequence of morphological image processing algorithms. The main algorithms employed used are erosion and dilation as described in [39, 45, 46]. The ice and ocean are sequentially dilated from areas that are known to be ice and ocean respectively. These dilations, termed region growing, remove polynyas and areas of sea-ice that are not adjacent to land.

After region growing, constraints are placed on the daily ice edge change to reduce large errors seen in the forms of "fingers" and "dents". This is done by iterating the dilation algorithm on the previous days mask until the desired dilation is achieved. Since each dilation expands the mask by 1 pixel the dilation distance is approximated by multiplying the pixel resolution by the number of iterations. The dilated mask is then subtracted from the current mask and a binary difference

Table A.2: Table of measured sea-ice extent statistical values for each of the study longitudes using SSM/I data. The parenthesis contain the percent difference between the corresponding QuikSCAT value and the SSM/I value for each statistic. Units are in km.

| Table of Measurements for each Selected Longitudinal Line (km) for SSM/I data. | | | | | | | |
| ()'s Contain the % Difference from QuikSCAT data. | | | | | | | |
Long-itudinal Line	Daily Change Std.	Mean Absolute Daily Change	Mean Contraction Season Daily Change	Mean Dilation Season Daily Change	Max. Absolute Daily Change ($\leq 5\sigma$)	Average Annual Variability	Corr. Coeff-icient
-175°	48.3 (-77)	19.9 (-40)	-9.84 (3.94)	5.04 (2.85)	124 (-27)	1473 (2.57)	0.964
-155°	31 (17)	20.3 (-35)	-8.7 (6.64)	8.29 (1.22)	87 (-31)	1285 (1.11)	0.984
-135°	36 (-5)	20 (-36)	-8.42 (3.83)	6.76 (1.61)	99 (-30)	1188 (-3.72)	0.992
-115°	29.3 (-6)	18.2 (-38)	-5.37 (8.43)	3.79 (6.73)	71 (-34)	914 (-0.0566)	0.957
-95°	26.5 (139)	16.4 (-36)	-3.94 (9.32)	3.21 (35.4)	76 (-13)	684 (-5.76)	0.973
-75°	25.1 (18)	16.1 (-35)	-3.38 (-0.728)	4.85 (24.3)	69 (-27)	751 (-3.94)	0.98
-55°	5.18 (-100)	0.898 (-55)	0 (-100)	0.651 (21.4)	23 (-9)	120 (-12.8)	0.845
-35°	38.4 (-103)	17.3 (-58)	-9.81 (2.5)	8.07 (10.4)	74 (-54)	1337 (-9.41)	0.975
-15°	48.5 (-34)	18.3 (-50)	-12.7 (9.85)	10.2 (1.89)	147 (-38)	1665 (-1.93)	0.981
5°	50.6 (12)	20.6 (-46)	-13 (-1.73)	12 (2.95)	177 (-25)	1764 (-2.7)	0.989
25°	40.9 (28)	19.1 (-45)	-11.8 (1.11)	8.61 (0.647)	120 (-42)	1686 (-1.96)	0.99
45°	26 (12)	14.6 (-45)	-7.31 (-1.25)	5.33 (2.31)	83 (-37)	1063 (-2.13)	0.985
65°	28 (84)	14.9 (-45)	-7.58 (-0.308)	4.86 (6.5)	81 (-44)	961 (-4.45)	0.983
85°	30 (6)	17.2 (-53)	-4.73 (-3.68)	6.39 (1.44)	126 (-29)	915 (-5.86)	0.973
105°	21.8 (4)	13.5 (-45)	-4.25 (16.4)	3.43 (5.28)	69 (-41)	622 (-13.2)	0.959
125°	19.1 (-67)	12.2 (-37)	-2.13 (-26.4)	2.02 (92.3)	57 (-39)	458 (-15.2)	0.896
145°	24.5 (-190)	13.6 (-38)	-2.8 (34.9)	2.44 (42.2)	71 (-34)	573 (-2.32)	0.94
165°	23.5 (40)	12.7 (-40)	-4.43 (1.57)	5.24 (18.9)	71 (-24)	701 (-0.928)	0.978

image is generated. Non-zero values, where the maximum growth constraint has been exceeded, are flagged as errors [44], and the current day's ice edge is mapped as a dilated version of the previous day's ice-edge [39]. The dilated version of the original edge is used to allow the algorithm to gradually recover from anomalies that are erroneously classified. Ice contraction is also constrained by eroding the previous day's image and performing a similar algorithm. ' Previously, the constraint on maximum sea-ice edge expansion and contraction has been set about 220km. The results of the study of this appendix now allow for constraints that exploit the physical properties of sea-ice expansion and dilation.

The results displayed in Tables A.1 and A.2 may be applied to the Long binary method with various levels of complexity. The simplest method is to adjust the maximum daily change constraint to the maximum of the maximum absolute daily changes exhibited by the ice masks of either image. Using that approach a new constraint of 237 km, which is only slightly larger than the current constraint would be used.

Setting a single ice change constraint does not exploit all the physical properties of the sea-ice. Sections 4 and 5 show that the amount of daily change is has a strong spatial dependence. To reflect this dependence, a constraint function is generated. Since this study reflects changes on only a few study lines cubic interpolation is used to create a piecewise polynomial constraint function that is dependent on the longitudinal location of the ice. Figure A.11 displays a plot of the piecewise constraint variable as a function of longitude. In this configuration the number of dilations applied to each pixel is dependent on its longitudinal location. Also, to exploit the time dependence of the ice edge movement, the spatially dependent constraint functions for ice dilation and contraction may be adjusted by the seasonal means shown in Table A.1.

When an area of the ice-edge is found to be in violation of the new constraint, the algorithm described by [39] is followed. The area exceeding the constrain is cut back the previous day's ice-edge. The cut area is then dilated or contracted to allow

anomaly recovery. In this way the spatial and seasonal characteristics of the ice may be exploited, allowing for more accurate filtering and ice-masks.

A.6 Conclusions

In this appendix, the average daily movement of the Antarctic sea-ice edge is analyzed. It is found that the pdf of such movement is approximately double-exponential. Tables A.1 and A.2 show that the largest mean daily sea-ice extent changes occur in the Weddell Sea (-35° to 45° longitude). Large changes also occur near the Ross Sea (-175° to -155°) and in East Antarctica (85°). Meanwhile, the ice on the Bellingshausen Sea (-125° to -75°) and the Indian Ocean (45° to 65°) tends to move slowly. This appendix also shows that, in general, Antarctic sea-ice contracts faster then it expands. For this reason the dilation season is longer than the contraction season.

Ice data from the NASA Team Algorithm using SSM/I data is used for comparison with the data from QuikSCAT. Both data sets have equivalent large scale estimations, but differ in the small scale. QuikSCAT data detects daily changes that are generally 30% larger than those detected by SSM/I. Many of the differences noted in Table A.2 are from the resolution difference of the two sensors and the filtering used in this study.

The results of this study may be applied to the binary processing step of the Long ice-masking algorithm. It is determined that the current 200km daily ice edge expansion or contraction constraint is too large, and the constraint can be reduced to 103km. This would reduce computation time and error sizes. A new method of constraining growth is also proposed. This method creates a constraint that is dependent on the date and location of the ice-edge. This constraint exploits the physical properties of the sea-ice to accurately flag algorithmic errors.
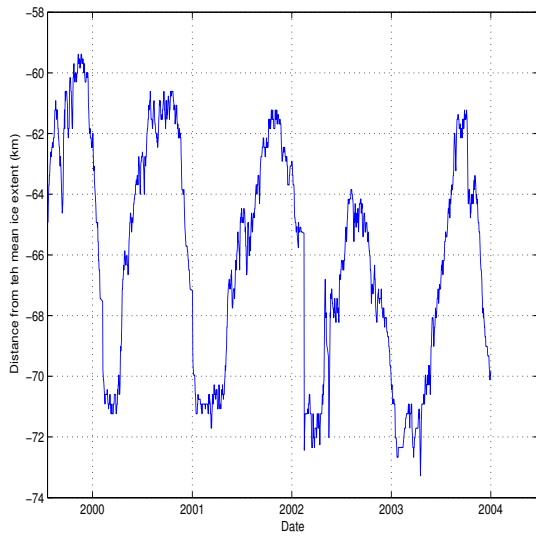
(a) SSM/I latitudinal distance from the mean (km)
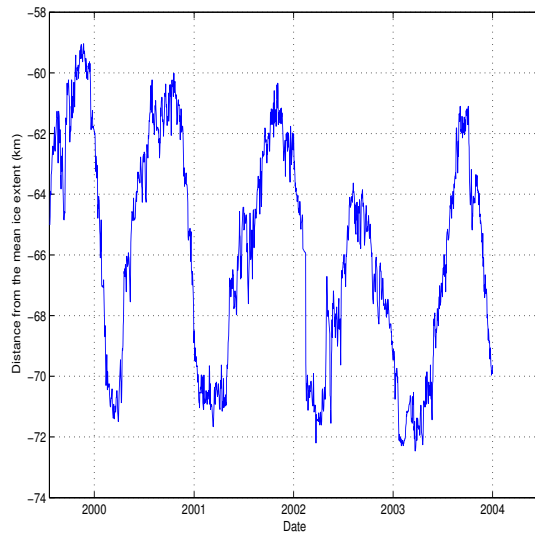
(b) QuikSCAT latitudinal distance from the mean (km)
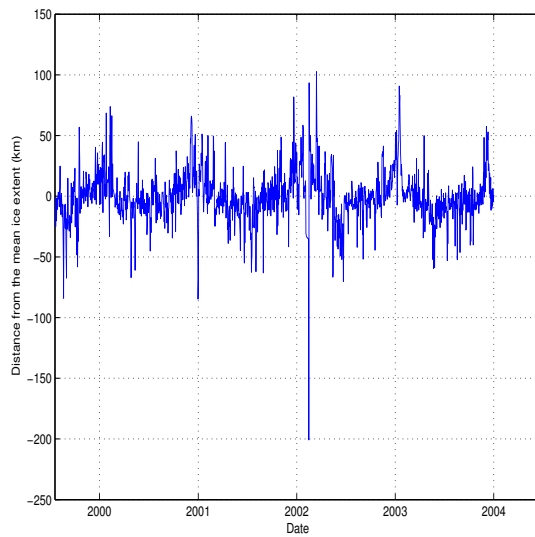
(c) SSM/I latitudinal extent subtracted from QuikSCAT latitudinal extent. One degree latitude is about 14 km in distance.

Figure A.10: Latitudinal distances from the mean (km) for both QuikSCAT and SSM/I measurements and the QuikSCAT and SSM/I latitudinal difference.
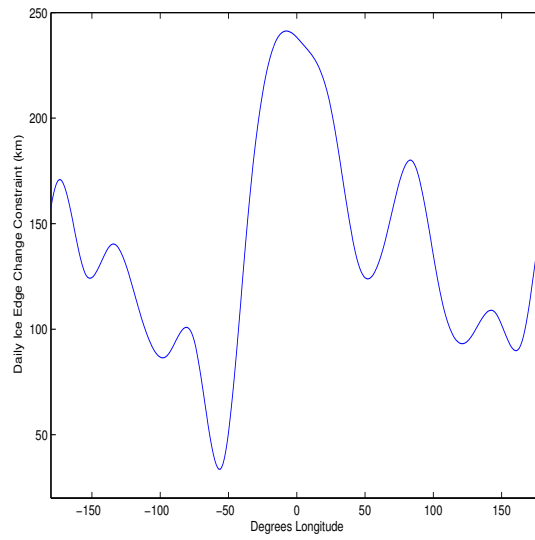
Figure A.11: Cubically interpolated plot of the constraint function over degrees longitude.

Appendix B

A Comparison of Ice-Masking Using QuikSCAT and Tandem Scatterometer Data

B.1 Introduction

Space-borne scatterometers provide a wealth of information about the Earth. These satellite instruments transmit pulses of electromagnetic energy toward the Earth's surface. Scatterometers then measure the radar cross section (RCS), or backscatter (σ^o), of the energy that is scattered off the Earth's surface and returns to the scatterometer. From the backscatter, a number of characteristics of the Earth's surface can be determined. One such characteristic is the extent of sea-ice around the Earth's poles. Scatterometers are especially useful in this application because their measurements are unaffected by atmospheric conditions and darkness.

It is desirable to compare the estimation of polar sea-ice using data from two different scatterometer data sets. The first set is data collected by the Seawinds instrument on the QuikSCAT satellite. This instrument is referred to as QuikSCAT. QuikSCAT's mission began in 1999 and continues today (Feb, 2005). QuikSCAT is in polar orbit and provides complete daily coverage of the Earth's poles. The second data source is the Seawinds scatterometer on ADEOS II. This scatterometer is referred to as Seawinds. Seawind's mission began April 10, 2003 and ended on October 24, 2003 due to a spacecraft power failure.

Seawinds and QuikSCAT are nearly identical instruments with the same operating frequency, incidence and azimuth angles, transmit powers, and orbits. In some applications, including the detection of polar sea-ice, their data can be treated as if they were one instrument collecting twice as much data. The combination of the

two data sets is referred to as tandem data. This appendix compares polar sea-ice detection using tandem and QuikSCAT data.

Each data subset is comprised of several subsets. This is because both the QuikSCAT and Seawinds scatterometers transmit alternating V and H polarized pulses at different incidence angles (46° and 54° respectively). The two different polarizations are transmitted in pencil beams sweeping in a circular pattern. This produces an elliptical antenna footprint. Measurements of the backscatter are termed egg data. To achieve higher resolution, the eggs can be resolved through signal processing into sub-footprints called slices [33]. Hence, each data set consists of V-pol egg, V-pol slice, H-pol egg, and H-pol slice subsets.

The process of finding polar sea-ice and creating a map of its extent is termed ice-masking. Sea-ice and open ocean can be differentiated because of the contrast in backscatter between sea-ice and open ocean. Sea-ice is generally much rougher than water, has greater conductivity, and reflects a much larger backscatter.

In order to translate the backscatter measurements of a data set to an image, the scatterometer image reconstruction (SIR) algorithm [35] is employed. The SIR algorithm processes egg data into images with a 4.225 km pixel size and slice data into images with a 2.225 km pixel size [36]. The SIR algorithm creates 4 images that are of interest. These images are:

- VV RCS σ_{ov} in dB;

- HH RCS σ_{oh} in dB;

- daily standard deviation per pixel for HH;

- daily standard deviation per pixel for VV;

Figure B.1 displays a σ_{ov} image derived from the SIR algorithm from slice data from the QuikSCAT instrument on August 25, 2003 over Antarctica. The light areas of the image correspond to areas of relatively high backscatter, and the dark areas correspond to areas of relatively low backscatter. In this image it is easy to see the ice-edge because of the differences in the backscatter textures of open ocean and sea-ice.

To automatically estimate the ice-edge and create an ice-mask Remund and Long developed the Remund-Long algorithm [37, 38]. This algorithm uses an iterative maximum likelihood (ML) approach on a 4-D histogram derived from both standard deviation measurements, σ_{oh} and a quasi-polarization ratio $(\sigma_{oh} - \sigma_{ov})$ to estimate the ice edge. Binary processing is then employed to constrain daily ice dilation or contraction and remove spurious ice classifications [39]. Later, Long developed an adaption of the Remund-Long algorithm termed the Long algorithm [10]. This is the processing algorithm used in this appendix. An ice-mask from September 30, 2003 produced by the Long algorithm is shown in Fig. B.2. The white areas correspond to land, the gray areas to sea-ice, and the black areas to open ocean.
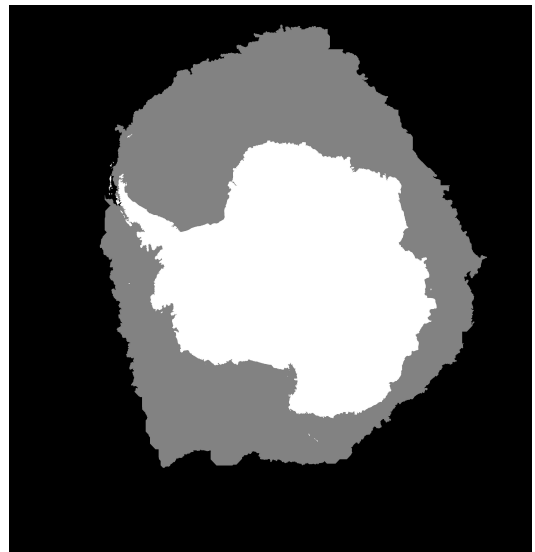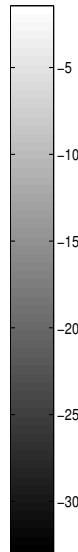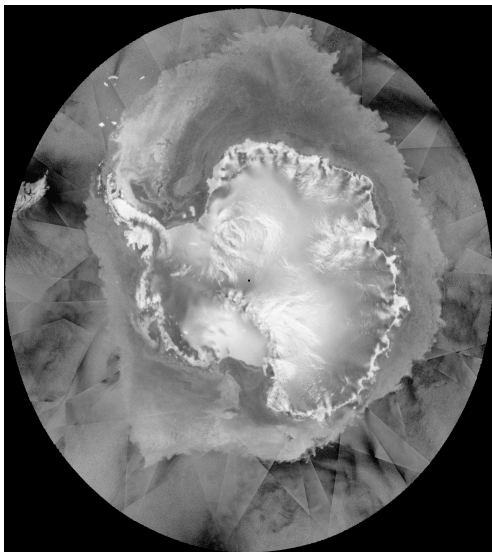
Figure B.1: SIR image from vertically polarized slice QuikSCAT data September 30, 2003. The backscatter is represented in dB.

Figure B.2: QuikSCAT ice-mask from the September 30, 2003. Gray areas show detected sea-ice, white areas show land, and black areas show open ocean.

At times it can be difficult to determine what is sea-ice and what is open ocean in a SIR image. For example, near-surface winds induce ocean surface capillary waves. These waves increase the backscatter and cause the ocean to appear more like ice.

95

Also, during times of melt, the water content of the sea-ice increases and pools of water may form on top of the sea-ice. This causes the ice to appear more like open ocean. These effects are sources of ice classification error. It is desirable to know if the tandem data set is more or less susceptible to error than the QuikSCAT set.

The tandem data set has a number of advantages over the QuikSCAT data set. The tandem set has twice as much data, so there is less missed coverage in a given time period. Also, the ADEOS II and Seawinds satellites are temporally spaced so one satellite passes over a given area several hours after the other. Hence, tandem data has a higher sample rate. This leads to higher spatial resolution while keeping the same temporal resolution (imaging period) as QuikSCAT. The accuracy of the σ^o estimates by the SIR algorithm increases with the number of samples provided by the data [38, 42]. The extra samples provided by the tandem data set yields more accurate SIR images. Also, for QuikSCAT at middle latitudes the standard deviation measurements have less significance because they are based on fewer measurements [47]. The extra samples provided by tandem data will give greater weight and accuracy to such measurements. For all the above reasons it is expected that the tandem SIR images will yield more accurate polar sea-ice detection than those from QuikSCAT data.

To determine with data set yields more accurate polar sea-ice detection, this appendix compares separate ice-masks made from QuikSCAT and tandem data. The same algorithm and settings are used from processing both sets. In section 2, the areal ice extents of ice-masks from each data set are compared. In section 3, the maximum latitudinal extent of Antarctic sea-ice estimated by the Long algorithm is found and discussed. In section 4 results from a few individual days are discussed. Section 5 concludes that the extra data provided by Seawinds increases the accuracy and quality of ice-masks developed using the Long algorithm.

B.2   Areal Extent Analysis

One way to evaluate ice masks created from different data sets is to analyze the ice-extent detected over a period of time for each set. Ice-masks using the Long

algorithm on QuikSCAT and tandem data are created for each day Seawinds data is available. The areal ice-extent is then found by finding the area of each ice pixel and summing them.

In order to achieve an accurate ice-extent measurement corrections must be made due to the map projection of the ice-masks. QuikSCAT ice-mask images are in a polar stereographic projection originating at 70° latitude. This type of projection is conformal but has areal distortion away from the origin [35]. To correct for this distortion, the area of each pixel is first set to the known area for a pixel at 70° latitude (4.950 km^2 for slice image pixels and 19.758 km^2 for egg image pixels [10]). The actual area is computed by dividing estimated area by the normalized areal distortion factor from [35]. (The distortion factor is normalized by the value of the areal distortion factor at 70° latitude.) The result of the division by the latitude-dependent normalized areal distortion factor is an accurate measurement of the area in km^2 covered by each pixel of the ice-mask image.

For verification purposes, daily ice data from the Special Microwave Measurement/Imager (SSM/I) instrument F-13, using the NASA Team Algorithm is included [41]. The SSM/I NASA Team dataset contains the percentage of the sea-ice concentration for each pixel in a given area. The resolution of SSM/I is 25 km, much less than the resolution of the egg and slice resolution of QuikSCAT. In order to approximate the ice-edge found by the iterative ML algorithm used by the Long algorithm, a threshold is used. The threshold that most closely corresponds to QuikSCAT ice-edge is 30% [38]. All pixels with ice concentration greater than 30% are classified as sea-ice, while pixels with concentration less than 30% are classified as open ocean. The corrected areas of the sea-ice pixels are summed and the areal ice-extent is determined.

Figures B.3, B.4, B.5, and B.6 show the areal extent of Antarctic and Arctic sea-ice detected by SSM/I, tandem, and QuikSCAT data for the duration of the tandem mission. Each figure displays the mean and variance of the estimated areal extent for all data sets. It can be seen that, for the most part, SSM/I, tandem and QuikSCAT data mirror each other with small differences. The SSM/I areal extents

Figure B.3: Areal ice extent vs. time for tandem and QuikSCAT egg data from Antarctica
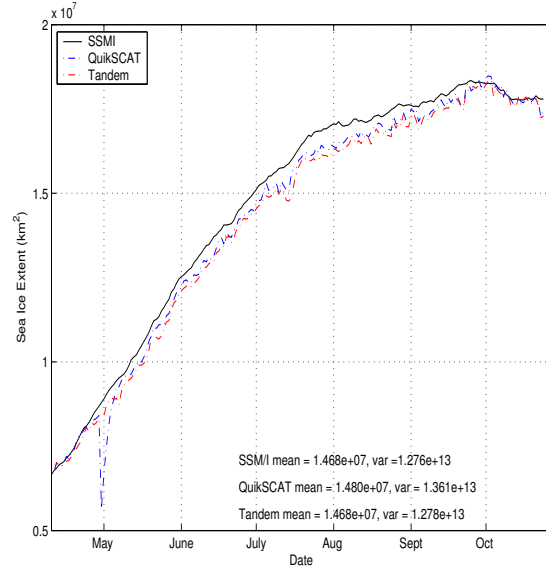
Figure B.4: Areal ice extent vs. time for tandem and QuikSCAT slice data from Antarctica

are generally greater than those of QuikSCAT and tandem. The main reason for this is land contamination. Land contamination occurs when pixels that contain both open ocean and land are classified as sea-ice. The tandem and QuikSCAT data do not suffer from land contamination because the land-mask used in the Long algorithm marks all pixels with land in them as all land. SSM/I does not do this [34]. The result is best seen in Figs. B.3 and B.4. When the ice area is small more land is bordered by open-ocean. This results in greater land contamination and differences between the areal extent detected by tandem and SSM/I are large. As the ice area increases, more land is surrounded by ice, and land contamination effects decrease. As a result, the differences between the ice-extents decrease. Differences may also be attributed to the fact that the 30% threshold is not an exact approximation, the inherent differences between active and passive sensors, and instrument resolution differences.

The largest differences between tandem and QuikSCAT are the Arctic slice extents between April 10 and May 10. SSM/I data shows that the tandem extent is correct. The errors are mostly likely caused by centroid drift in the Long iterative ML algorithm [39]. Each iteration in the ML algorithm used in the Long algorithm
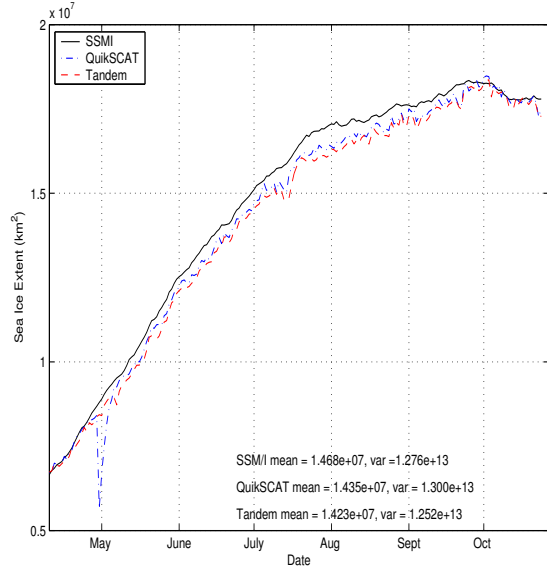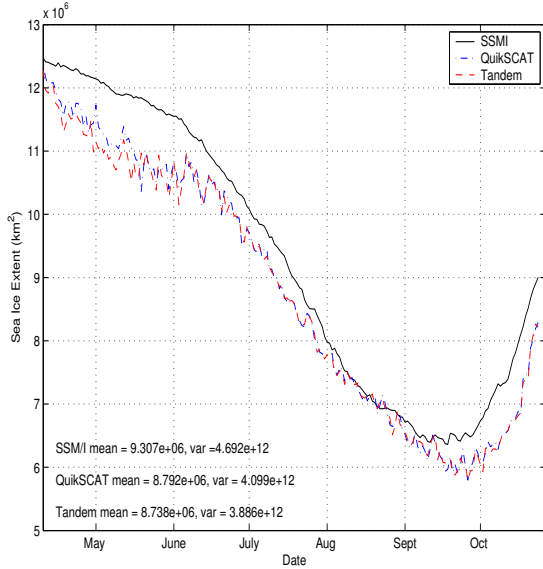
Figure B.5: Areal ice extent vs. time for tandem and QuikSCAT egg data from the Arctic
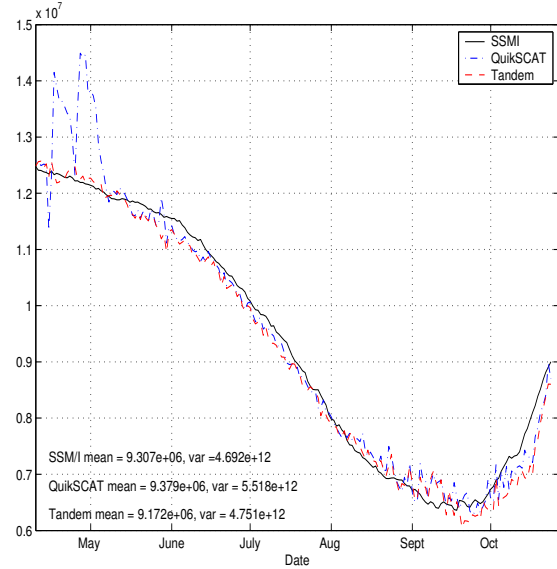
Figure B.6: Areal ice extent vs. time for tandem and QuikSCAT slice data from the Arctic

causes the centroids of the ice and ocean classification centroids to change. At times the centroids can drift so far that ice is classified as ocean and vice-versa. An example of this can be seen in Fig. B.7 which shows the ice-mask from April 16 from QuikSCAT Arctic slice data. The centroid drift in this figure causes the open ocean to be classified as sea-ice, and constraints from the previous day's data cause most of the sea-ice in the Arctic Ocean to remain classified as sea-ice. The result is that a large percentage of the ocean areas are classified as sea-ice causing the areal spike in Fig. B.6. The corresponding tandem ice-mask is shown in Fig. B.8. This ice-mask does not show drift effect errors.

In each data set the ice-masks made with QuikSCAT's data have a mean that is 0.6% larger than tandem's mean in the Antarctic and 0.8% to 2.5% larger than tandem's mean in the Arctic. The 2.5% difference in the Arctic slice data is, in the most part, caused by the centroid drift effects, while the 0.8% difference in the Arctic egg data is caused by data bias. All data subsets show a bias in which QuikSCAT ice-masks have more ice. This suggests that the addition of Seawinds data causes the algorithm to detect slightly less ice.

99
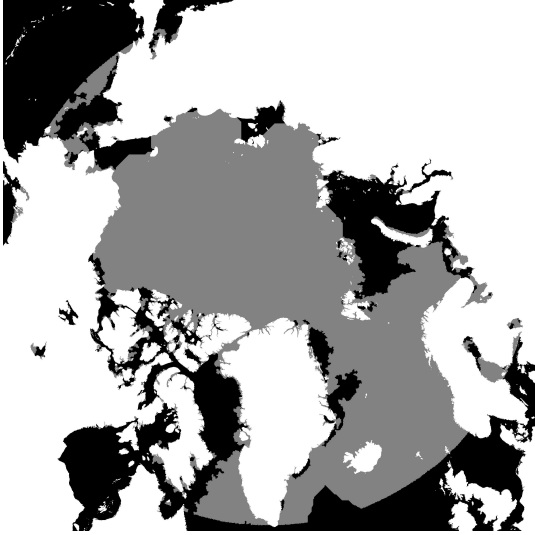
Figure B.7: QuikSCAT Arctic slice
ice-mask from April 16, 2003. Centroid
drift causes most of the open ocean to
be classified as sea-ice and some the
sea-ice to be classified as open ocean.

Figure B.8: Tandem Arctic slice
ice-mask from April 16, 2003. This
image does not have the
mis-classifications of Fig. B.7

The Antarctic areal extent plots for QuikSCAT and tandem are nearly identi-
cal. The largest deviation occurs on April 29. SSM/I data shows that the QuikSCAT
data is in error. This error occurs because on that day QuikSCAT was only able to
collect 2 orbits of data, instead of the usual 14. The data gap causes errors in the
QuikSCAT ice-masks because the algorithm determines that the sea-ice in missed
areas is ocean. After the day of missing data the algorithm takes several days to
dilate the ice back to the actual ice-edge. The Seawinds satellite collected a full data
set on April 29, 2003, and the tandem data is unaffected by the QuikSCAT gap.

The Arctic areal extent egg plots are highly correlated. In all cases the corre-
lation coefficient is greater than 0.98. The largest differences are caused by centroid
drift and missed coverage. In the days studied the tandem data did not experience
centroid drift or missed coverage. This is due to the advantages gained by the use of
two satellites.

B.3 Latitudinal Ice Extent Analysis

In this section the maximum latitudinal ice extent of the ice-masks is compared. The maximum latitudinal ice extent is the furthest extent of sea-ice away from the pole measured in degrees of latitude. In the Antarctic, this extent changes significantly as the ice contracts and dilates over a year. This measure is only effective on the Antarctic masks, because the Arctic masks generally have some sea-ice at the maximum latitudinal extent of the Arctic polar stereographic image all year.

At times, the ice-mask algorithm can incorrectly detect thin strips of ice protruding several degrees of latitude away from the main ice pack. Such strips can have small area, and may not be noticeable in section 2. However, such strips would be obvious in a study to latitudinal ice extent over time. Maximum latitudinal ice extent graphs for egg and slice data are created by dividing Antarctica into quadrants as shown on Fig. B.9. The maximum latitudinal extent of each quadrant is then found and plotted for each day of the tandem mission. Figures B.10 and B.11 display the maximum latitudinal extent for each quadrant for egg and slice data respectively.

The QuikSCAT and tandem plots in Figs. B.10 and B.11 have few discrepancies. However, there are a few important differences, some of which are investigated in this section. On May 22 Fig. B.10(a) exhibits a spike in the maximum latitudinal extent of nearly 2° that is not shown in the corresponding tandem plot. This increase does not have a large areal extent because there is not a significant corresponding areal increase in Fig. B.6. The QuikSCAT sir image with its corresponding ice-edge line from May 22 is shown on Fig. B.12. The difference can be seen in the top left of the image. It can also be seen from the SIR image that the difference is most likely an error in the QuikSCAT ice-mask. The error has a small area, but a relatively long latitudinal length. It is terminated by a straight line in the northernly direction. This is because the Long algorithm limits the ice-edge daily change to prevent errors from becoming very large. The zoomed tandem sir image with the ice-mask ice-edge line from the same day can be seen on Fig. B.13. The tandem ice-mask does not exhibit the error.
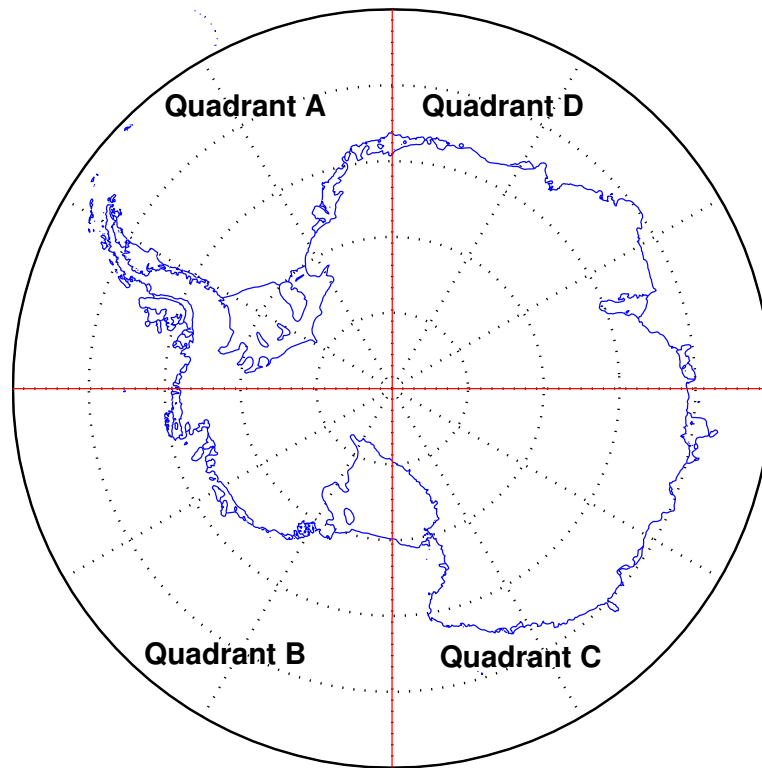
Figure B.9: The 4 Antarctic quadrants used in the latitudinal ice extent analysis.

The tandem and QuikSCAT ice-masks are different because the textures of the corresponding SIR images in the area of interest are different. The area of interest of the QuikSCAT SIR image has a texture very similar to that of sea-ice while that of the tandem SIR image does not. To better see the differences in the image a difference SIR image of this area is created. This is done by subtracting the tandem SIR image from the QuikSCAT SIR image. The zoomed result is shown on Fig. B.14. The large white spot in the area of the error shows where the QuikSCAT SIR image shows a higher backscatter with makes the open ocean to appear to be ice. In this case, the extra data of the tandem data set helps to yield a more accurate ice-mask.

Figure B.10(d) displays a spike in the Tandem data from July 7, 2003. To investigate the difference, QuikSCAT and tandem ice-edge outlines are plotted on the Quadrant C QuikSCAT SIR image. This plot is shown on Fig B.15. The line that stays closest to the pole corresponds to the tandem ice-edge the other is the
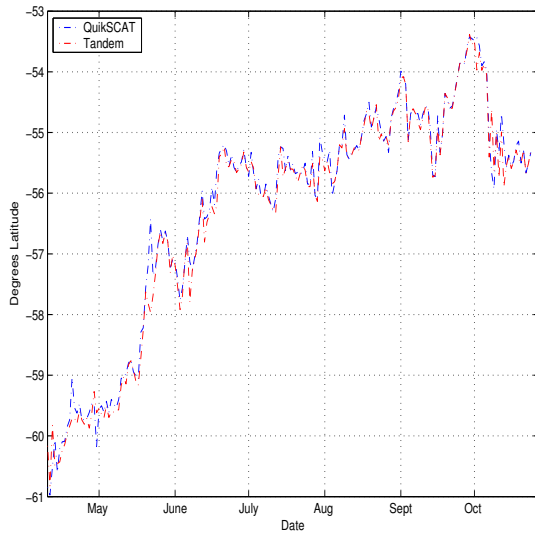
(a) Quadrant A
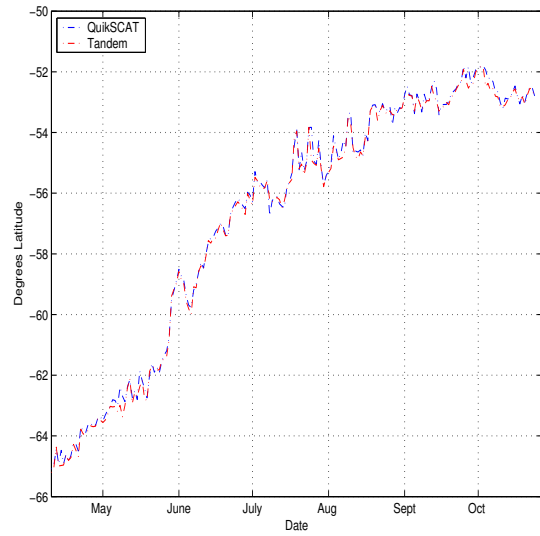
(b) Quadrant D
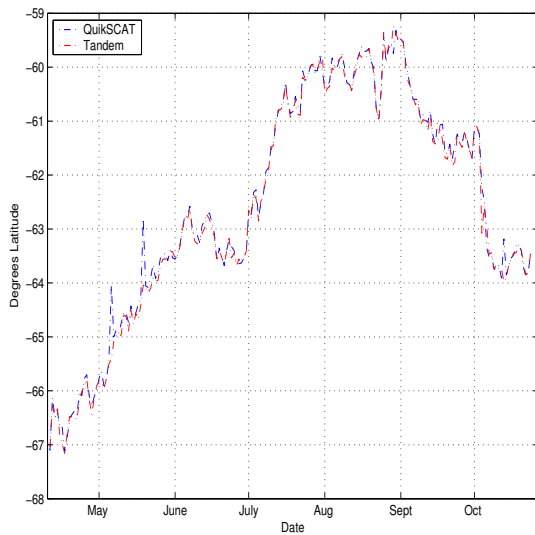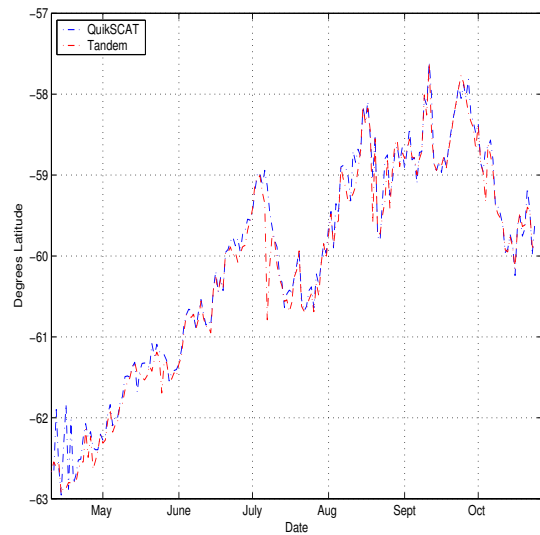
(c) Quadrant B

(d) Quadrant C

Figure B.10: Maxiumum latitudinal extent for each quadrant from Antarctic egg information.
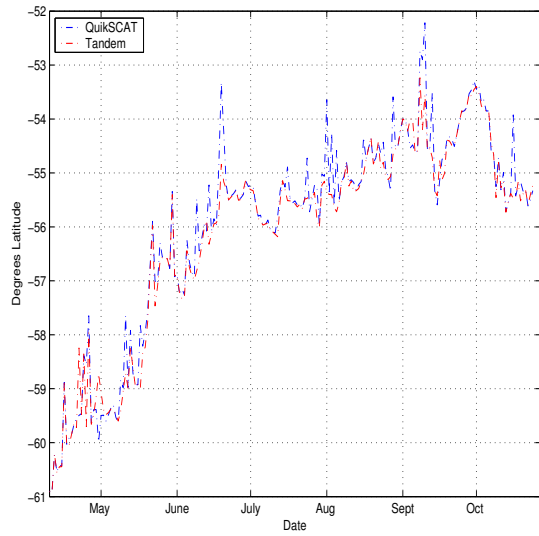
(a) Quadrant A
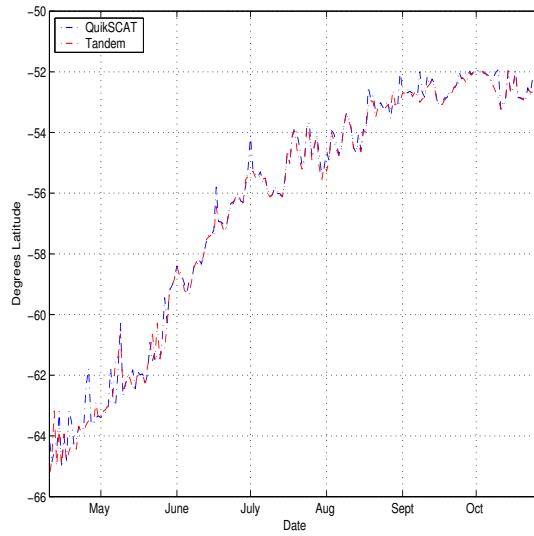
(b) Quadrant D
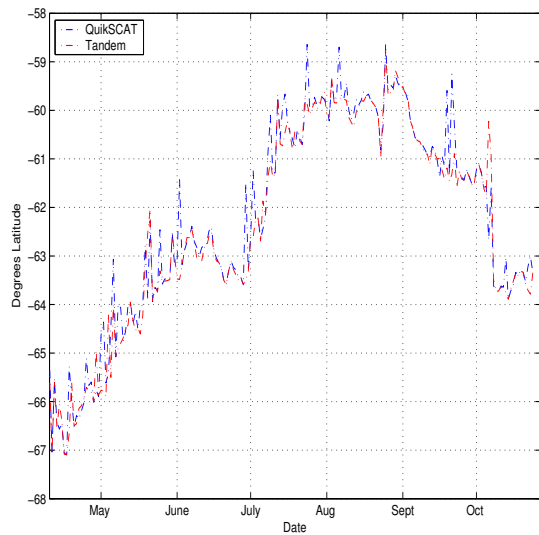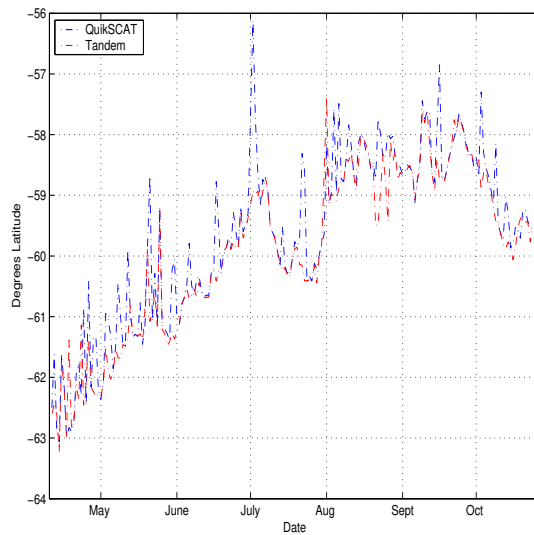
(c) Quadrant B

(d) Quadrant C

Figure B.11: Maxiumum latitudinal extent for each quadrant from Antarctic slice data.
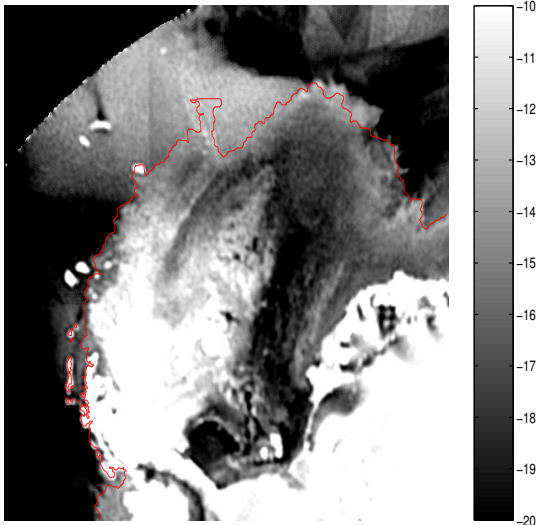
Figure B.12: Zoomed QuikSCAT VV Antarctic egg sir image from May 22, 2003. The image is enlarged to show only the ice just north of the Weddell Sea. A finger of classified ice 2° latitude in length protrudes off the top of the image because that area appears to have the same texture as sea-ice.
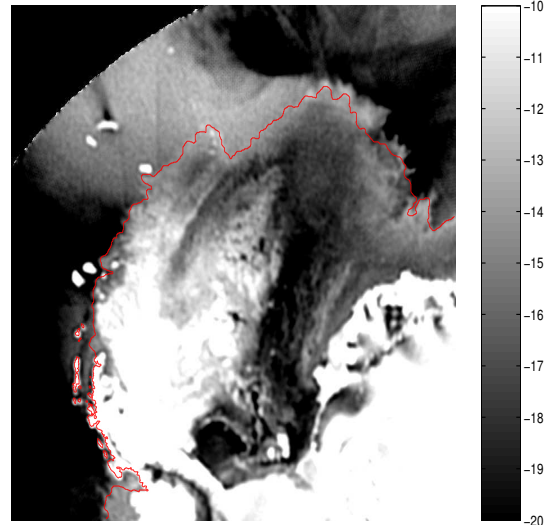
Figure B.13: Zoomed tandem VV Antarctic egg ice-mask from May 22, 2003. This image does not have the error of Fig. B.12 because the ocean just north of the ice-sheet does not have the same texture as the sea-ice.

QuikSCAT ice-edge. It can be seen that in this case the QuikSCAT ice-edge is more accurate than the tandem edge.

Through further studies it has been found that all differences in which one maximum latitudinal extent has a spike and the other does not, is from an error. This error is always in the ice-mask that has the spike. It can be seen from Figs. B.10 and B.11 that the QuikSCAT maximum latitudinal extents have many spikes, all of which are errors in the QuikSCAT data set.

The maximum latitudinal plots show that the ice-masks of the QuikSCAT and tandem data sets are very similar. There are some discrepancies in the egg plots and slice plots, but in most cases the extents are highly correlated. A further analysis of the differences in the plots reveal that when the maximum latitudinal ice-extent plots differ, the tandem ice-extent is usually more accurate.
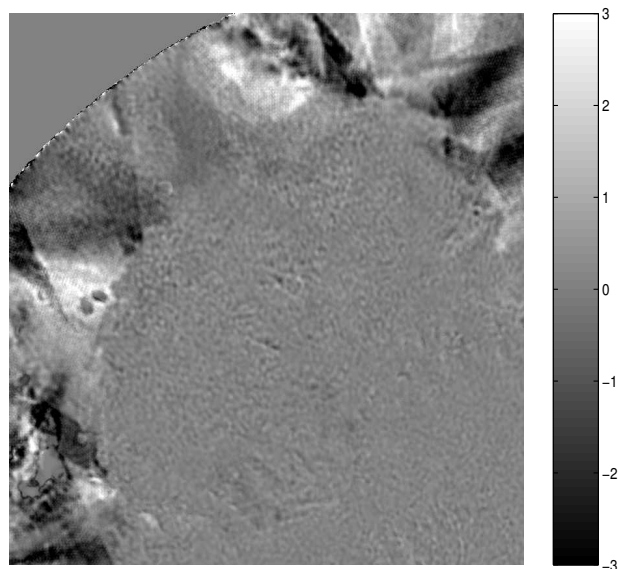
Figure B.14: Difference Image from SIR QuikSCAT and SIR tandem data (dB) for May 22, 2003. The white area in the same location as the error on Fig B.12 shows where the larger QuikSCAT backscatter makes the open ocean appear to be sea-ice which causes the error of Fig. B.12.

B.4 Individual Day Comparison

To further analyze tandem and QuikSCAT ice-masks, ice-masks from a few days chosen at random are examined with their respective SIR files. From these, human analysis is used to evaluate ice-mask accuracy.

Figures B.16 and B.17 display Antarctic slice data from June 19, 2003 over quadrant A. Neither ice-edge is completely accurate, but the QuikSCAT ice-edge is less accurate than the tandem. The QuikSCAT ice-edge extents far away from the sea-ice and has a straight line where the algorithm limits its extent. A difference image of the tandem SIR image subtracted from the QuikSCAT SIR image is shown in Fig. B.18. This image shows that the differences in the SIR images are very small in the area of interest. This means that the open ocean in the area of interest appears to be ice. The tandem ice edge estimate is more accurate, than the QuikSCAT estimate. This is due to previous tandem ice-masks that are more accurate than their tandem counterparts.
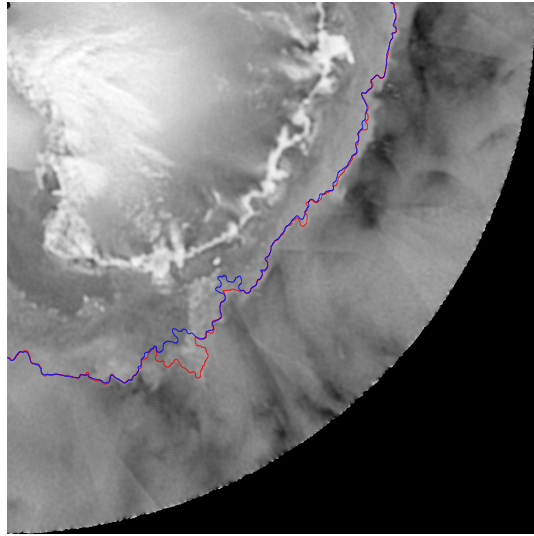
Figure B.15: Tandem and QuikSCAT ice-edges plotted on the QuikSCAT egg VV SIR image of quadrant C. The innermost line is the tandem ice-edge, while the outermost is the QuikSCAT ice-edge. In this case the QuikSCAT ice-edge is more accurate.

Figures B.19 and B.20 show QuikSCAT and tandem ice-masks for October 14, 2003 over the Davis Strait between Greenland and Baffin Island, Canada. The QuikSCAT ice-mask detects a large tongue of ice extending from Baffin Island into the Labrador Sea. The tandem ice-mask does not detect this tongue. The probablilty of such ice existing on October 19 is highly unlikely [34]. The shape of the ice is also unlikely, because the Northern and Southern ice-edges of the tongue are straight lines. To see why the tongue is exhibited by QuikSCAT data and not by tandem data a difference image is shown in Fig. B.21. In the difference image it can be seen that southern edge of the ice follows a line of large differences (3 dB). Hence, it can be deduced that the extra data from the tandem set makes the algorithm determine that there is no ice in the area. Once again, the tandem data creates a more accurate ice-mask.

In most tested days the tandem and QuikSCAT ice-masks are very similar. This section highlights days in which the largest differences are found. On such days, the tandem ice-masks are superior indicators of ice in an area. They more closely
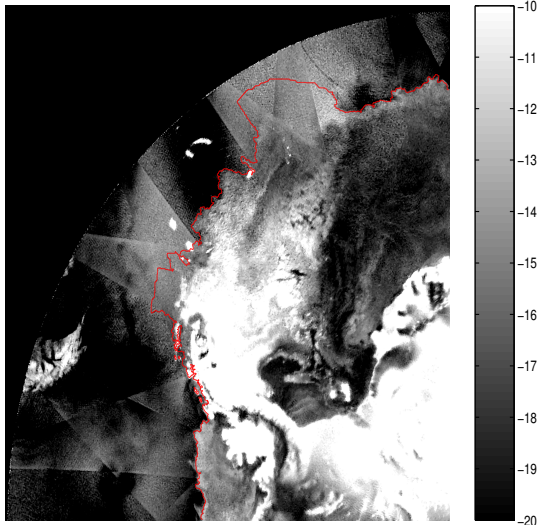
Figure B.16: QuikSCAT VV slice SIR image from June 19, 2003 quadrant A, Antarctica. The overlying line shows the predicted sea-ice edge. This line shows that the predicted edge extends far from the actual edge.
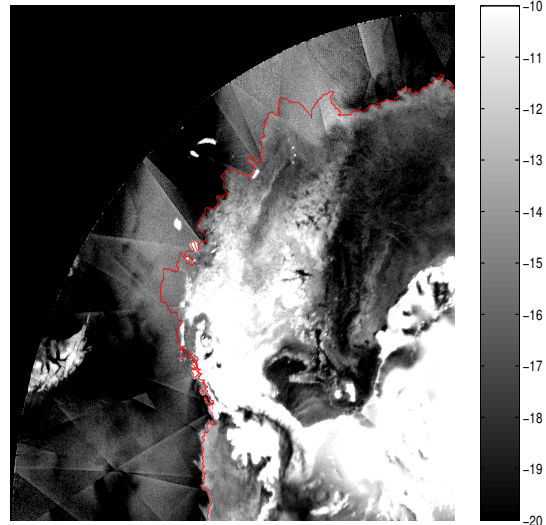
Figure B.17: Tandem VV slice SIR image from June 19, 2003 quadrant A, Antarctica. The overlying line shows the predicted sea-ice edge. This edge, although still inaccurate, is more accurate than the edge of Fig. B.16

follow the ice seen in the corresponding SIR images. On each the highlighted days the tandem ice-mask exhibits a more realistic ice-edge that appears to be more consistent with the SIR image than the QuikSCAT ice-mask.

B.5   Conclusions

On average, ice-masks from QuikSCAT data have an areal ice extent that is 0.6%-2.5% greater than the masks from tandem data. Additionally, QuikSCAT data alone produces more masks with long "finger" errors than tandem. The improvements exhibited in the tandem ice-masks are likely due to a combination of better standard deviation and σ^o estimates available in the tandem data set.

In most cases daily ice-masks from both data sets exhibit few significant differences. Nevertheless, on days of missed data, days of storms, melting, or data that causes centroid drift in the Long algorithm, the additional data yield more accurate ice-masks. Despite the fact that the tandem data is superior to QuikSCAT data,
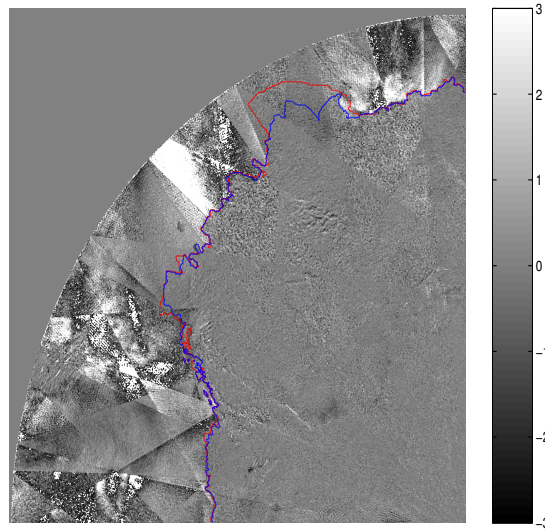
Figure B.18: Difference SIR slice image from June 19, 2003 from quadrant A. The lines show both the tandem (blue) and QuikSCAT (red) ice-edges.

Figure B.19: QuikSCAT slice VV SIR image from September 30, 2003 over the Davis Strait. A large error can be seen extending from Baffin Island into the Labrador Sea. The southern edge of this error borders a QuikSCAT swath edge.

Figure B.20: Tandem slice SIR VV image from September 30, 2003 over the Davis Strait. This image does not have the error of Fig B.19.
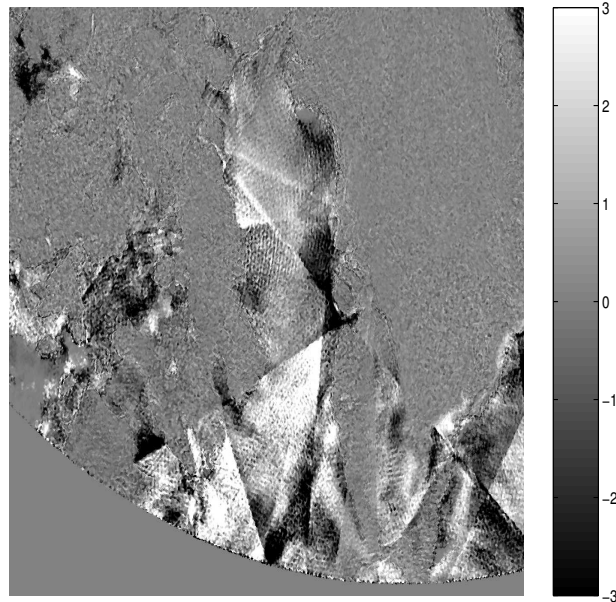
Figure B.21: Difference SIR slice image from September 30, 2003 over the Davis Strait. The largest differences in the SIR images is along the southern edge of the error in Fig B.19.

QuikSCAT data is still quite useful. This analysis has chosen images which highlight the main differences. In most cases QuikSCAT's ice-masks can are nearly as accurate as tandem's, and in some rare cases can be more accurate.

The accuracy of tandem ice-masks suggests that QuikSCAT ice-masks could be improved if two days of SIR data were used to create ice-masks. In that way, the QuikSCAT ice-masks would be made from a data set with as much data as tandem ice-masks. This extra data would improve the spacial resolution, supply more middle latitude measurements, but decreases the time resolution of the ice-masks. It would insert a low pass temporal filter in the algorithm and possibly cause temporal smearing of the image in periods of rapid ice change.

Even though tandem data is only available for a short period of time, it is quite useful. Tandem data can be used to get higher resolution ice-masks for the time it is available. The data set can be used to calibrate the Remund-Long algorithm for the remaining QuikSCAT instrument. Also, tandem data can be used to validate

ice-masks made from multiple days of QuikSCAT mission. The tandem accuracy can be used as a benchmark for future ice-mask algorithms.

Appendix C

Comparison of the Long and Remund Methods of Ice-masking

C.1   Introduction

This appendix compares and analyzes results from the Long ice-mask algorithm (developed by Long) [10] and the Remund-Long (RL) algorithm (developed by Remund and Long) [37]. Both algorithms employ an iterative maximum likelihood (ML) algorithm to classify pixels on as either sea-ice or open ocean. They also use binary processing to detect the ice-edge, and filter spurious classifications, and constrain ice changes. The Long method contains much of the code and algorithms of the Remund method with several changes and updates. For example, the Long binary algorithm weights coastal areas so that regions closer to land more likely to be classified as sea-ice. Also, the Long ML algorithm runs a variable number of ML iterations that is dependent on the season the data is collected, while the RL always runs three iterations.

Both algorithms perform ice-masking by first processing the data gathered by the scatterometer using the Scatterometer Image Reconstruction (SIR) algorithm [35] into an image. This image contains the one day average of the radar cross section (σ^o) for each pixel. Measurements of σ^o are combined with the variance of σ^o to create a data ensemble. This ensemble is used by the iterative ML method to classify a pixel is sea-ice or open ocean. Pixels that are classified as sea-ice are assigned a "1" value while ocean pixels are assigned a "0" value. A land mask adapted from the Central Intelligence Agency (CIA) World Data Set II is then applied to the image, and all pixels corresponding to a piece of land are assigned a "2" value. The resulting trinary-valued image is called a .corr image. An example .corr image of Antarctica

can be seen on Fig. C.1. The black areas are areas classified as ocean, the gray areas correspond to classified sea-ice, and the white areas of the image are land.
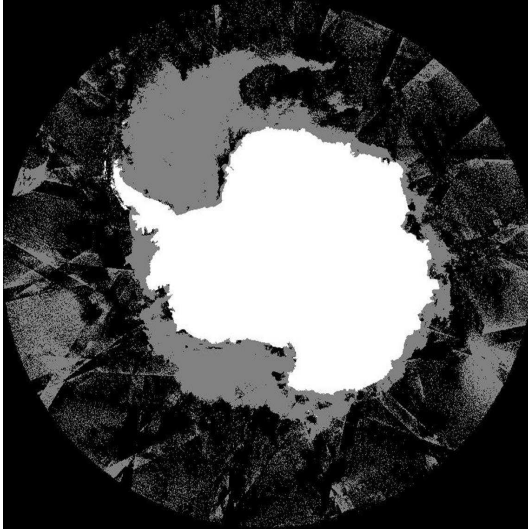
Figure C.1: .corr image from JD 001 2003. Black areas are areas classified as ocean, gray areas classified as sea-ice, and white areas are land.
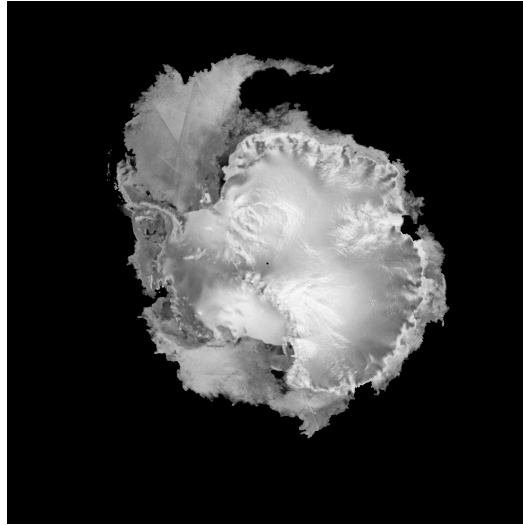
Figure C.2: Resulting ice-masked image using the long method from the .corr image on Figure C.1.

After the iterative ML step the .corr image is processed with the binary processing algorithm. This algorithm estimates the ice edge (where the ice stops and open ocean begins), filters spurious ice classifications, and assigns a value of 1 to all the pixels inside the ice edge and a 0 to all pixels outside the edge. This binary image is then multiplied by the original .sir image and a final ice-masked image is created. An example of an ice-masked image is shown in Fig. C.2.

In some cases it can difficult to discriminate between sea-ice and open ocean. This is because ice melt causes pooling on the ice, giving the ice ocean-like properties. Also, storms perturb the ocean, increase the backscatter, and cause the ocean to appear more ice-like. Additionally, the satellite may miss an area, or the ice-masking algorithm may be confused by moving ice. Also, both methods assume a Gaussian data distribution, and the data may not be so distributed [39].

To compare the RL and Long ice-mask algorithms several days of QuikSCAT data are chosen. For each of the test days, both binary processing methods are invoked with the Long .corr from the test day as an input. ML methods are also tested by using the .corr images from both methods as an input to the Long binary algorithm. Thus, for each test day four ice-masks are created. One from the Long binary method using the RL .corr image, from the RL binary method from the RL .corr image, and two from both Binary methods with the Long .corr image. The four images are then analyzed for accuracy.

C.2 Binary Processing Results

This section compares the Long and RL binary processing algorithms. To test the algorithms, ice-masked images are made from both binary methods, using the same Long .corr image for each of test days. Ice-masks using the RL .corr image are nearly identical and are omitted. Results are from Julian Days (JDs) 300, 2002, and 1, 97, 100, 121, 200, 271, and 300 of 2003. Most days of testing yield identical results and only days with significant differences are noted in this section.

The only test day with significant ice-mask differences is JD 100, 2003. Figure C.3 displays the ice-mask result from the RL binary processing in quadrant A of Antarctica while the corresponding image resulting from the Long processing is in Fig. C.4. It can be seen that the image from the RL binary processing detects a 28,000 km^2 piece of sea-ice that extends east from the Antarctic Peninsula into the Bellingshausen Sea. The ice-mask produced by the Long binary step does not detect ice in the same area.

To determine which ice-mask is more accurate both ice-masks in Figs. C.3 and C.4 are compared with the SIR image from JD 100, 2003 shown in Fig. C.5. This image does not exhibit the ice east of the Antarctic Peninsula show in Fig. C.3. Thus it can be determined that, in this case, the Long binary processing is more accurate than the RL binary processing.

For each of the test days, there is no case in which the RL binary processing step is more accurate than the Long method. In fact, the two methods are equivalent
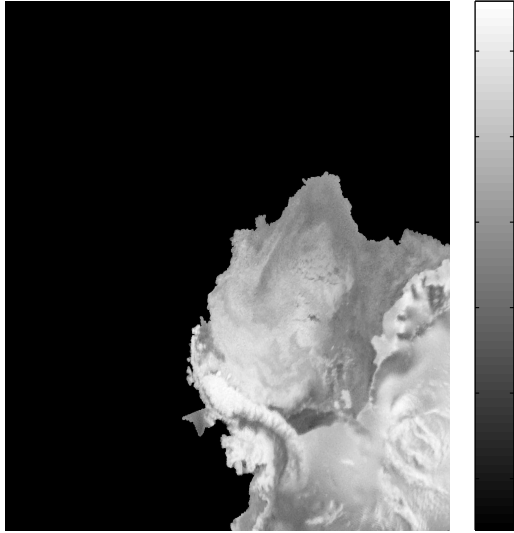
Figure C.3: JD 100, 2003 icemask using the RL method from quadrant A of Antarctica. This image shows sea-ice below the Antarctic Peninsula. This is probably incorrect based on Fig. C.5.
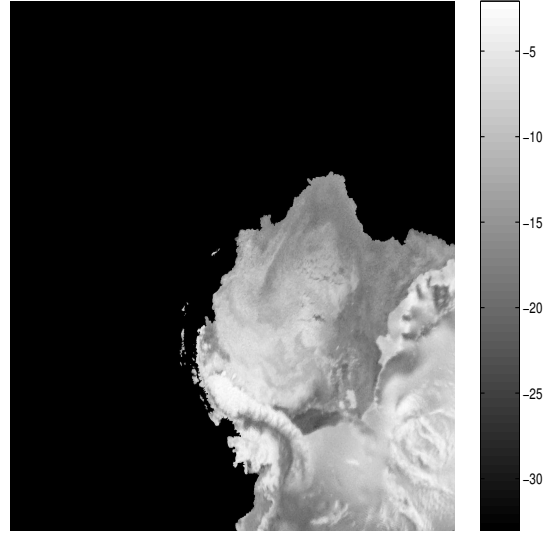

Figure C.4: JD 100, 2003 icemask using the Long method from quadrant A of Antarctica. This image exhibits open ocean in the area east of the Antarctic Peninsula where Figure C.3 shows ice. This is probably correct.

for all but one of the examined days. On the day in which a significant difference occurs, JD 100, 2003, the Long binary algorithm produces a more accurate ice-mask.

C.3 Iterative ML Classification Analysis

This section compares the performance of the Long and RL iterative ML processing algorithms. This appendix uses two methods of comparison. One method is to perform a human analysis on the .corr image created by the ML step and make accuracy observations. This is difficult because the quality of a .corr image is not obvious. For example, Figs. C.6 and C.7 show the Long and RL .corr images from JD 097, 2003, over quadrant A, Antarctica. Although differences can be seen between the two files, it is difficult to ascertain which file is better through direct examination. An alternate method of testing the iterative ML step is it to perform binary processing using the resulting .corr image and analyze the results. In this section we use the alternate method. For each of the chosen test days ice-masks created by both binary
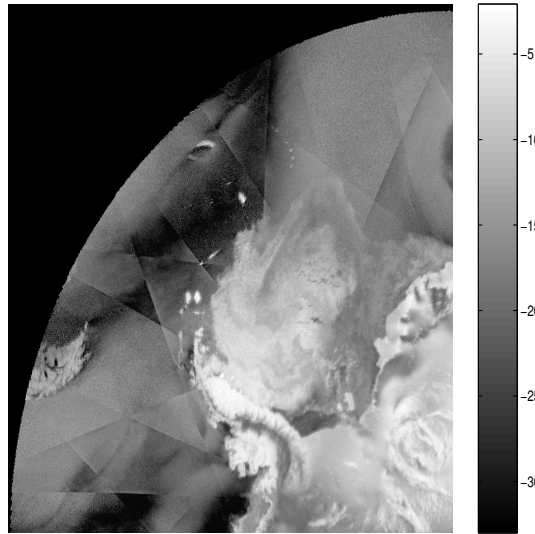
Figure C.5: V-pol .sir image from quadrant A of Antarctica, JD 100, 2003. This image does not exhibit the ice east of the Antarctic Peninsula in Fig. C.3.

methods in conjunction with the Long binary processing algorithm are compared for accuracy.

Figures C.8, C.9, C.10 show ice-masking results using the Long .corr, RL .corr, and the sir image from quadrant B, Antarctica from JD 097, 2003. Figure C.9 shows a large piece of ice on the bottom left of the ice pack that Fig. C.8 does not. This piece of ice does not appear in Fig. C.10, suggesting that the ice-mask created using the RL ML method is probably in error. The error has an area of about 40,000 km^2. Because it does not have the error, the Long iterative ML algorithm appears to be more accurate.

Figures C.11 and C.12 display ice-masks from JD 300, 2002. The largest differences occur on the middle left of the images. The ice-mask from the RL image exhibits a 136,000 km^2 piece of ice extending into the Amundsen Sea that the ice-mask from the ice-mask from the Long .corr file does not. Also, just northwest of the Antarctic Peninsula, the Long ice-mask indicates ice where the RL mask does not. The final difference can be seen on the very top of the images where the Long image exhibits a finger of ice of area 48,000 km^2 that the RL does not have. A review
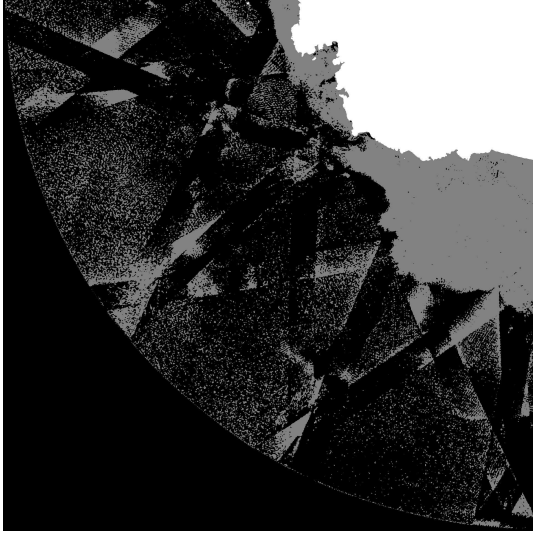
Figure C.6: JD 097, 2003 Long .corr image from quadrant B.
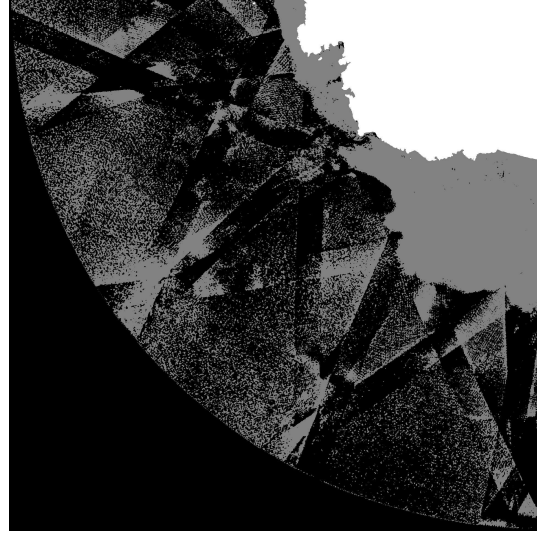
Figure C.7: JD 97, 2003 RL .corr image from quadrant B.

of the SIR image from the same day reveals that the ice in the Amundsen Sea, and the hole northwest of the Antarctic Penninsula are errors resulting from the RL ML algorithm, while the finger on the upper part of the image is an error by the Long ML algorithm. So, in this case both algorithms have errors not in the other. The error from the Long algorithm is smaller in area then that from the RL algorithm. However, in other cases, the RL algorithm may be better. Figures C.13, C.14 display ice-masks from JD 271, 2003 in quadrant D, Antarctica. Both ice-masks exhibit a large error off the western side of the ice-edge. The error in the RL ice-masks is 40,000 km^2 larger then the error in the Long icemask. Once again, while both ice-masks have errors, the RL ice-mask has the larger error.

Figure C.8: JD 097, 2003 quadrant B icemask, created from the Long .corr image.
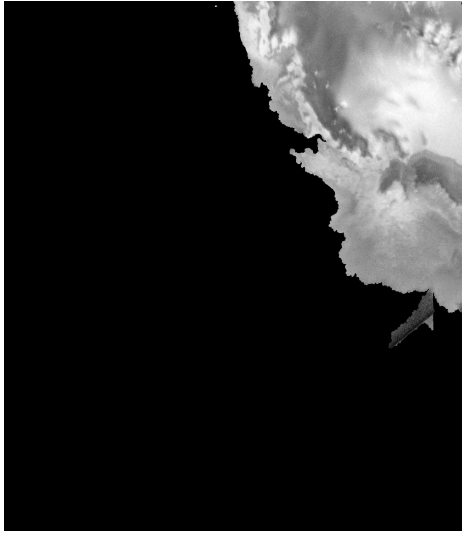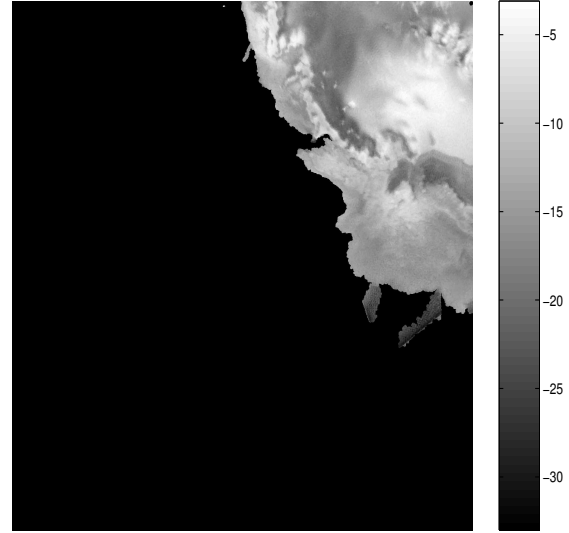

Figure C.9: JD 97, 2003 quadrant B icemask, created from the RL .corr image.

C.4 Conclusions

This appendix highlights days in which the Long and RL ice-mask differ significantly. Most of the differences occur between JD 300, 2002 to JD 100, 2003. This is because those days are days of greatest Austral melt. During melt, water pools on the surface of the ice and the backscatter decreases. This causes the ice to appear more ocean-like. This effect is augmented in storms when the ocean's backscatter increases and the the ocean to appears more like ice. In such instances, it can be especially difficult to determine the ice-edge.

Both the RL and Long binary processes produce nearly equivalent ice-masks. On all the examined days except JD 100, 2003, the results from the two processes exhibit no significant differences. The difference from JD 100, 2003 is relatively small, $28,000$ km^2, and is caused by an error from the RL binary processing.

Over the tested days, the iterative ML algorithms generally produce identical results. On the days in which differences are seen, the Long algorithm, with one exception, is more accurate. The RL ML step is seen to cause large errors, up to $136,000$ km^2, while the error caused by the Long ML step has an area of only 48,000
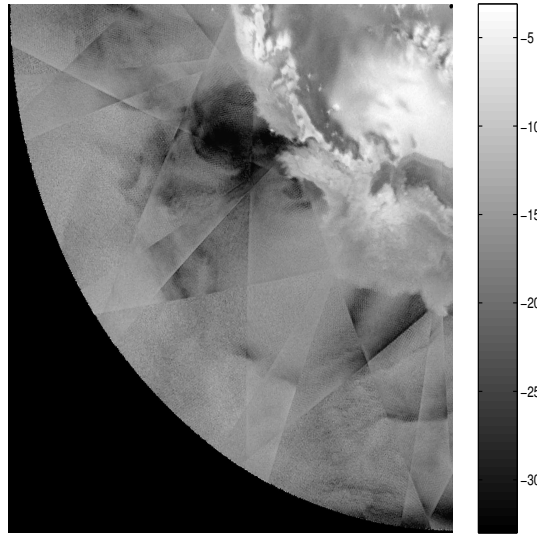
Figure C.10: V-pol SIR image from JD 97, 2003, quadrant B.

km^2. In general, the differences between ice-masks from the Long and RL iterative ML algorithms are caused by improvements in the Long step not seen in the RL algorithm.

To summarize, both the Long and RL ice-mask algorithms produce similar results. On days in which differences are seen, those differences are generally errors in the RL ice-mask that are not seen in the Long ice-mask. The Long algorithm appears to be a more accurate process that yields a more precise ice-edge.

Figure C.11: JD 300, 2002 icemask
using the Long .corr file

Figure C.12: JD 300, 2002 icemask
using the RL .corr file

Figure C.13: JD 271, 2003 ice-mask
from quadrant D using the Long .corr
file

Figure C.14: JD 271, 2003 ice-mask
from quadrant D using the RL .corr file

Bibliography

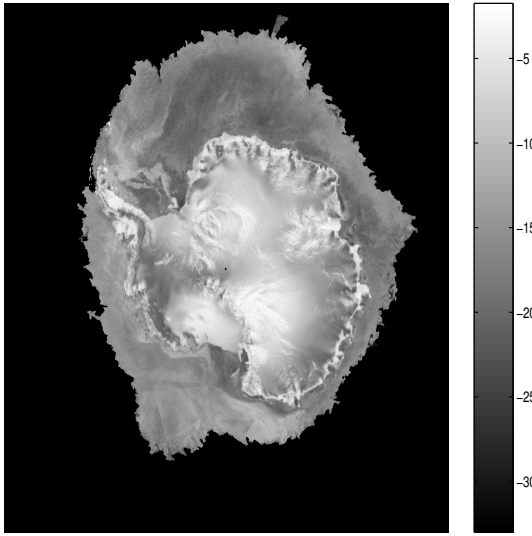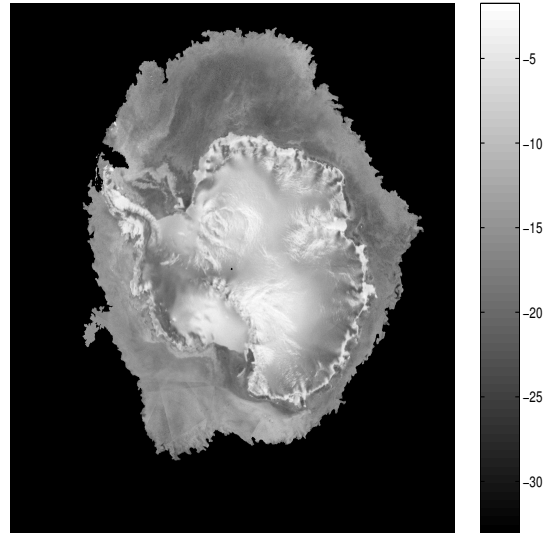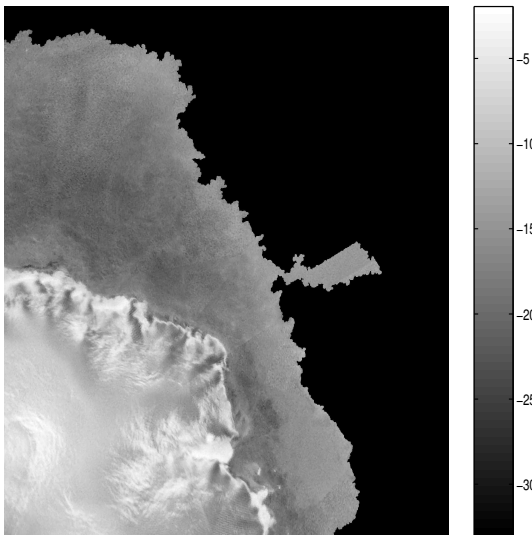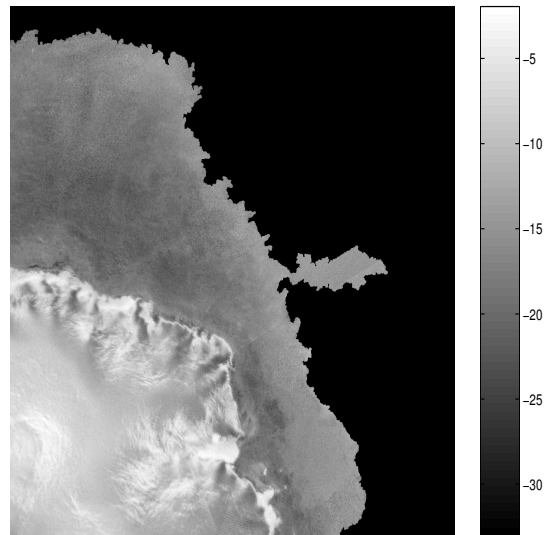[1] A. Bentamy, E. Autret, P Queffeulou, and Y. Quilfen, "Intercomparison of ERS-2 and QuikSCAT winds", in *IEEE International Geoscience and Remote Sensing Symposium*, 2000.

[2] D.W. Draper and D.G. Long, "An assessment of SeaWinds on QuikSCAT wind retrieval", *J. Geophys. Res.*, 2002, doi:10.1029/2002JC001330.

[3] L.F. Bliven and J.P. Giovanangeli, "Experimental study of microwave scattering from rain- and wind-roughened seas", *Int. J. Remote Sens.*, vol. 14, pp. 855–869, 1993.

[4] R.F. Contreras, W.J. Plant, W.C. Keller, K. Hayes, and J. Nystuen, "Effects of rain on Ku-band backscatter from the ocean", *J. Geophys. Res.*, vol. 108, no. C5, pp. (34)1–(34)15, 2003.

[5] D.E. Weissman, M.A. Bourassa, and J. Tongue, "Effects of rain rate and wind magnitude on SeaWinds scatterometer wind speed errors", *Atmos. Ocean. Tech.*, vol. 19, no. 5, pp. 738–746, May 2002.

[6] D.W. Draper and D.G. Long, "Evaluating the effect of rain on SeaWinds scatterometer measurements", *J. Geophys. Res.*, 2004, doi:10.1029/2002/JC001741.

[7] D.W. Draper and D.G. Long, "Assessing the quality of SeaWinds rain measurements", *IEEE Trans. Geosci. Remote Sensing*, vol. 42, no. 7, pp. 1424–1432, July 2004.

[8] D.W. Draper and D.G. Long, "Simultaneous wind and rain retrieval using SeaWinds data", *IEEE Trans. Geosci Remote Sensing*, vol. 42, pp. 1411–1423, July 2004.

[9] Q.P. Remund and D.G. Long, "Sea-ice extent mapping using Ku-band scatterometer data", *J. Geophys. Res.*, vol. 104, pp. 11515–11527, 1999.

[10] D.G. Long, "Personal communication", May 2004.

[11] R.K. Moore and A.D. Fung, "Radar determination of winds at sea", *Proc. IEEE*, vol. 67, pp. 1504–1521, 1979.

[12] F.J. Wentz and D.K. Smith, "A model function for the ocean-normalized radar cross section at 14 GHz derived from NSCAT observations", *J. Geophys. Res.*, vol. 104, no. C5, pp. 11 499–11 514, May 1999.

[13] F.J. Wentz, M.H. Freilich, and D.K. Smith, "NSCAT-2 geophysical model function", *Proc 1998 Fall AGU Meeting*, 1998.

[14] M.H. Freilich and R.S. Dunbar, "Derivation of satellite wind model functions using operational surface wind analyses- An altimeter example", *J. Geophys. Res.*, vol. 98, no. C8, pp. 14633–14649, Aug 1993.

[15] C. Chi and F.K. Li, "Comparitive study of several wind estimation algorithms for spaceborne scatterometers", *IEEE Trans. Geosci. Remote Sensing*, vol. 26, pp. 115–121, March 1988.

[16] D.W. Spencer, C. Wu, and D.G. Long, "Tradeoffs in the design of a spacebourne scanning pencil beam scatterometer: Application to SeaWinds", *IEEE Trans. Geosci. Remote Sensing*, vol. 35, pp. 116–126, Jan. 1997.

[17] T.E. Oliphant and D.G. Long, "Accuracy of scatterometer derived winds using the Cramer-Rao bound", *IEEE Trans. Geosci. Remote Sensing*, vol. 37, pp. 2642–2652, Nov. 1999.

[18] Jet Propulsion Lab, *QuikSCAT Science data product user's manual*, California Inst. Technol., Pasadena, CA, 2003, Rep. D-18053.

[19] B.W. Stiles, B.D. Pollard, and R.S. Dunbar, "Direction interval retrival with thresholded nudging: A method for improving the accuracy of QuikSCAT winds", *IEEE Trans. Geosci. Remote Sensing*, vol. 40, pp. 79–89, Jan. 2002.

[20] S.J. Shaffer, R.S. Dunbar, S.V. Hsiao, and D.G. Long, "A median-filter-based ambiguity removal algorithm for NSCAT", *IEEE Trans. Geosci. Remote Sensing*, vol. 40, pp. 1973–1983, Sept 2002.

[21] B.W. Stiles and S. Yueh, "Impact of rain of spaceborne Ku-band wind scatterometer data", *IEEE Trans. Geosci. Remote Sensing*, vol. 40, pp. 1973–1983, 2002.

[22] M.W. Spencer and M. Shimada, "Effect of rain on Ku-band scatterometer wind measurements", in *Proc. IGARSS*, 1991, vol. 3, pp. 1285–1288.

[23] D.W. Draper, *Wind Scatterometry with Improved Ambiguity Selection and Rain Modeling*, PhD thesis, Brigham Young University, 2003.

[24] Federal Coordinator for Meteorological Services, Part B Dopler Radar Theory Supporting Research, and Meteorology, *Doppler Radar Meteorological Observations*, National Oceanic and Atmospheric Administration, 1991.

[25] J.S. Marshall and W.M. Palmer, "The distribution of raindrops with size", *J. Appl. Meteorology*, vol. 5, pp. 165–166, 1948.

[26] D.P. Jorgensen and P.T. Willis, "A Z-R relationship for mature hurricanes", *J. Appl. Meteorology*, vol. 21, pp. 356–366, 1982.

[27] F.T. Ulaby, R.K. Moore, and A.K. Fung, *Microwave Remote Sensing Active and Passive*, Artech House, 1981.

[28] J.K. Joss, K. Schram, J.D. Thams, and A. Waldvolgel, "On the quantitive determination of precipitation by radar", *Wissenschaftlich Mitteliungen*, , no. 63, pp. 38, 1970.

[29] R.H. Douglas, "Size distribution of Alberta hail samples", Tech. Rep., Montreal: Stormy Weather Group, McGill University, 1963.

[30] J.N. Huddleston and B.W. Stiles, "A multidimensional histogram rain-flagging technique for SeaWinds on QuikSCAT", in *Geoscience and Remote Sensing Symposium*, 2000, vol. 3, pp. 1238–1240.

[31] F.J. Wentz C.A. Mears, D. Smith, "Detecting rain with QuikSCAT", *Geoscience and Remote Sensing Symposium*, vol. 3, pp. 1235–1237, July 2000.

[32] B.W. Stiles, *Special wind vector data product: Direction Interval Retrieval with Threshold Nudging (DIRTH) Product Description*, Jet Propulsion Laboratory, Pasadena, CA, 1.1 edition, 1999.

[33] J.B. Luke, "High resolution wind retrieval for SeaWinds on QuikSCAT", Master's thesis, Brigham Young University, 2003.

[34] P. Gloersen, W. J. Campbell, D. J. Cavalieri, et al., *Arctic and Antarctic Sea Ice, 1978-1987: Satellite Passive-Microwave Obersvations and Analysis*, National Aeronautics and Space Administration, 1992.

[35] D.S. Early, *A Study of the Scatterometer Image Reconstruction Algorithm and its Applications to Polar Ice Studies*, PhD thesis, Brigham Young University, 1998.

[36] D.G. Long and D. Daum, "Spatial resolution enhancement of SSM/I data", *IEEE Trans. Geosci. Remote Sens.*, vol. 36, pp. 407–417, Mar. 1997.

[37] Q.P. Remund and D.G. Long, "Sea ice mapping algorithm for QuikSCAT and Seawinds", in *Proceedings of the International Geoscience and Remote Sensing Symposium*, 1998, vol. III, pp. 1686–1688.

[38] Q.P. Remund, *Multisensor Microwave Remote Sensing in the Cryosphere*, PhD thesis, Brigham Young University, 2000.

[39] H.S. Anderson, "Polar sea ice mapping for Seawinds", Master's thesis, Brigham Young University, 2003.

[40] C.L. Parkinson, "Length of the sea ice season in the southern ocean", in *Antarctic Sea Ice. Physical Processes, Interactions and Variability*, M.O. Jeffries, Ed., 1998.

[41] D. Cavalieri, P. Gloerson, and J. Zwally, "DMSP SSM/I daily polar gridded sea ice concentrations", 1990, updated 2004 July 1999 to December 2003. Edited by J. Maslanik and J. Stroeve. Boulder, CO: National Snow and Ice Data Center. Digital media.

[42] D.S. Early and D.G. Long, "Image reconstruction and enhanced resolution imaging from irregular samples", *IEEE Trans. Geosci. Remote Sens.*, vol. 39, no. 2, pp. 291–302, Feb. 2001.

[43] D.G. Long, P.J. Hardin, and P.T. Whiting, "Resolution enhancement of spacebourne scatterometer data", *IEEE Trans. Geosci. Remote Sens.*, vol. 31, pp. 700–715, May 1993.

[44] Q.P. Remund and D.G. Long, "Iterative mapping of polar sea ice using Ku-band SeaWinds scatterometer data", Unpublished Manuscript, September 2004.

[45] J. Serra, *Images Analysis and Mathematical Morphology*, Academic Press, 1982.

[46] A.K. Jain, *Fundamentals of Digital Image Processing*, Prentice Hall, 1989.

[47] J. Haarpaintner, R.T. Tonboe, D.G. Long, and M.L. Van Woert, "Automatic detection and validity of the sea-ice edge: An application of enhanced-resolution QuikSCAT/Seawinds data", *IEEE Trans. Geosci. Remote Sens.*, vol. 42, pp. 1433–1443, July 2004.